Int J Coal Sci Technol (2015) 2(2):97–161
DOI 10.1007/s40789-015-0071-4

# Key technologies and equipment for a fully mechanized top-coal caving operation with a large mining height at ultra-thick coal seams

**Jinhua Wang[1] · Bin Yu[2] · Hongpu Kang[1] · Guofa Wang[1] · Debing Mao[1] · Yuntao Liang[3] · Pengfei Jiang[1]**

Received: 20 February 2015 / Revised: 15 March 2015 / Accepted: 18 March 2015 / Published online: 21 July 2015


**Abstract** Thick and ultra-thick coal seams are main coal seams for high production rate and high efficiency in Chinese coal mines, which accounts for 44 % of the total minable coal reserve. A fully mechanized top-coal caving mining method is a main underground coal extraction method for ultra-thick coal seams. The coal extraction technologies for coal seams less than 14 m thick were extensively used in China. However, for coal seams with thickness greater than 14 m, there have been no reported cases in the world for underground mechanical extraction with safe performance, high efficiency and high coal recovery ratio. To deal with this case, China Coal Technology & Engineering Group, Datong Coal Mine Group, and other 15 organizations in China launched a fundamental and big project to develop coal mining technologies and equipment for coal seams with thicknesses greater than 14 m. After the completion of the project, a coal extraction method was developed for top-coal caving with a large mining height, as well as a ground control theory for ultra-thick coal seams. In addition, the mining technology for top-coal caving with a large mining height, the ground support technology for roadway in coal seams with a large cross-section, and the prevention and control technology for gas and fire hazards were developed and applied. Furthermore, a hydraulic support with a mining height of 5.2 m, a shearer with high reliability, and auxiliary equipment were developed and manufactured. Practical implication on the technologies and equipment developed was successfully completed at the No. 8105 coal face in the Tashan coal mine, Datong, China. The major achievements of the project are summarized as follows: 1. A top-coal caving method for ultra-thick coal seams is proposed with a cutting height of 5 m and a top-coal caving height of 15 m. A structural mechanical model of overlying strata called cantilever beam-articulated rock beam is established. Based on the model, the load resistance of the hydraulic support with a large mining height for top-coal caving method is determined. With the analysis, the movement characteristics of the top coal and above strata are evaluated during top-coal caving operation at the coal face with a large mining height. Furthermore, there is successful development of comprehensive technologies for preventing and controlling spalling of the coal wall, and the top-coal caving technology with high efficiency and high recovery at the top-coal caving face with a large mining height. This means that the technologies developed have overcome the difficulties in strata control, top-coal caving with high efficiency and high coal recovery, and enabled to achieve a production rate of more than 10 Mtpa at a single top-coal caving face with a large mining height in ultra-thick coal seams; 2. A hydraulic support with 5.2 m supporting height and

✉ Hongpu Kang
kanghp@163.com

[1] China Coal Technology & Engineering Group, Beijing 100013, China

[2] Datong Coal Mine Group Co., Ltd., Datong 037003, China

[3] CCTEG Shenyang Research Institute, Shenyang 110016, China

anti-rockburst capacity, a shearer with high reliability, a scraper conveyor with a large power at the back of face, and a large load and long distance headgate belt conveyor have been successfully developed for a top-coal caving face with large mining height. The study has developed the key technologies for improving the reliability of equipment at the coal face and has overcome the challenges in equipping the top-coal caving face with a large mining height in ultra-thick coal seams; 3. The deformation characteristics of a large cross-section roadway in ultra-thick coal seams are discovered. Based on the findings above, a series of bolt materials with a high yielding strength of 500–830 MPa and a high extension ratio, and cable bolt material with a 1 × 19 structure, large tonnage and high extension ratio are developed. In addition, in order to achieve a safe roadway and a fast face advance, installation equipment for high pre-tension bolt is developed to solve the problems with the support of roadway in coal seams for top-coal caving operation with a large mining height; 4. The characteristics of gas distribution and uneven emission at top-coal caving face with large mining height in ultra-thick coal seams are evaluated. With the application of the technologies of gas drainage in the roof, the difficulties in gas control for high intensive top-coal caving mining operations, known as "low gas content, high gas emission", are solved. In addition, large flow-rate underground mobile equipment for making nitrogen are developed to solve the problems with fire prevention and safe mining at a top-coal caving face with large mining height and production rate of more than 10 Mtpa. A case study to apply the developed technologies has been conducted at the No. 8105 face, the Tashan coal mine in Datong, China. The case study demonstrates that the three units of equipment, i.e., the support, shearer and scraper conveyor, are rationally equipped. Average equipment usage at the coal face is 92.1 %. The coal recovery ratio at the coal face is up to 88.9 %. In 2011, the coal production at the No. 8105 face reached 10.849 Mtpa, exceeding the target of 10 Mtpa for a top-coal caving operation with large mining height performed by Chinese-made mining equipment. The technologies and equipment developed provide a way for extracting ultra-thick coal seams. Currently, the technologies and equipment are used in 13 mining areas in China including Datong, Pingshuo, Shendong and Xinjiang. With the exploitation of coal resources in Western China, there is great potential for the application of the technologies and equipment developed.

**Keywords** Ultra-thick coal seams · Top-coal caving mining · Large mining height · Mining method · Mining equipment · Roadway support · Safety guarantee

## 1 Introduction

In China, there is approximately 1341 Bt of proven coal resource, including 279.58 Bt of basic coal resource for coal mine construction. Among them, coal resource in thick coal seams accounts for 44 % of the total available. The annual underground coal production from thick coal seams exceeds 45 % of total coal production. Since the Eighties in the last century, there have been many research projects focusing on mechanical coal extraction from thick coal seams. The mining technologies and systems for thick and ultra-thick coal seams have been gradually developed in China. Until recently, there have been three major mechanical mining methods for thick coal seams, i.e., a fully mechanized longwall top-coal caving mining method (thereafter LTCC mining method), a fully mechanized sub-level coal mining method, and a fully mechanized mining with a large mining height method. There are some limitations with the fully mechanized sub-level coal mining method, including the thickness variation of coal seams, spontaneous combustion, unit mining cost and efficiency. Due to the low production efficiency (Qian and Shi 2003; Wang 2005; 2006a; Mao and Yao 2010; Wang 2010a), the fully mechanized sub-level coal mining method is currently replaced by the other two mining methods. Compared with the fully mechanized sub-level coal mining method, the fully mechanized coal mining with a large mining height method can reduce the amount of roadway development, mitigate the tension between mining and development, and simplify the mining process. With the progress of mining technologies and equipment in China, the fully mechanized coal mining with a large mining height method has seen widely used (Yan and Yin 2008; Yan 2009; Yan et al. 2011), and has achieved significant mining profit and coal recovery. The method is only applicable to the coal seams of low dip, relative stable, and good roof conditions, and is also limited by the shearer's cutting height and coal wall spalling. For this reason, the mining height for one mining pass is 7.0 m (Wang et al. 2012), and cannot meet the requirement for safe and efficient mining in ultra-thick coal seams above 7 m. In terms of ultra-thick coal seams above 7 m, the top-coal caving mining method is the first choice. For coal seams with thicknesses ranging from 7 to 14 m, the top-coal caving mining method can be applied as the technologies and the equipment are well established and manufactured. In order to achieve safe and efficient coal extraction in ultra-thick coal seams with thicknesses ranging from 14 to 20 m, the authors propose a fully mechanized large mining height longwall top-coal caving mining method (thereafter LLTCC mining method), developed a full range of technologies and equipment for a LLTCC mining operation. The technologies and equipment developed have been successfully applied in the Tashan coal mine

in Datong, China, and has achieved a production of 10 Mtpa at a LLTCC mining operation in the ultra-thick coal seam. In the early twentieth century, the top-coal caving mining method was applied at steep seams in France, Spain and former Yugoslavia. Due to the low mechanical levels in mining, the method was actually an alternative of the high caving mining method, which was only used as a special mining method under complex geological conditions. At the end of forties and early fifties of the twentieth century, the top-coal caving mining method was used to extract the thick coal seams in the former Soviet Union, France and former Yugoslavia. With the progress of hydraulic support technology, the fully mechanized top-coal caving technology was improved and successfully applied in some countries.

In the late eighties of the last century, the top-coal caving technology was not widely applied and its potential was not fully achieved due to the competition from other energy industries, the changes of social and political systems, and no solutions for the difficulties of its application in difficult geological conditions. Up to 1992, fully mechanized top-coal caving faces had been stopped in all countries, with the last site in Russia. By that time, China was the only country using the LTCC mining method to extract coal from thick coal seams (Wang 2009). Currently, China is a world leader in developing and conducting the LTCC mining technology, which results in several large, safe, high production rate and high efficiency mining areas including Luan, Yanzhou, Yangquan and Suozhou (Fan et al. 2003; Wang 2011). In recent years, with the development of the LTCC mining technology in China, the technology and equipment is starting to be introduced in some other countries, such as Australia, and is successfully used in underground coal mines.

Although China was late to develop and apply top-coal caving mining technology, its development and applications are progressing very fast, showing significant economic potential and attracting attentions from other countries. In China, the top-coal caving mining method means the fully mechanized longwall top-coal caving mining method. A longwall panel is laid out at the bottom of the thick coal seam and extracted using a fully mechanized longwall mining method. At the same time, the remaining coal above the longwall face are fractured by ground stress and strain (manually fractured in some special cases), and caved through the sliding window at the support canopies into an additional scraper conveyor, and then transported out of the working face. There are approximately four stages for the development of LTCC technology in China.

### 1.1 Stage 1: Exploration stage (1982–1990)

Since 1982, the LTCC technology has been introduced and investigated in China. In 1984, the first industrial trial of the technology at a gentle inclined seam was conducted at Northern Area 3 in Puhe mine, Shenyang Province, China (Yan and Fu 2003). Due to the problems with support design and equipment, and lack of experience in production management, the trial was not successful. However, the subsequent trials at steep inclined coal seams in the No. 2 mine of Yaojie, Meihekou mine of Liaoyuan, and Liudaowan mine in Urumqi, China, were all successful. Up until 1990, although the trials on the technology at gentle inclined coal seams continued in Northeastern China and Pingdingshan, there were no breakthroughs. In the second half of 1990, the LTCC face 8603 at the No. 1 coal mine in Yangquan produced 140,000 t/m, doubling the production from a sub-level coal face and exceeded 80 % of coal recovery from the face. The dip of the LTCC face was 3°–7°, the thickness was 6 m and the face width was 120 m. The trial at Yangquan found a way to achieve high production, high efficiency at a LTCC face, demonstrated the potential with LTCC technology, and laid a solid foundation for the development of LTCC technology. The feasibility of high production capacity and high efficiency of the technology has been proven at this stage.

### 1.2 Stage 2: Gradual maturation (1990–1995)

The key achievement at this stage was that the LTCC face at Xinglongzhuang mine in Yanzhou, China, reached the high production of 3 Mtpa. In addition, there was a breakthrough for LTCC technology at “three soft” coal seams, “large dip” coal seams (approximately 30°), and “high gassy” coal seams, which will enable a wide application of the technology in China. At this stage, the LTCC technology developed quickly and made some coal mining companies in China realize that the LTCC technology was a technological step-change for the coal mining industry. In addition, the research and studies were very active in the areas of ground control, support-strata relationship, cavability of top coal, and methods of top-coal caving, which provided various theories and practices.

### 1.3 Stage 3: Technical maturation and promotion (1995–2005)

Due to the huge technical advantages demonstrated, LTCC technology has attracted great attention from mining companies in China. Also with the removal of some technical difficulties in using LTCC technology, LTCC technology was widely and quickly applied in the coal mining industry in China. In 1995, LTCC technology was selected as one of five key technologies for further research and promotion during the period of the ninth five-year national economic plan by the Ministry of China Coal Industry. Several major technical issues associated with the

LTCC mining method were named as key topics for research. Furthermore, in 1997, China National Nature Science Foundation launched a research project of "Basic study of whole seam coal extraction in thick coal seams". Various achievements were obtained at this stage. In some coal mines that meet appropriate geological conditions i.e., simple geological conditions, large coal reserves, fewer natural hazards, 6–9 m coal seams, and medium hard coals, the annual coal production and profit at LTCC faces increased substantially. For instance, in 1997, the coal production rate at the LTCC face in Dongtan mine in Yanzhou, China, achieved 4.1 Mtpa, and 208 t/manpower. In 1998, at the same face, the coal production rate reached 5.4 Mtpa, and the manpower efficiency was at 235 t/manpower, which was regarded as a world level in that time. In addition, at this stage, the LTCC technology was developed to extract some difficult coal seams, such as "three soft", "two hard", "large dip", "high gassy", "spontaneous combustion-prone", and "ultra-thin seams", etc. The various technologies were obtained from the above development.

During the period of the tenth five-year national economic plan, a project called "the research and experiment on LTCC technology and equipment with a production capacity of 6 Mtpa" was completed in Yanzhou, China. The study enabled a higher than 6 Mtpa production rate of the LTCC face for six consequent years, which showed that LTCC technology in China had reached a new high level.

### 1.4 Stage 4: Improvement (2005 to present)

In 2005, during the study of safe and high efficiency mining technologies for high gassy ultra-thick coal seams, the causes of problems that stagnated the production of high gassy LTCC faces were analyzed. In addition, the feasibility of further increasing the coal cutting height was investigated for coal extraction using LTCC technology at ultra-thick coal faces. In 2006, Li et al. (2006) presented some characteristics and potential of designing top-coal caving hydraulic support with large mining heights. In terms of equipment capacities, Lu et al. (2006) conducted a study on a complete set of mining equipment with a cutting height of 3.5 m. Currently, in order to overcome the difficulties in mining high gassy and ultra-thick coal seams, some mining companies in China, such as Tunliu mine and Wangzhuang mine of Luan Group, and Tashan mine of Datong Group, conducted various LTCC mining experiments with large mining heights and studies on the ground control at LTCC faces. Because LTCC mining technology with large mining height is a new coal mining method, however, there is still a lack of related theories and studies; for instance, the applicable conditions for a large mining height LTCC mining operation, the movement of the top coal and the roof strata, stress distribution around the face, and a complete set of equipment for a large mining height LTCC face.

In terms of LTCC mining operations, the characteristics of ground pressure, the movement of the top coal and roof strata, and the relationship between the support and surrounding rock are the main topics. They are also the main criteria for the selection of face equipment, mining parameters and support parameters.

The studies on ground pressure and the movement of the top coal and roof strata are limited in countries other than China. Limited literatures exist that describe top coal movement and top coal cavability (Hu 1995), while there is less description on roof structure, face pressure, and roof control, etc. Since the application of LTCC technology, there have been many studies on the movement characteristics of overlying strata, which has resulted in a large amount of achievements.

Kang Lijun (Kang 1990; 1995; 1996; 1998; 1999; Kang and Qi 1998; Kang et al. 1998; 1999) divided the roof movement into two stages, the non-complete extraction stage and the complete extraction stage. At the non-complete extraction stage, the periodic pressure from the main roof is mainly caused by the combination impact or individual impact from the broken cantilever beam roof in the irregular caving zone, and the broken or overturned overlying beam roof fixed at the two ends. But at the complete extraction stage, the periodical pressure from the main roof is mainly caused by the periodical broken, overturn and unstable arch beam roof in the regular caving zone. The strength of periodic pressure at the non-complete extraction stage is higher than that at the complete extraction stage. A case study on the roof movement of a LTCC face at the No. 4 mine in Yangquan, China, further described the roof movement at the two stages (Kang et al. 1997). Based on the movement characteristics of overlying strata at the LTCC face, Yan (1996) introduced a mechanical theory of limited deformation and proposed a balance structure of macro continuous "compressed arch beam" of overlying strata at the upper location.

Deng Guangzhe et al. from the Xi'an Mining Institute (Deng 1994) investigated the characteristics of "arch structure" of overlying strata movement and ground control law based on the observation and measurement at LTCC face and the analysis of 3D analogue modelling. Using mechanical analysis of the shell structure, the arch structure of the overlying strata at LTCC face was preliminarily analyzed. The analysis concluded that the formation of the arch structure at overlying strata relies on some external conditions. When there are no stable skewbacks, the arch structure becomes unstable. The caving of the arch structure of strata shows an abruptness. Zhang (1999) believe that after the immediate roof caved, an

unstable "arch similarly" structure may be formed within 1.0–1.2 times of mining height above the coal face, and its stability is random. On the other hand, after the caving of the immediate roof above the unstable range, a stable "arch similarly" structure may be formed due to limited space. This type of "arch similarly" structure may be formed and caved with the advance of the coal face, resulting in periodical ground pressure.

Jiang Fuxing et al. proposed a concept of spatial structure of the overlying strata. Based on the different mining boundaries at different mining areas, the main roof and overlying strata may form four types of 3D structures after caving, including type "θ", "O", "S" and "C". The spatial structure type of overlying strata in mining regions or mines is initially determined by design, and then varies with the mining operation. It is determined by roof property, buried depth, coal pillars between the working face and the mining area, and fault protection pillars. In addition, it varies at different mining stages (Ma 2005; Jiang 1995; 2006; Wang 2006b; Hou et al. 2009; Liu 2010).

In terms of the movement characteristics of overlying thick hard strata, Shi Hong (Shi 2005; Shi and Jiang 2004; 2005; Shi et al. 2005) regard the hard strata as a simple "beam fixed at two ends" structural model and analyzed the broken characteristics of thick hard strata before the initial fracture of the main roof. Using the stress distribution in the strata, Shi Hong, et al., proposed a mechanical criterion for three broken modes of thick hard rock, and predicted the initial fracture and the ground pressure interval of the main roof.

Based on the "elastic plate and articulated plate" mechanical model, Jia Xirong of Taiyuan University of Technology et al. (Jia et al. 1998) extended the ground pressure calculation method in medium thick coal seams into the calculation of ground pressure at LTCC face roof. According to the structural properties of roof strata and mining conditions, the strata with no self-support capability after fracture (no self-support strata) are defined as immediate roof. The strata with support structure, but without sufficient self-support capability after fracture (transition strata) are defined as main roof. The strata with self-support capability after fracture (complete support strata) are defined as roof overlying strata. In addition, they presented the basic assessment criteria for complete support strata, transition strata and no self-support strata.

Xie Guangxiang (Xie 2005; 2006; Xie and Luo 2005; Xie et al. 2006a, b; 2007a, b; 2009) believe that there is a "stress shell" composed of high stress beams in the surrounding rock space of mines. The maximum principal stress in the "stress shell" is greater than the principal stress in the strata inside and outside the "stress shell". The stress shell bears and transfers the load and pressure from the overlying rock, and is a major support body while the main roof bears only partial load. Based on the findings on the "stress shell" and its mechanical properties, the 3D mechanical properties of the surrounding rock at LTCC faces were found, including the effect of mining height, the mechanism of pillar width and the response of advance rate. Furthermore, the mechanical properties of ground pressure abate and the mechanisms of dynamic hazard mitigation were obtained.

Some researchers have completed various studies on the theory of ground control and the law of roof movement at LTCC face (Buddery and Oldroyd 1992; Zhang 1995; Wu 1998; Wang et al. 2001; Yasitli and Unver 2005; Ren 2005; Liu et al. 2006; Nan et al. 2008; Liu and Huang 2009; Xie and Zhao 2009a, b; Altounyan and Taljaard 2001; Alehossein and Poulsen 2010; Chen et al. 2010; Miao and Lai 2011; Yu et al. 2011; Zhang et al. 2011), including seismic monitoring (Liu 2008a, b; Kong et al. 2009; 2010a, b, c), analogous material (Kang et al. 2007a, b), numerical modelling (Wang et al. 2007; Zhu and Yan 2011), theoretical analysis (Meng 2007; Yang 2007; Fu 2008; Wu 2008; Zhang and Liu 2008; Zhou and Su 2008; Li and Xu 2009; Shi et al. 2009; Xing et al. 2009; Liu 2010; Meng et al. 2010; Wang 2010b) and site observations (Cheng 2008; Duan et al. 2008; Liu 2008a, b; Su 2008; Song et al. 2010).

The research results above are all based on the characteristics of ground pressure, and the models of "beam", "arch"and "shell". In addition, theoretical analysis and analogous (numerical) modelling were used to establish the model of overlying strata structure. Subsequently the models were validated on site. As a stable structure is formed in the strata at higher locations, its deformation and fracture will not affect or have little effect on the ground pressure at working face. Although there are some differences in studying methods and aspects, the ultimate purposes of the models derived are to explain the ground pressure during the LTCC operation and maintain a high efficient safe production. In recent years, however, the strong ground pressure at a large mining height LTCC face in ultra-thick coal seam cannot be explained by previous experiences and knowledge accumulated at a normal LTCC face. Therefore, based on the LTCC operation in ultra-thick coal seam of more than 14 m, this paper proposes a "cantilever beam-articulated rock beam" structural model. Based on the model proposed, the resistance force of support was calculated and the top coal and roof movement were monitored and analyzed.

In the study on the relationship between support and surrounding rock, to overcome the difference between the actual measurement and the traditional theory, Qian Minggao (Liu 1996; Qian et al. 1996a, b; Liu et al. 2002) regarded the key blocks of the Voussoir beam as the top boundary condition of the immediate roof, and believed

that the support resistance force is mainly from "the pressure of loose blocks" and "the deformation pressure of overturned blocks" caused by the "S–R" movement of the "Voussoir beam". The deformation of immediate roof results in the overturned deformation load of the immediate roof inserted by the Voussoir beam absorbed by the fractured immediate roof (including top coal) and the non-existence of double curve relationship in the "$P$–$\triangle L$" relationship. Based on the mechanical properties and effect of various components in the support and surrounding rock system, the mechanical model of support and surrounding rock was established and provided a basis for further investigation on the relationship between the support and surrounding rock.

With the development of LTCC technology, the comprehensive mechanical model for LTCC mining face has been greatly improved. Liu Changyou, et al. used site observation, finite element numerical calculation, and the analogous material modelling method to investigate the comprehensive mechanical properties of the immediate roof and their effect on the relationship between support and surrounding rock. By considering the immediate roof as a variable body, the characteristics of deformation and fracture of the immediate roof and the structural mechanical and stiffness properties of the immediate roof were studied. They proposed that the load of the immediate roof is regionalized, and provided a calculation method for the stiffness of the immediate roof. In addition, based on the stiffness characteristics of the immediate roof with a rectangle shape face, the immediate roof is divided into three categories as stiffness similar, zero stiffness and medium stiffness. When the immediate roof stiffness is zero, the support is in the status of a "given load" or a "limited load". When the immediate roof is in a stiffness similar status, the support is in a "given deformation" status. When the immediate roof is in a medium stiffness status, the "$P$–$\triangle L$" curve shows a typical double curve relationship. When the immediate roof is in a zero stiffness status, the rational resistance force of support is mainly determined by its effect on the stability of the face ends.

The thickness variation of the immediate roof (including top coal) also affects the load bearing capacity of the immediate roof. Cao Changsheng et al. (Liu et al. 1997; 2002; Cao and Liu 1997; Cao et al. 1998; 1999; Cao et al. 1999) presented a concept on the critical thickness of the immediate roof and believed that the "$P$–$\triangle L$" double curve flattens when the immediate roof thickness exceeds a critical thickness. In other words, the variations of support resistance and main roof overturn angles have little effect on the roof subsidence.

Shi Yuanwei et al. (Kang et al. 1991; Shi and Chen 1993; Shi et al. 1993) presented and analyzed the critical thickness of the immediate roof and its effecting factors. They state that when critical thickness is greater than actual thickness, or when the immediate roof in front of the face enters a plastic zone, the immediate roof would lose its load bearing capacity after it enters the roof control zone. Therefore, the mechanical relationship of support and surrounding rock will show a variation. In contrast, the immediate roof will maintain a certain deformation capacity.

Fang (2002) simulated the effect on the roof stability at face ends by support type using discrete element software and believes that under soft coals, the critical issue is to control the distance from the support tip to the coal wall, which must be controlled within the distance limit. Under the conditions of medium hard coals, the constraint distance from the support tip to coal wall is relatively large and thus there will be a rational arrangement for the tip to wall distance and support resistance force. For hard coals, the study focus should be on improving the top coal caving ability. In the study on the mechanical relationship of support and surrounding rock in a soft coal extraction, Huang (2002) found that the increase of support resistance can reduce the tensile stress range in the top coal between support tip and coal wall, increase the self-support capacity from the top coal between support tip and coal wall, and suppress the movement and fracture of top coals. Nevertheless, the increase of support resistance has a limited effect on the improvement of subsidence of unsupported zone between the support tip and coal wall.

Jin et al. (2002) state that under the condition of hard roof and hard coal, the LTCC face shows the characteristics of hard roof, and demonstrates the characteristics of top coal cushion effect at LTCC face. The rational support resistance force should be based on the cantilever beam model with a modification by the coefficient of cushion effect.

Wu Jian et al. (Wu and Yan 1995; Wu and Fu 1998; Wu and Zhang 2001) suggest that the traditional ground control theory could not explain the interaction relationship between the support and surrounding rock. The key support parameters in the support and surrounding rock relationship includes the vertical support force, the horizontal support force, the distance between the supporting point of resultant force and the coal wall, and the distance between the support tip and coal wall. There are obvious effects from these parameters, sometimes obvious only when they interact.

Yang et al. (2009) state that the key to the interaction system of the support and surrounding rock is the interaction between the support and top coal. Under hard coal conditions, the overturn of the immediate roof is affected by the support and top coal system, and the turning angle of the lower strata is less than the turning angle of the main roof. Under the medium hard coals and soft coals, the

immediate roof can equally transfer the overturn deformation of the main roof to top coals and the support system. With the consideration of the immediate roof as the top boundary of support-top coal systems, the mechanical model for two-leg shield support and surrounding rock can be established.

The studies on the relationship between roof support and surrounding rock provide theories for the design and selection of LTCC roof support, the improvement of support-surrounding rock status and effective roof control (including top coals). In this paper, based on the relationship between roof support and surrounding rock, the authors propose a 3D dynamic optimal design method with hydraulic support and surrounding rock coupling, and subsequently the determination of the working resistance of hydraulic support at the No. 8105 coal face in Tashan mine in Datong, China, and test on site.

In terms of the study on mining equipment for LTCC operation, the improvement of the production rate at a fully mechanized coal face mainly depends on the increase of longwall width and shear cutting depth, fast advance and the extension of applicable range. In particular, the application of electromechanical heavy equipment enables the increase of the production rate, including high powered electric traction shearer, large capacity conveyor, electric-hydraulic controlled hydraulic support, non-stop self-moving stage loader and conveyor end, and high voltage power supply for face equipment. Currently the mining equipment manufactured in China for the fully mechanized longwall face and the LTCC face can meet the requirements and demands for high production and high efficiency in the Chinese coal industry.

In the early years, China imported a large amount of shearers including chain haulage type and hydraulic haulage type. Since the 1970s, China has started to manufacture shearers. In the eighties, the hydraulic haulage shearers met the requirements for extracting coal seams with heights from 1.5 to 4.5 m. In addition, the difficulties in integrating all mining equipment had been overcome. There were about 50 types of shearers. Up to the 1990s, large power hydraulic haulage shearer developed in China has gone into mass production. Furthermore, the high performance electric haulage shearer had been developed, and is currently at an advanced level in the world, with a cutting height of 5.5 m. In China, the application of large power electric haulage shearers enables the increase of coal production at a fully mechanized face from 1 Mtpa to 4 Mtpa or even 10 Mtpa. Currently, several series of electric haulage shearers are manufactured in China. In addition, the electric shearers are equipped with intelligent monitoring, control and protection systems, and applied with information processing and sensor technologies to achieve electro-mechanization.

Top-coal caving hydraulic support is a key equipment for LTCC operations. During the last 20 years, top-coal caving hydraulic support was gradually developed from high position top-coal caving support, middle position top-coal caving support, to low position top-coal caving support. Currently, the low position top-coal caving support is widely used, which is a chock-shield hydraulic support with positive four-link bar, reverse four-link bar and single swing link bar.

In terms of the scraper conveyor, there has been significant improvement every 10 years in China. In the 1980s, there were various types of scraper conveyors with two series of chute width of 730 mm and 764 mm. In 1994, the SGZ880/800 cross-side unloading scraper conveyor with an entirely cast-welded chute was developed by the Taiyuan Branch of China Coal Research Institute and Northwestern Mining Equipment Manufactory, which had a capacity of 7000 t/d. During the same period, Zhangjiakou Mining Equipment Manufactory introduced some casting and processing equipment and manufactured scraper conveyors with entirely cast-welding chutes.

During the period of the ninth five-year national economic plan, with the cooperation of Zhangjiakou and Northwestern Coal Mining Equipment Manufactory, using CAD technology, the Taiyuan Branch of China Coal Research Institute developed the first scraper conveyors for LTCC face with retractable end chain adjusting device. They were the SGZ960/750 front scraper conveyor and the SGZ900/750 rear scraper conveyor, and also stage loader and crusher. The equipment developed met the requirements from Yankuang Group for a coal production of 10,000–13,000 t/d. During the period of the tenth five-year national economic plan, Yankuang Group, the Taiyuan Branch of China Coal Research Institute and Northwestern Benniu Group jointly developed the SGZ1000/1200 and the SGZ1200/1400 long distance high reliability front scraper conveyor and rear scraper conveyor. Currently, the SFZ1200/1400 long distance high reliable rear scraper conveyor is an ultra-heavy scraper conveyor for LTCC faces, which is characterized by its highest power level, widest chute and longest length. Furthermore, it integrated various advanced technologies, including automatic extension of the conveyor end, hydraulic motor chain tensioner, speed adjustment hydraulic coupler and compact chain. In the 1990s, its main specifications reached an advanced level accepted worldwide. The SGZ1000/1200 front scraper conveyor is currently the largest front scraper conveyor, and can be integrated with various powerful shearers and hydraulic supports. Its installed power is $2 \times 600$ kW. The development of the SGZ1000/1200 and the SGZ1200/1400 scraper conveyors enables not only the technical advance in scraper conveyor technology, but also in LTCC technology.

In order to promote the development of large mining height LTCC technology and equipment for ultra-thick coal seams, and to achieve safe, high efficiency and high recovery mining of ultra-thick coal seams, in 2008, the Ministry of Science and Technology of China launched a significant R&D project called "the study of large mining height LTCC technology and equipment" The project was supported by the national science and technology plan. With 14–20 m thick coal seams, the project has developed a large mining height LTCC mining method (LLTCC mining method), a complete set of mining equipment, roadway drivage and support technology and equipment, and mine safety warrant technology and equipment (Wang 2013a, b). In 2011, the technologies and equipment developed were tested at the No. 8105 coal face of Tashan mine in Datong, China, with a production of 1.0849 Mtpa. The success of the project marked a new level for large mining height LTCC technology and equipment for ultra-thick coal seams in China. In this paper, the major research achievements, case studies and technical economical results from this project are presented.

## 2 Geological and mining conditions at the Tashan coal mine

### 2.1 Brief description of the mine

The Tashan coal mine is a large modern coal mine in Datong extracting the coals from Permo-Carboniferous system in the Datong coal field. The mine is located at the middle edge of Eastern Datong coal field in Shanxi Province, China, Fig. 1. The strike length of the mine is 24.3 km, the dip width is 11.7 km and the total area is 170.9 km$^2$. The mine extracts five coal seams including seam 2, 3, 4, 5 and 8. The mine has 5070 Mt of geological coal reserve, 4760 Mt of industrial coal reserve and 3070 Mt of mineable coal reserve. In 2007, the mine had a nominal production capacity of 1.5 Mtpa, and a life of 140 years.


**Fig. 1** Locality of Tashan coal mine

### 2.2 Geological conditions of the mine

The main coal seams extracted at Tashan coal mine are coal seam 3–5; their buried depth ranges from 347 to 447 m; average seam thickness is 16.8 m and maximum is 20 m; and average seam dip is 4°. The protodyakonov coefficient F of the coal seams ranges from 2.7 to 13.7. There are 4–14 plies partings, and their lithologies consist of grey brown kaolinite, kaolinitic mudstone, grey and black carbonaceous mudstone, sandy mudstone, and locally dark grey siltstone.

The top of coal seam 3–5 is a 0.33 m thick false roof of grey black carbonaceous mudstone. The top part of the immediate roof consists of brown grey kaolinitic mudstone, magmatic rock and the seam 2. The middle part of the immediate roof is composed of shed coal and silicified coal. The bottom part consists of grey black carbonaceous mudstone, kaolinite and magmatic rock. The thickness of the immediate roof ranges from 2.4 to 6.3 m. From top to bottom, the upper roof consists of seam 4, magmatic rock, silicified coal, siltstone, fine sandstone, kaolinitic mudstone and sandy mudstone. The thickness of the upper roof varies from 11.31 to 27.36 m. The immediate floor consists of grey brown kaolinitic mudstone and sandy mudstone. It is brittle, fragile and contains coal bits. The lower floor is dark grey siltstone with local fine sandstone. The length of the No. 8105 LLTCC face is 207 m. The face is affected by igneous rock. Thus, there are some metamorphism and silicification in the seam 3-5. The seam structure is complex. The coal with metamorphism and silicification is hard, broken and with well-developed cleats. Mixed coal is lose and fragile. A lower coal seam is stable and hard, and forms a structure like a sandwich, shown in Fig. 2.

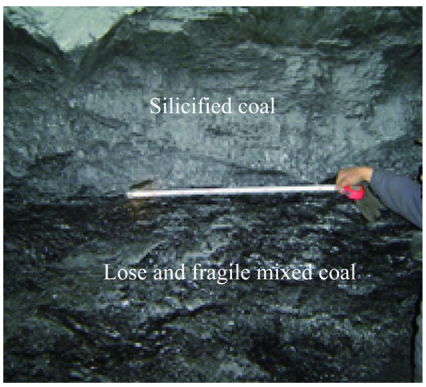


**Fig. 2** The upper seam structure at No. 8105 working face

**Table 1** Geotechnical measurement of surrounding rock at Tashan coal mine

| Order number | Measurement contents | Measurement instrument | Number of measurement points |
|---|---|---|---|
| 1 | Ground stress | SYY-56 ground stress monitor with hydraulic fracture | 3 holes |
| 2 | Rock strength | WQCZ-56 measurement instrument of rock strength | 8 holes |
| 3 | Rock structure | KDVJ-400 borehole camera | 13 holes |

**Table 2** Test results of ground stress

| Order number | Roadway name | Buried depth (m) | Vertical stress (MPa) | Maximum horizontal principal stress (MPa) | Minimum horizontal principal stress (MPa) | Direction of maximum horizontal principal stress |
|---|---|---|---|---|---|---|
| 1 | 1070 auxiliary transport roadway | 467 | 11.44 | 12.00 | 6.40 | N26.7°E |
| 2 | 5102 gate road | 467 | 11.44 | 12.40 | 8.22 | N24.8°E |
| 3 | 2102 gate road | 467 | 11.44 | 12.90 | 7.24 | N19.0°E |

The relative gas emission at coal seam 3–5 in Tashan coal mine is 1.95 $m^3$/t, which is classified as a low gas mine. However, the coal dust has the possibility of a dust explosion, with an explosion index of 37 %. The period of spontaneous combustion is 68 days. There is no high temperature heat hazard area. The geothermal gradient is 2.41 °C/100 m.

## 2.3 Geotechnical measurement and analysis of coal and rock masses

In order to fully understand the geotechnical properties of the surrounding rock, the measurement of geotechnical properties was systematically and comprehensively conducted, including the underground measurement of ground stress, rock strength test and rock structure observations. The measurement contents are listed in Table 1.

### *2.3.1 Measurement results of in situ stresses*

Using the hydraulic fracturing method, the in situ stress of rock in the roof of the seam 3–5 at Tashan coal mine was measured. The measurement results are shown in Table 2. These results show that the maximum horizontal principal stress is greater than the vertical principal stress. The type of stress field is the $\sigma_H > \sigma_V > \sigma_h$ type. Therefore, the stress field tested is mainly a structural stress field, and maximum horizontal principal stress is the principal stress.

### *2.3.2 Test results of surrounding rock strength*

The surrounding rock strength was directly measured in the borehole underground using the WQCZ-56 instrument. There were eight boreholes at four test stations, including four roof holes and four wall holes. Figures 3 and 4 show the test results in the No. 2102 roadway that was the closest station to the No. 8105 working face.

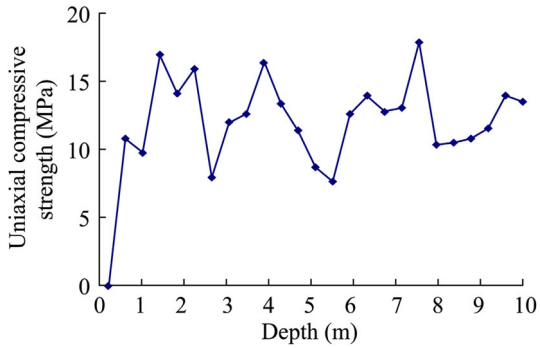


**Fig. 3** Test results of surrounding rock strength at roof of No. 2102 roadway

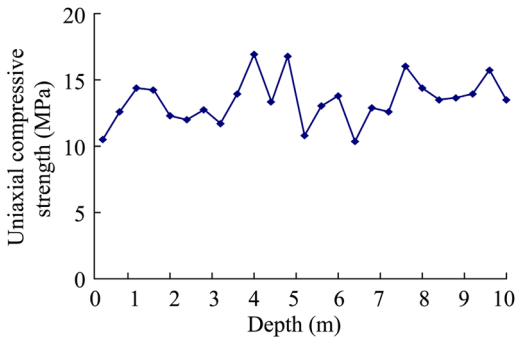


**Fig. 4** Test results of surrounding rock strength at wall of No. 2102 roadway

The test station was located in the No. 2102 roadway and 500 m away from the intersection of the No. 2102 roadway and the No. 1070 return airway. At this location, the roof holes and wall holes were all in coal seams and the coal strength was measured in detail. A 0.4 m fractured

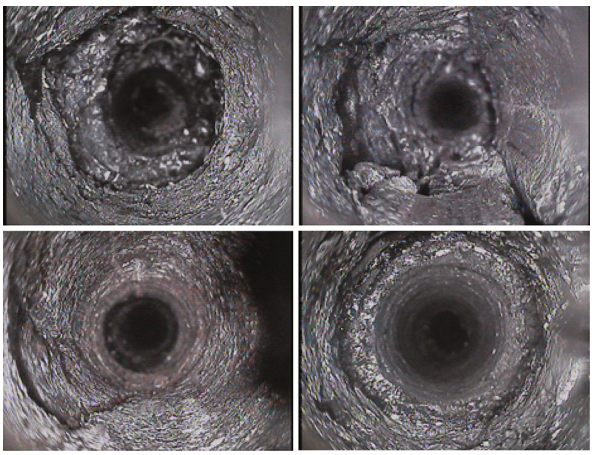

**Fig. 5** Typical photos inside boreholes at roof of roadway in Tashan coal mine

zone at roof holes was ignored and thus the maximum strength of the coal was 17.85 MPa, the minimum was 7.65 MPa, and the average was 12.43 MPa. The average coal strength in wall holes was 13.43 MPa.

*2.3.3 Observations of the surrounding rock structure*

The development of cleavage and fracture of the surrounding rock was directly observed in the boreholes underground using a KDVJ-400 borehole camera. The observations of 13 boreholes demonstrated that the cleavage and fracture in the top coal and immediate roof at the Tashan coal mine were well developed. In addition, there were various degree of layer separation at shallow roof strata and there was a trend to extend the layer separation into the upper strata. Figure 5 shows the photos of cleavage and fracture in boreholes.

## 3 Mining method and ground control technology for LLTCC operation in ultra-thick coal seams

### 3.1 LLTCC in ultra-thick coal seams

In a conventional fully mechanized top-coal caving longwall face, the coal cutting height is normally 3.0–3.5 m. Based on the rule of cutting to caving ratio 1:3, the conventional top-coal caving height is 9–10.5 m. In other words, the maximum thickness of coal extraction is 12–14 m. In terms of ultra-thick coal seams with thicknesses greater than 14 m, if the cutting height remains as 3.0–3.5 m, there will be many problems. For instance, the cutting to caving ratio will be too low (1:4.7 if cutting height is 3.5 m in a 20 m thick coal seam); it would be difficult to cave top coals, and the coal recovery will be low. At the same time, the increase of coal production will result in the increase of gas emission and the difficulties in removing gas due to limited cross-section area at the coal face.

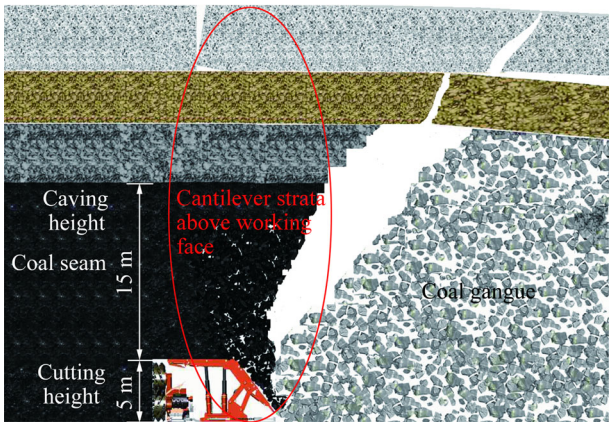


**Fig. 6** LLTCC mining method in ultra-thick coal seam

In order to overcome the problems mentioned above, the authors propose a LLTCC mining method, that is to increase the coal cutting height to 5 m, the top coal caving height to 15 m, and the total coal extraction height to 20 m, shown in Fig. 6. The LLTCC mining method involves a large coal cutting height, a large coal caving height and a large extraction space, that will result in some additional problems including coal wall spalling, difficulties in top-coal caving, and strong ground pressure. Those problems require comprehensive, in-depth and systematic research and testing.

### 3.2 3D spatial structural model of the roof in LLTCC mining

Because of the large thickness of the coal seam extracted through LLTCC mining in ultra-thick coal seams, the range of ground control should also be extended. After the completion of top coal caving operation, it is not possible for the roof rock to cave and fill in the goaf in a short time. Therefore, the immediate roof will form a "cantilever beam", and the upper roof will form a stable "articulated beam". In other words, a "cantilever beam–articulated beam" will be formed in a LLTCC coal face. In a general case, the overlying strata does not simply follow the movement from lower layer to upper layer, and instead forms various combinations of structures and moves with some laws. Figures 7 and 8 show the structural model of the roof.

Based on the study discussed above, a "cantilever beam–articulated beam" structural model for overlying strata at a LLTCC face has been developed, shown in Fig. 9. The strata that need to be controlled are the strata

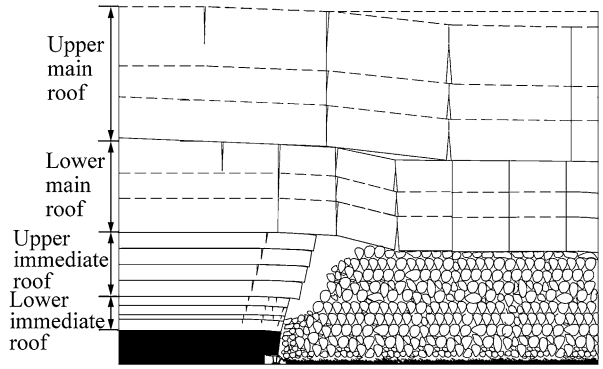


**Fig. 7** Strike cross-section of a LLTCC face

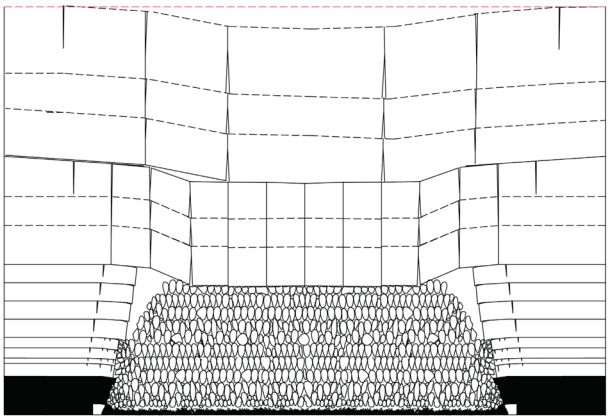

**Fig. 8** Dip cross-section of a LLTCC face

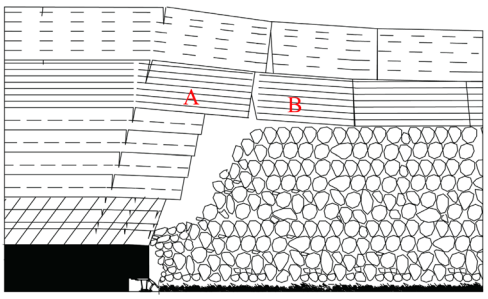


**Fig. 9** Structural model of "cantilever beam–articulated beam"

that cannot be supported by caved rocks before they cave. They are in the form of a "cantilever beam" and defined as immediate roof. Above the immediate roof, the strata that are supported by caved rocks are called the upper roof with an "articulated beam" structure. The roof strata satisfying the $\Delta_j - \Delta_m \leq 0$ condition are defined as immediate roof while the roof strata satisfying the $\Delta_j - \Delta_m > 0$ condition are defined as upper roof. $\Delta_j$ is the ultimate subsidence.

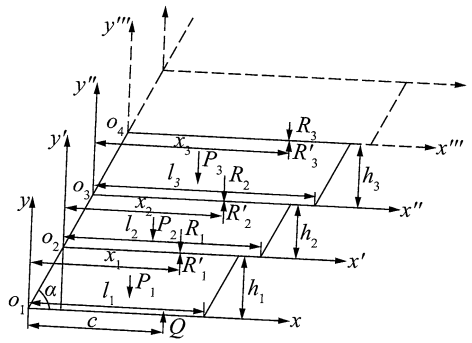

**Fig. 10** Force analysis and calculation of the immediate roof

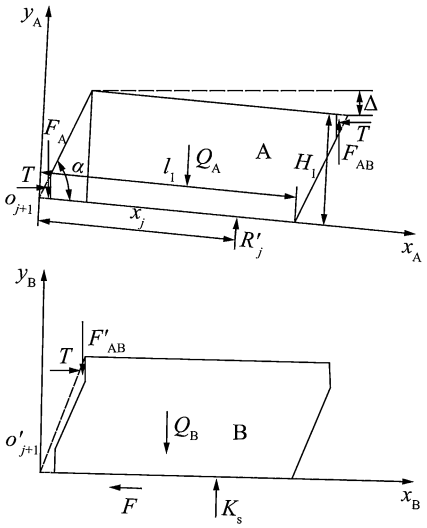

**Fig. 11** Force analysis of rock in main roof

$$\Delta_j = h - \frac{ql^2}{2kh\sigma_c} \tag{1}$$

where $h$ is the strata thickness analyzed, $k$ is a dimensionless coefficient ($k = 0.1\ h$), $q$ is the line load, $l$ is fracture length of the strata analyzed, $\sigma_c = (0.30 - 0.35)R_c$ ($R_c$ is compression strength), $\Delta_m$ is the possible subsidence (Yan 2009),

$$\Delta_m = (h_c + h_f)(1 - p_1) + (1 - k_P)h_m \tag{2}$$

where $p_1$ is the coal loss rate; $h_c$ is the coal-cutting height; $h_f$ is the coal caving height; $k_p$ is the expansion coefficient; $h_m$ is thickness of the immediate roof.

### 3.3 Determination of working resistance of the LLTCC hydraulic support

The top coal body of the LLTCC face in ultra-thick coal seams can be regarded as a "semi-rigid top coal body" that can transfer the roof deformation. The deformation effect

of the part of the immediate roof enables the top coal body becoming "semi-rigid top coal body". In terms of pressure on the support, this part of the strata can be called "no deformation pressure strata". Through the "semi-rigid top coal body", the pressure generated by the deformation of immediate roof and upper roof is transferred to hydraulic support. This part of the strata can be called "deformation pressure strata" (Yan 2009). The loads on the support are the combination of the weight of the top coal and the pressure generated by roof deformation. The force analysis of the immediate roof with deformation pressure is shown in Fig. 10. The force analysis of the upper roof is shown in Fig. 11.

(1) Force analysis of the immediate roof with deformation pressure.

According to $\sum M_{oi}= 0$ ($i = 1, 2, 3,\ldots, j$), get:

$$P_1\left(\frac{l_1}{2}+\frac{1}{2}h_1\text{ctan }\alpha\right)+R_1x_1-Qc=0$$

$$P_2\left(\frac{l_2}{2}+\frac{1}{2}h_2\text{ctan }\alpha\right)+R_2x_2-R_1'(x_1-h_1\text{ctan }\alpha)=0$$

$$P_3\left(\frac{l_3}{2}+\frac{1}{2}h_3\text{ctan }\alpha\right)+R_3x_3-R_2'(x_2-h_2\text{ctan }\alpha)=0$$

$$\ldots\ldots\ldots\ldots$$

$$P_j\left(\frac{l_j}{2}+\frac{1}{2}h_j\text{ctan }\alpha\right)+R_jx_j-R_{j-1}'\left(x_{j-1}-h_{j-1}\text{ctan }\alpha\right)=0$$

The $j$ formulas above are combined, and which will get:

$$Qc=\frac{1}{2}\sum_{i=1}^{j}P_i(l_i+h_i\text{ctan }\alpha)+\sum_{i=1}^{j-1}R_ih_i\text{ctan }\alpha+R_jx_j \tag{3}$$

where $Q$ is the deformation pressure on support, kN; c is the distance from resultant force of support to coal wall, m; $P_i$ is the rock weight of immediate roof of ith layer with deformation pressure, kN; $h_i$, $l_i$ are the rock thickness and length of the immediate roof of $i$th layer with deformation pressure respectively, m; $\alpha$ is the rock fissure angle, (°); $R_j$ is the additional force of upper strata, kN; $x_j$ is the distance from additional force of upper strata to caving point of $j$th layer immediate roof, m.

During the analysis of the large roof structure, the roof with deformation pressure is regarded as an entire body, and the interaction of internal layers can be ignored. Therefore, the Eq. (3) can be simplified as follows:

$$Qc=\frac{1}{2}\sum_{i=1}^{j}P_i(l_i+h_i\text{ctan }\alpha)+R_jx_j \tag{4}$$

(2) Analysis of rock A in main roof with deformation pressure.

During the analysis of rock A in main roof, assume that the broken distance of main roof A exceeding immediate roof $P_j$ is $h_j$ctan $\alpha$, thus, $\sum M_{j+1}=0$ to get:

$$R_jx_j=Q_A\left(\frac{L}{2}+\frac{1}{2}H\text{ctan }\alpha\right)-T(H-\Delta)-F_{AB}(L+H\text{ctan }\alpha) \tag{5}$$

where $Q_A$ is the weight of rock A in main roof with deformation pressure, kN; $T$ is the compression force between rocks, kN; $H$, $L$ is the strata thickness and broken distance of main roof with deformation pressure respectively, m; $\Delta$ is the subsidence of rock A in main roof with deformation pressure, m; $F_{AB}$ is the friction force between rock A and B, kN.

Substitute Eq. (2) into Eq. (3), to get:

$$Qc=\frac{1}{2}\sum_{i=1}^{j}P_i(l_i+h_i\text{ctan }\alpha)+Q_A\left(\frac{L}{2}+\frac{1}{2}H\text{ctan }\alpha\right)-T(H-\Delta)-F_{AB}(L+H\text{ctan }\alpha)$$

Assume $Q_A=P_{i+1}$, $L=l_{j+1}$, $H=h_{j+1}$, the equation above is simplified as:

$$Qc=\frac{1}{2}\sum_{i=1}^{j+1}P_i(l_i+h_i\text{ctan }\alpha)-T(h_{j+1}-\Delta)-F_{AB}\left(l_{i+1}+h_{j+1}\text{ctan }\alpha\right) \tag{6}$$

(3) Analysis of rock B in main roof.

Force balance in vertical direction:

$$F_{AB}'=Ks-Q_B \tag{7}$$

In Eq. (5), $F_{AB}'=Tf$, $F_{AB}'=F_{AB}$, therefore:

$$T=\frac{Ks-Q_B}{f} \tag{8}$$

where $K$ is the rigidity of gangue in goaf, N/m; $s$ is the compression of gangue in goaf, m, ($s=(k_1-k_2)\sum_{i=1}^{j}h_i, k_1$ is the expansion coefficient, $k_2$ is the residual expansion coefficient); $f$ is the friction coefficient among rocks; $Q_B$ is the weight of key block B in main roof (assume $Q_B=Q_A$), kN.

Substitute Eq. (8) into Eq. (6), to get:

$$Q = \frac{f\sum_{i=1}^{j+1} P_i(l_i + h_i \mathrm{ctan}\ \alpha) - 2(Ks - Q_B)(h_{j+1} + fl_{i+1} + fh_{i+1}\mathrm{ctan}\ \alpha - \Delta)}{2cf} \tag{9}$$

In summary, the calculation formula of hydraulic support for LLTCC mining is as follows:

$$P_z = K_d B(G_d + Q) = K_d B\left[L_d h_d \gamma_m + \frac{f\sum_{i=1}^{j+1} P_i(l_i + h_i \mathrm{ctan}\ \alpha) - 2(Ks - Q_B)(h_{j+1} + fl_{i+1} + fh_{i+1}\mathrm{ctan}\ \alpha - \Delta)}{2cf}\right] \tag{10}$$

where $P_z$ is the working resistance force of LLTCC support, kN; $K_d$ is the dynamic load coefficient; $G_d$ is the weight of top coal, kN; $B$ is the distance between the centers of two supports, m; $L_d$ is the distance of roof control, m; $h_d$ is the thickness of top coal, m; $\gamma_m$ is the bulk density of top coal, kN/m$^3$.

The equation for calculating the support external load obtained from the theoretical study discussed above was tested and validated at the No. 8105 coal face in Tashan coal mine in Datong, China. The borehole analyzed was WEI 1403 at the No. 8105 coal face in Tashan coal mine. Table 3 shows the structure of the strata in borehole, and Table 4 shows the physical and mechanical parameters.

The determination on the working resistance force of hydraulic support for LLTCC mining in ultra-thick coal seams:

(1) Based on criteria of immediate roof.
$\Delta_{mi}$ is the possible subsidence of $i$th layer, $i = 1, 2,\ldots,12$.

**Table 3** Structure of rock strata in WEI 1403 borehole

| Layer No. | Layer thickness (m) | Rock name | Layer No. | Layer thickness (m) | Rock name | Layer No. | Layer thickness (m) | Rock name |
|---|---|---|---|---|---|---|---|---|
| C1 | 4.49 | Mudstone | C22 | 2.40 | Siltstone | C43 | 7.25 | Coarse sandstone |
| C2 | 1.33 | Coal | C23 | 2.24 | Kaolinitic mudstone | C44 | 1.70 | Fine conglomerate |
| C3 | 2.97 | Sandy mudstone | C24 | 1.40 | Siltstone | C45 | 10.15 | Sandstone |
| C4 | 3.17 | Sandstone | C25 | 14.39 | Kaolinitic mudstone | C46 | 20.52 | Fine conglomerate |
| C5 | 15.67 | Sandy mudstone | C26 | 4.10 | Siltstone | C47 | 10.18 | Fine sandstone |
| C6 | 1.12 | Mudstone | C27 | 2.40 | Fine conglomerate | C48 | 4.95 | Siltstone |
| C7 | 1.78 | Coal | C28 | 3.70 | Coarse sandstone | C49 | 4.58 | Fine sandstone |
| C8 | 5.37 | Sandy mudstone | C29 | 3.00 | Siltstone | C50 | 2.16 | Fine conglomerate |
| C9 | 1.10 | Coarse sandstone | C30 | 14.13 | Sandy mudstone | C51 | 9.34 | Fine sandstone |
| C10 | 1.3 | Siltstone | C31 | 4.10 | Siltstone | C52 | 1.40 | Siltstone |
| C11 | 1.55 | Kaolinitic mudstone | C32 | 1.70 | Fine sandstone | C52 | 8.60 | Fine conglomerate |
| C12 | 5.03 | Siltstone | C33 | 7.96 | Sandy mudstone | C54 | 5.90 | Fine sandstone |
| C13 | 1.00 | Coarse sandstone | C34 | 2.66 | siltstone | C55 | 1.70 | siltstone |
| C14 | 1.10 | Siltstone | C35 | 1.65 | Fine sandstone | C56 | 1.00 | Fine sandstone |
| C15 | 5.37 | Kaolinitic mudstone | C36 | 3.50 | siltstone | C57 | 12.28 | Sandstone |
| C16 | 1.25 | Siltstone | C37 | 5.35 | Sandy mudstone | C58 | 10.20 | Siltstone |
| C17 | 2.93 | Coarse sandstone | C38 | 1.60 | Kaolinitic mudstone | C59 | 5.34 | Sandy mudstone |
| C18 | 0.90 | Siltstone | C39 | 0.65 | Coarse sandstone | C60 | 10.68 | Fine sandstone |
| C19 | 1.10 | Coarse sandstone | C40 | 13.64 | Siltstone | C63 | 122.56 | |
| C20 | 4.43 | Kaolinitic mudstone | C41 | 7.72 | Fine sandstone | to | | |
| C21 | 2.70 | Fine sandstone | C42 | 2.00 | Sandy mudstone | surface | | |

**Table 4** Lithological parameters of rock strata

| Rock strata | Volume force (kN/m$^3$) | Tensile strength (MPa) |
|---|---|---|
| Coal | 14.50 | 2.50 |
| Mudstone | 25.10 | 2.90 |
| Sandy mudstone | 26.20 | 3.10 |
| Kaolinitic mudstone | 25.13 | 3.30 |
| Siltstone | 25.80 | 5.10 |
| Fine sandstone | 26.50 | 4.30 |
| Sandstone | 24.10 | 3.70 |
| Fine conglomerate | 26.50 | 4.23 |
| Coarse sandstone | 25.80 | 4.10 |

$$\Delta_{m1} = 10.73\,\text{m}$$

$$\Delta_{j1} = h - \frac{ql^2}{kh\sigma_c} = 3.87\,\text{m} < \Delta_{m1}$$

Thus rock strata C1 is in the immediate roof.

……

$$\Delta_{m11} = 1.89\,\text{m}$$

$$\Delta_{j11} = h - \frac{ql^2}{kh\sigma_c} = 0.56\,\text{m} < \Delta_{m11}$$

Thus, rock strata C11 is in the immediate roof.

$$\Delta_{m12} = 0.63\ \text{m}$$

$$\Delta_{j12} = h - \frac{ql^2}{kh\sigma_c} = 4.32\ \text{m} > \Delta_{m12}$$

Thus, rock strata C12 and strata above are in the upper roof.

(2) Determination of rock strata without deformation pressure.

$\sum_{i=1}^{n} (\Delta_j)_i = \Delta_d$, $\Delta_d$ is a total deformation of coal body in roof control zone, $\Delta_d = \eta h_d(1+\lambda)$ (Yan 2009); $\eta$ is the porosity of top coal, $\eta = (1 - \gamma_d/\gamma) \times 100\,\%$, $\gamma_d$ is the dried bulk density of coal seam, $\gamma$ is the bulk density of coal seam, $\lambda$ is the coefficient of horizontal pressure (measured value at Tashan coal mine is 1.13).

$$\Delta_d = \eta h_d(1+\lambda) = 0.3 \times 10.61 \times (1+1.13)$$
$$= 6.78\,\text{m} \sum_{i=1}^{4}(\Delta_j)_i = 5.50\,\text{m} < \Delta_d;$$

$$\sum_{i=1}^{5} (\Delta_j)_i = 12.48\ \text{m} > \Delta_d;$$

Rock strata C5 is divided into two parts, $C5^{-1} = 10.17$ m, $C5^{-2} = 5.50$ m.

$$\sum_{i=1}^{5^{-1}} (\Delta_j)_i = \Delta_d$$

Thus rock strata C1–$C5^{-1}$ is rock strata without deformation pressure.

(3) Determination of working resistance force.

To maximize Eq. (10):

$$P_z = K_d B \left[ L_d h_d \gamma + \frac{f \sum_{i=1}^{j+1} P_i (l_i + h_i \cot\alpha)}{2cf} \right] \tag{11}$$

Analyze Table 3, refer to the mechanical property of each rock stratum, and take C12–C16 as a whole. Substitute the basic data of C5-2, C6, C7,…,C16 into Eq. (11), get:

$$P_z = K_d B \left[ L_d h_d \gamma + \frac{f \sum_{i=1}^{j+1} P_i (l_i + h_i \cot\alpha)}{2cf} \right]$$
$$= 1.6 \times 1.75 \times (923.07 + 4378.11)$$
$$= 14843.3\,\text{kN}$$

Therefore, based on the geotechnical conditions of rock strata at the Tashan coal mine, the working resistance force of hydraulic support for the No. 8105 LLTCC face at ultra-thick coal seam in Tashan coal mine was determined as 15,000 kN. The ZF15000/28/52 hydraulic support for LLTCC face was selected.

### 3.4 Analysis on the applicability of hydraulic support type

The dynamic change characteristics of the ZF15000/28/52 fully mechanized high strength LLTCC hydraulic support in a shift is shown in Fig. 12. The figure shows that the variation of working resistance was not large, implying that the support had a very high reliability.

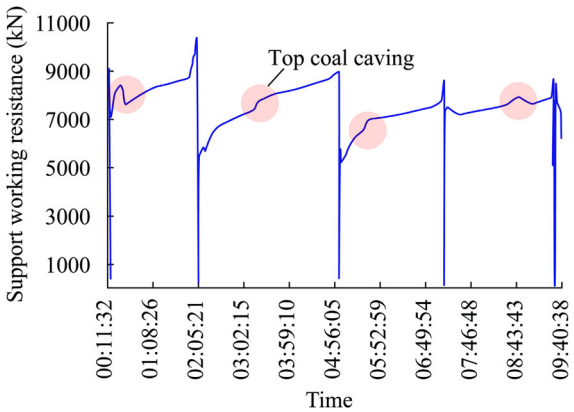


**Fig. 12** Periodical change of support working resistance at the middle of the face

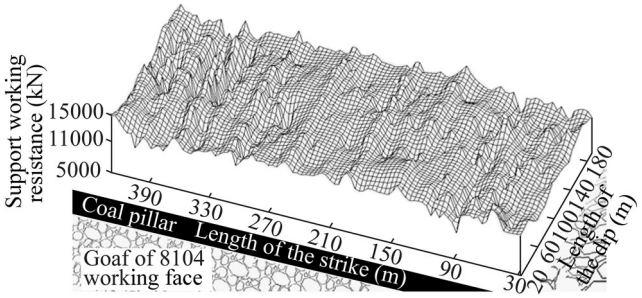


**Fig. 13** Distribution of ground pressure at the working face

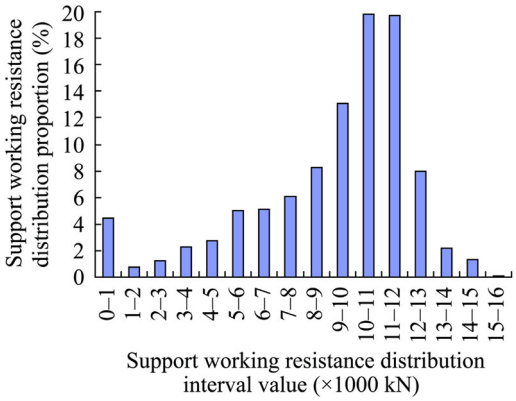


**Fig. 14** Histogram of support working resistance

Figure 13 shows the 3D support resistance variation at the end of the circle in the No. 8105 face. The impact range of the initial caving and periodical caving of the upper roof was extensive and covered the whole working face. In a normal working period, the average working resistance is 9073.06 kN. Table 5 shows that there was almost no effect on supports, although the dynamic load coefficient is large during loading period, indicating that the impact resistance of support is high. When load is high, and the working resistance force exceeds nominal resistance force, the relief valve can be activated in a timely manner, showing the stability of the support is good.

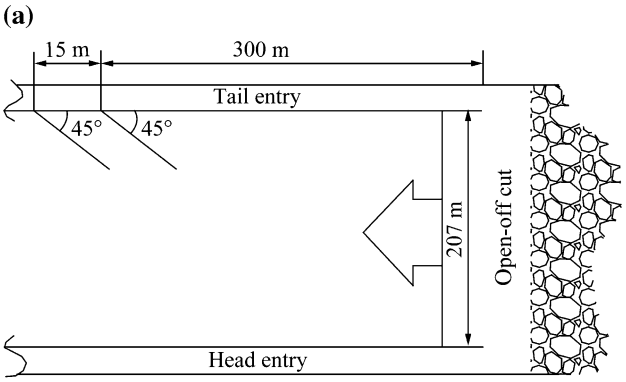


**Fig. 15** Boreholes layout. **a** Top view of boreholes layout, **b** vertical cross-section diagram

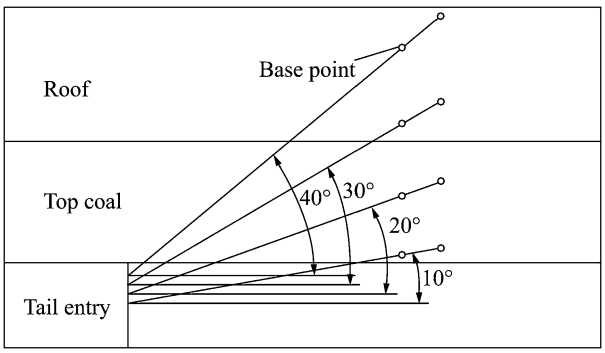


**Fig. 16** Layout of deep base points

**Table 5** Statistics of dynamic loading coefficient of upper roof

| Support No. | 20 | 21 | 63 | 64 | 95 | 96 |
|---|---|---|---|---|---|---|
| Dynamic loading coefficient at initial loading | 1.51 | 1.57 | 1.56 | 1.58 | 1.62 | 1.49 |
| Average dynamic loading coefficient at initial loading | 1.56 | | | | | |
| Dynamic loading coefficient at Ith periodical loading | 1.43 | 1.58 | 1.58 | 1.58 | 1.49 | 1.50 |
| Dynamic loading coefficient at IIth periodical loading | 1.54 | 1.58 | 1.57 | 1.56 | 1.55 | 1.46 |
| Dynamic loading coefficient at IIIth periodical loading | 1.30 | 1.51 | 1.66 | 1.41 | 1.41 | 1.40 |
| Dynamic loading coefficient at IVth periodical loading | 1.38 | 1.51 | 1.64 | 1.52 | 1.59 | 1.37 |
| Dynamic loading coefficient at Vth periodical loading | 1.44 | 1.52 | 1.63 | 1.56 | 1.57 | 1.46 |
| Average dynamic loading coefficient at periodical loading | 1.43 | 1.55 | 1.61 | 1.54 | 1.54 | 1.45 |
| Total average dynamic loading coefficient at periodical loading | 1.52 | | | | | |

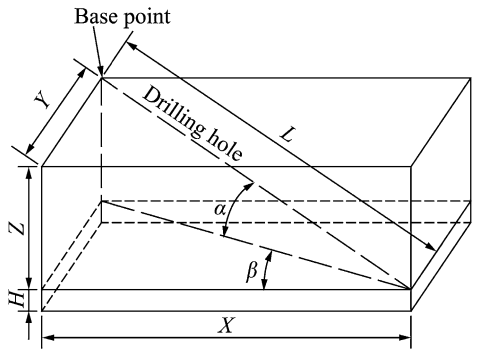


**Fig. 17** Geometry of deep base point parameters

The percentage of support resistance at different intervals was described as a histogram (Fig. 14). Figure 14 shows that the distribution of working resistance of hydraulic support was rational, and appeared as a distribution of sine wave. The support resistance was mostly within 8000–13,000 kN. In summary, the selection of support was reasonable and their utilization was high. The support selected was suitable for the roof conditions in the working face.

### 3.5 Analysis of the characteristics of top coal and roof movement in a LLTCC coal face

In order to study the movement law of top coal and roof at a LLTCC coal face, some boreholes were drilled into the top coal and roof of the tailgate at the No. 8105 LLTCC coal face in Tashan coal mine. Basic anchors were installed at different layers inside the boreholes. GUW300 tracking instruments were installed at the opening of the boreholes. The first monitoring station was setup at the location 300 m away from the box cut of the No. 8105 face. The second monitoring station was 15 m away from the first station. At each station, four boreholes were drilled into the top coal and roof, two deep base points were installed inside each hole, eight deep base points in total were installed, and four GUW300 deep base point movement tracking instruments were installed. The intersection angle of borehole and tailgate was 45°. The angles of from No. 1 to No. 4 boreholes with horizontal level were 40°, 30°, 20° and 10° respectively. The heights of borehole positions from No. 1 to No. 4 with floor were 2.4, 2.1, 1.8 and 1.5 m respectively. Figure 15 shows the layout of the boreholes. Figure 16 shows the layout of eight deep base points in each monitoring station with four points in the top coal and four points in the roof (Table 5).

Figure 17 shows the basic parameter geometry of the boreholes layout. Tables 6 and 7 show the parameters of deep base points. Basic geometry is described as Eq. (12).

$$X = \sqrt{(L\cos\ \alpha)^2 - (L\sin\ \beta)^2} \tag{12}$$

where $L$ is the depth of base point, m; $\alpha$ is the angle of elevation, (°); $\beta$ is the angle between borehole and tailgate, (°); $X$ is the horizontal length from borehole opening to deep base point and parallel to tailgate, m; $Y$ is the horizontal length from borehole opening to deep base point and perpendicular to tailgate, m; $Z$ is the vertical height from floor to deep base point, m; $H$ is the vertical height from floor to borehole opening, m.

From Figs. 18, 19, 20 and 21 show the movement of top coal and roof from two monitoring stations at the No. 8105 working face.

As shown from Figs. 18, 19, 20 and 21, among the initial displacement positions of eight top coal deep base points at two monitoring stations, the distance ahead of the coal wall at the working face ranged from 34 to 48 m with an average of 38 m; among the initial displacement positions of roof deep base points, the maximum distance ahead of the coal wall at the working face ranged from 22 to 34 m, with an average of 28.6 m.

The average measured displacement at the top coal base points in front of the coal wall was 114.88 mm, accounting for 26.6 % of total displacement. The average measured displacement at the top coal base points behind coal wall was

**Table 6** Parameters from first monitoring station

| Hole No. | Height from floor to hole opening (m) | Base point No. | Angle of elevation (°) | Height to floor (m) | Height to hole opening (m) | Depth to base point (m) | Horizontal projection of base point (m) | Distance of tailgate projection (m) |
|---|---|---|---|---|---|---|---|---|
| 1 | 2.4 | 11 | 40 | 32.1 | 29.7 | 46.2 | 35.4 | 25.0 |
| | | 12 | | 26.1 | 23.7 | 37.0 | 28.3 | 20.0 |
| 2 | 2.1 | 21 | 30 | 22.5 | 20.4 | 40.9 | 35.4 | 25.0 |
| | | 22 | | 18.4 | 16.3 | 32.7 | 28.3 | 20.0 |
| 3 | 1.8 | 31 | 20 | 14.7 | 12.9 | 37.7 | 35.4 | 25.0 |
| | | 32 | | 12.1 | 10.3 | 30.1 | 28.3 | 20.0 |
| 4 | 1.5 | 41 | 10 | 7.7 | 6.2 | 35.9 | 35.4 | 25.0 |
| | | 42 | | 6.5 | 5.0 | 28.7 | 28.3 | 20.0 |

**Table 7** Parameters from second monitoring station

| Hole No. | Height from floor to hole opening (m) | Base point No. | Angle of elevation (°) | Height to floor (m) | Height to hole opening (m) | Depth to base point (m) | Horizontal projection of base point (m) | Distance of tailgate projection (m) |
|---|---|---|---|---|---|---|---|---|
| 1 | 2.4 | 11 | 40 | 32.1 | 29.7 | 46.2 | 35.4 | 25.0 |
| | | 12 | | 26.1 | 23.7 | 37.0 | 28.3 | 20.0 |
| 2 | 2.1 | 21 | 30 | 22.5 | 20.4 | 40.9 | 35.4 | 25.0 |
| | | 22 | | 18.4 | 16.3 | 32.7 | 28.3 | 20.0 |
| 3 | 1.8 | 31 | 20 | 14.7 | 12.9 | 37.7 | 35.4 | 25.0 |
| | | 32 | | 12.1 | 10.3 | 30.1 | 28.3 | 20.0 |
| 4 | 1.5 | 41 | 10 | 7.7 | 6.2 | 35.9 | 35.4 | 25.0 |
| | | 42 | | 6.5 | 5.0 | 28.7 | 28.3 | 20.0 |

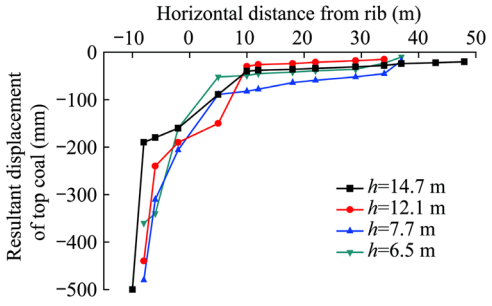


**Fig. 18** Top coal displacement at first monitoring station

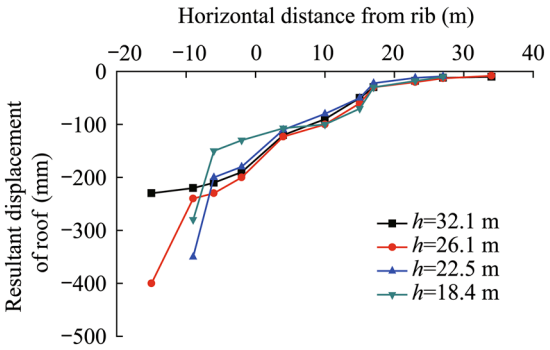


**Fig. 21** Roof displacement at second monitoring station

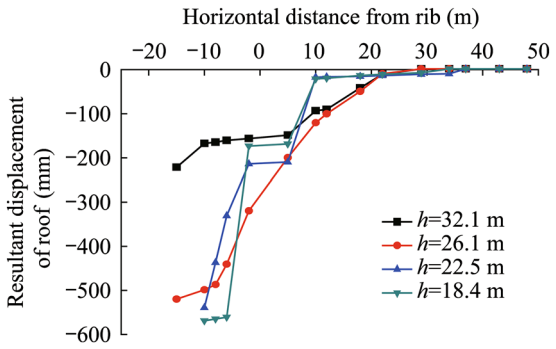


**Fig. 19** Roof displacement at first monitoring station

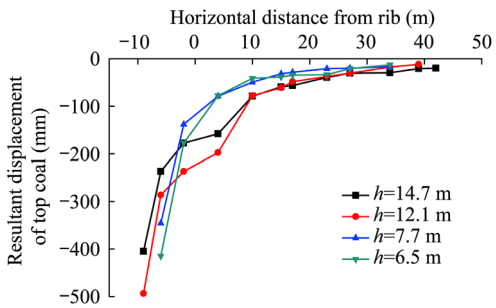


**Fig. 20** Top coal displacement at second monitoring station

317.63 mm, accounting for 73.4 % of total displacement. The total displacement was 432.5 mm. Average measured displacement at the roof base points in front of the coal wall was 149 mm, accounting for 38.3 % of the total displacement. Average measured displacement at roof base points behind coal wall was 240.25 mm, accounting for 61.7 % of total displacement. The total displacement was 389.25 mm. Although from initial displacement position, the top coal base points were affected by abutment pressure in front of the face, that lasted a long period and affected a long distance, the accumulated displacement of the top coal and roof was relatively small due to the constraint from limited space before entering the roof control zone. After entering the roof control zone, the movement of the top coal and roof followed the movement law of vertical subsidence after caving.

In front of the coal wall at the working face, the movement of the top coal and roof mainly showed a horizontal deformation under the abutment pressure due to the vertical constraints of the top coal and roof. At the rear of the coal wall which was under the repeated loading and unloading actions, the vertical constraints on the lower part of the top coal exhibited subsidential weakening with the advance of coal cutting resulting in a large space. Therefore, the movement of roof appeared as fracture subsidence and the movement of the top coal appeared as vertical

displacement caused by the roof fracture subsidence. There was a large difference in accumulated top coal and roof displacement in the front and in the rear of the coal wall. In addition, the difference of displacement per unit advance was relatively large. The displacement rate of the top coal in front of the coal wall was 2.63 and 42.29 mm/m at rear of the coal wall. The displacement rate of the roof in front of the coal wall was 5.4 mm/m, and 21.35 mm/m at rear of coal wall. It demonstrated that the horizontal deformation rate of the top coal and roof caused by abutment pressure in front of the coal wall was much less than the vertical subsidence rate of the top coal and roof at rear of coal wall.

At eight base points in the top coal in two monitoring stations, from the coal wall to the gulf, the distance between the caving position to the coal wall ranged between 6 and 10 m, with an average of 7.8 m. Assume the average distance of the roof control was 6.5 m, the average caving position of the top coal was greater than the average distance of the roof control. In particular, the average caving position was 9 m in the middle or upper part of the top coal ($h = 12.1$ m, or $h = 14.7$ m), that indicated that there was a delay of the middle or upper part of top coal caving, the average distance of delay was 2.5 m, and the top coal was caved in a form of inverted step. From the point view of eight base points at two monitoring stations, the roof base points at $h = 18.4$ m, $h = 22.5$ m and $h = 26.1$ m caved in time with the top coal caving. The displacement of the roof started to increase at the roof base point of $h = 32.1$ m and 15 m at the rear of the coal wall. Therefore, the immediate roof was not completely caved or caved on time, and formed an immediate roof in the form of a cantilever beam above the coal seam. Based on the position of the top coal caving, the caving angle of the top coal can be approximately calculated, i.e., 64.3° for the first monitoring station, 70.1° for the second monitoring station, and 67.2° for an average caving angle.

### 3.6 Spalling of coal wall at a LLTCC coal face

#### *3.6.1 Factors of coal wall spalling at a LLTCC coal face*

At different stages of non-periodical ground pressure and periodical pressure, as the differences in mining height, advance speed and distance from the support tip to the coal wall, the spalling depth and spalling ratio were different at a LLTCC coal mining face (Yan 2008; Yin et al. 2008; Zhang et al. 2010). In order to better understand the spalling mechanism at a LLTCC coal mining face, the coal wall spalling were examined under different conditions including mining heights, advance rates, distances from the support tip to the coal wall, and ground pressure stages.

Using the numerical simulation method, the horizontal displacements of the coal wall with mining heights of 3.5, 4.5, 5.0 and 5.5 m were simulated and the results are shown in Fig. 22.

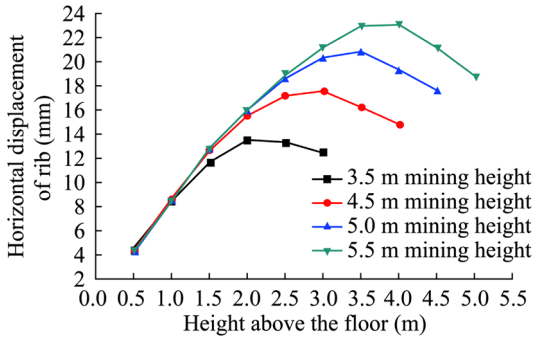


**Fig. 22** Horizontal displacements of rib with different mining heights

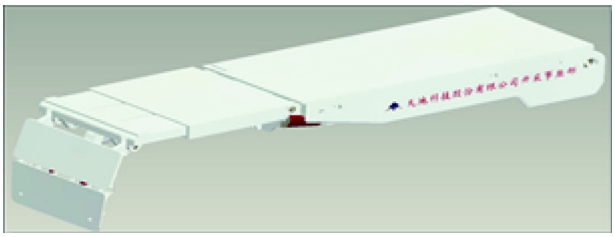

**Fig. 23** Structure of the second level wall guard plate installed on the extendable beam

Figure 22 showed that the peak horizontal displacement increased with the increase of mining height. Considering the normal mining height was 4.0–4.5 m, the point of peak horizontal displacement to floor was approximately 2.5–3.0 m. Therefore, the rational height of the wall guard plate of support was 1.5 m. Based on simulated results, the second level wall guard plate was installed on a high reliable extendable beam and articulated front beam to prevent the spalling of the coal wall. Its structure is shown in Fig. 23.

The face advance speed also significantly affected wall spalling. The observations at the No. 8105 coal face demonstrated that with the increase of face advance speed, there was a reduction of damage area around the coal wall, and a reduction of wall horizontal displacement. In other words, the spalling of coal wall was suppressed. It is therefore suggested that the face advance speed should be rationally increased to reduce the exposure time and spalling of coal wall. Nevertheless, the effectiveness of controlling coal wall spalling was limited through the increase of face advance speed. With a large amount of observations on site, the effect of increasing face advance speed on coal wall spalling was found. If the advance speed is too high, the coal spalling might increase.

With the increase of the distance from support tip to coal wall, the peak abutment pressure in front of the face

decreased. Subsequently, the displacement at support tip increased significantly, and the damage zone in front of the face also increased, redulting in significant spalling. Undoubtedly, the distance from the support tip to the coal wall should be reduced appropriately.

Coal cutting height, face advance speed and distance from support tip to coal wall were three factors that had substantial effects on coal wall spalling. Their weighted effects might be ordered as coal cutting height > face advance speed > distance from support tip to coal wall.

The effect on coal wall spalling from the caving and displacement of the top coal and the roof had an obvious regular pattern. The coal wall spalling clearly appeared before ground pressure commenced, increasing to maximum with ground pressure, and decreased to a minimum after ground pressure disappeared. During periodical ground pressure, the average spalling ratio of the coal wall increased to 24.58 %. With a low face advance speed, the effect on coal wall spalling would be obvious from periodical ground pressure. Therefore, the maintenance of the coal wall should be enhanced during the period of periodical pressure occurring.

The seriousness of coal wall spalling is different at different positions. Coal wall spalling was found to be most serious at the middle part of the face, less serious at the lower part of the face and better at the upper part of the face.

According to the observation at the No. 8105 LLTCC face, the position of peak abutment pressure in front of the coal face was between 10 and 25 m, the relative stress concentration coefficient $k$ was 1.3–6.5 during the peak period, and the average was 2.13. From the 10–25 m zone in front of the coal face to the coal wall was the stress release zone, and the effected zone by abutment pressure was 80 m.

With the analysis on the characteristics of coal wall spalling at the LLTCC face under different conditions, including mining height, face advance speed, distance from support tip to coal wall, ground pressure, and different positions at the coal face, the authors have developed a comprehensive spalling control technology of controlling the face advance speed, increasing initial support power, and improving the support capacity for wall protection. The technology developed has been tested and applied at the No. 8105 coal face.

### 3.6.2 *Observation plan of coal wall spalling at the No. 8105 face*

The observation of coal wall spalling consisted of two aspects:

(1) During the non-periodical pressure period, under different face advance speeds, the coal wall spalling ratio and depth are at different positions of the face.

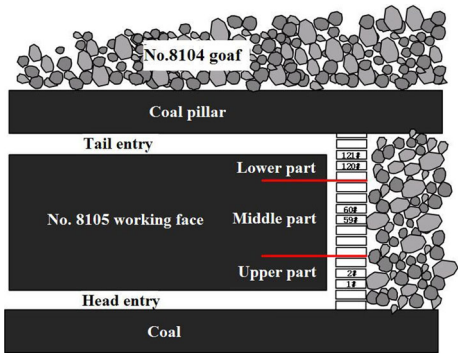


**Fig. 24** Observation plan

(2) During the periodical pressure period, under different face advance speeds, the coal wall spalling ratio and depth are at different positions of the face.

The observation plan of coal wall spalling was as follows: the length of the No. 8105 face was 207 m, and the number of supports was 121. The face was divided into three observation zones including upper part, middle part and lower part (upper part: No. 1–No. 30 supports, middle part: No. 31–No. 89 supports and lower part: No. 90–No. 121 supports). Figure 24 shows the observation zones.

### 3.6.3 *Analysis of coal wall spalling during non-periodical pressure period*

(1) Coal wall spalling at the upper part of the face.
Observation results of coal wall spalling at the upper part of the face (non-periodical pressure period) are shown in Table 8 and Fig. 25.
In the non-periodical ground pressure period, the depth of coal wall spalling increased with the face advance speed at the upper part of the face, and eventually maintained at a certain depth range. When the face advance speed reached 3.05 m/d, the coal wall spalling length and depth reached their maximum values of 35 m and 0.6 m respectively, and the maximum spalling ratio was 66.67 %. The relationship between spalling length, depth, ratio and the face advance speed displayed a significant range. But generally, the values tended to increase with the face advance speed.

(2) Coal wall spalling in the middle part of the face.
Observation results of coal wall spalling at the middle part of the face (non-periodical pressure period) are shown in Table 9 and Fig. 26.
During the non-periodical pressure period, being similar to the coal wall spalling at the upper part of the face, the depth of coal wall spalling decreased with the increase of face advance speed in the middle

**Table 8** Characteristics of coal wall spalling at the upper part of the face (non-periodical ground pressure period)

| Face advance speed (m/d) | Average spalling depth (m) | Spalling length (m) | Spalling ratio (m) | Maximum spalling depth (m) |
|---|---|---|---|---|
| 2.05 | 0 | 0 | 0 | 0 |
| 2.25 | 0 | 0 | 0 | 0 |
| 2.25 | 0.40 | 31.50 | 60.00 | 0.50 |
| 2.40 | 0.35 | 31.50 | 60.00 | 0.50 |
| 3.00 | 0.20 | 14.00 | 26.67 | 0.30 |
| 3.05 | 0.40 | 35.00 | 66.67 | 0.60 |
| 3.10 | 0.35 | 22.75 | 43.33 | 0.60 |
| 3.15 | 0 | 0 | 0 | 0 |
| 3.40 | 0.35 | 7.00 | 13.33 | 0.40 |
| 3.60 | 0 | 0 | 0 | 0 |
| 3.85 | 0.30 | 1.75 | 3.33 | 0.30 |
| 3.90 | 0.30 | 17.50 | 33.33 | 0.40 |
| 4.00 | 0.40 | 17.50 | 33.33 | 0.40 |
| 4.50 | 0.25 | 17.50 | 33.33 | 0.40 |
| 4.60 | 0 | 0 | 0 | 0 |
| 4.75 | 0.25 | 1.75 | 3.33 | 0.30 |
| 5.00 | 0.30 | 28.00 | 53.33 | 0.30 |
| 5.40 | 0.30 | 26.25 | 50.00 | 0.50 |
| 5.50 | 0.25 | 14.00 | 26.67 | 0.30 |
| 5.65 | 0 | 0 | 0 | 0 |
| 5.75 | 0.20 | 12.25 | 23.33 | 0.30 |
| 6.00 | 0.25 | 14.00 | 26.67 | 0.30 |
| 6.15 | 0 | 0 | 0 | 0 |
| 6.25 | 0 | 0 | 0 | 0 |
| 6.50 | 0 | 0 | 0 | 0 |
| 7.00 | 0 | 0 | 0 | 0 |
| 8.50 | 0.30 | 15.75 | 30.00 | 0.50 |

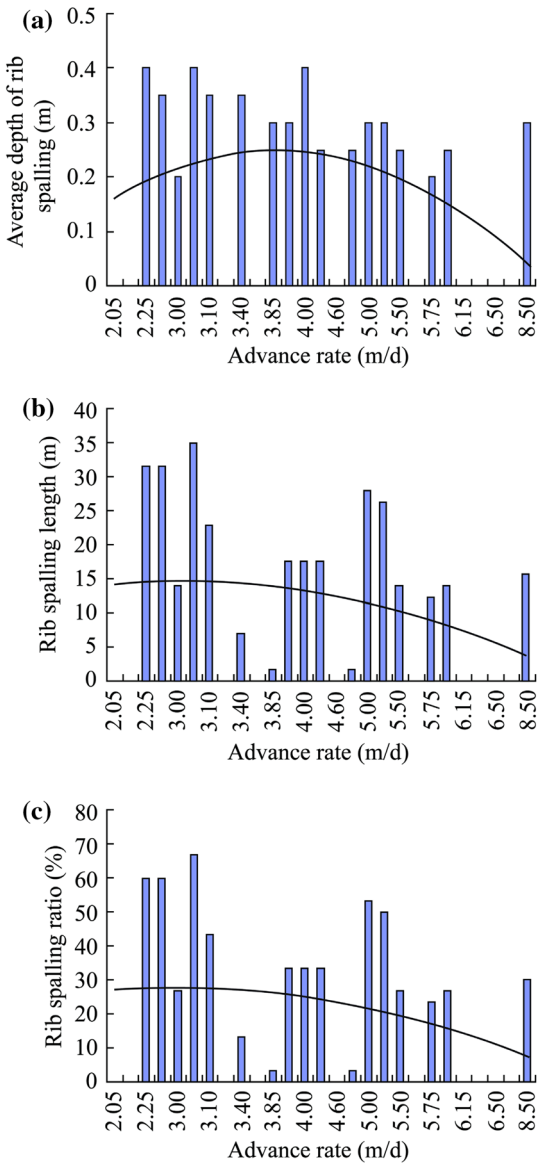


**Fig. 25** Relationship *curves* between coal wall spalling and face advance speed at the upper part of the face (non-periodical ground pressure). **a** Relationship between average rib spalling depth and face advance rate, **b** relationship between rib spalling length and face advance rate, **c** relationship between rib spalling ratio and face advance rate

part of the face, the spalling ratio showed a trend of non-linear decrease with the increase of face advance speed.

(3) Coal wall spalling at the lower part of the face.

Observation results of coal wall spalling at the lower part of the face (non-periodical pressure period) are shown in Table 10 and Fig. 27.

During the non-periodical pressure period, at the lower part of the face, the relationship between coal wall spalling and face advance speed showed a certain degree of randomness. When the face advance speed reached 2.4, 3.05, 5, 5.5 and 5.75 m/d, there was no spalling occurring. In general, the depth of coal wall spalling showed less variation with face advance speed at the lower part of the face, the average spalling depth concentrated within 0.3–0.4 m. With the increase of face advance speed, the spalling length and ratio showed a trend of decrease early, to increase at a later time.

(4) Comparison of coal wall spalling at different face positions during non-periodical ground pressure period.

Figure 28 shows the comparison of the depth of coal wall spalling at different face positions during non-periodical ground pressure period. Table 11 lists the

**Table 9** Characteristics of coal wall spalling in the middle part of the face (non-periodical ground pressure period)

| Face advance speed (m/d) | Average spalling depth (m) | Spalling length (m) | Spalling ratio (%) | Maximum spalling depth (m) |
|---|---|---|---|---|
| 2.05 | 0.30 | 29.75 | 28.81 | 0.40 |
| 2.25 | 0.30 | 24.50 | 23.73 | 0.30 |
| 2.40 | 0.35 | 22.75 | 22.03 | 0.50 |
| 3.00 | 0.35 | 28.00 | 27.12 | 0.60 |
| 3.05 | 0.40 | 42.00 | 40.68 | 0.60 |
| 3.10 | 0.40 | 15.75 | 15.25 | 0.70 |
| 3.15 | 0.45 | 21.00 | 20.34 | 0.70 |
| 3.40 | 0.35 | 31.50 | 30.51 | 0.50 |
| 3.60 | 0.35 | 50.75 | 49.15 | 0.50 |
| 3.85 | 0.30 | 33.25 | 32.20 | 0.30 |
| 3.90 | 0.35 | 26.25 | 25.42 | 0.50 |
| 4.00 | 0.30 | 17.50 | 16.95 | 0.30 |
| 4.50 | 0.30 | 50.75 | 49.15 | 0.40 |
| 4.60 | 0.25 | 14.00 | 13.56 | 0.30 |
| 4.75 | 0.30 | 12.25 | 11.86 | 0.40 |
| 5.00 | 0.40 | 8.75 | 8.47 | 0.40 |
| 5.40 | 0.30 | 22.75 | 22.00 | 0.40 |
| 5.50 | 0.20 | 15.75 | 15.25 | 0.20 |
| 5.65 | 0.30 | 14.00 | 13.56 | 0.30 |
| 5.75 | 0.35 | 29.75 | 28.81 | 0.50 |
| 6.00 | 0.35 | 19.25 | 18.64 | 0.30 |
| 6.15 | 0.30 | 26.25 | 25.42 | 0.40 |
| 6.25 | 0.20 | 7.00 | 6.78 | 0.30 |
| 6.50 | 0.30 | 33.25 | 32.20 | 0.30 |
| 7.00 | 0.20 | 8.75 | 8.47 | 0.30 |
| 8.50 | 0.25 | 7.00 | 7.00 | 0.40 |

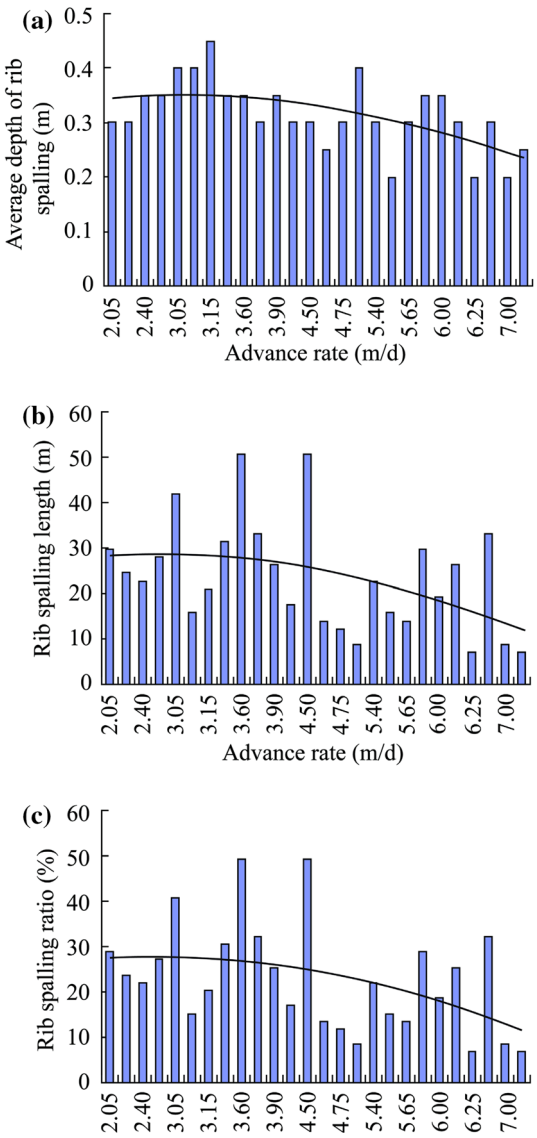


**Fig. 26** Relationship *curves* between coal wall spalling and face advance speed in the middle part of the face (non-periodical ground pressure). **a** Relationship between average rib spalling depth and face advance rate, **b** relationship between rib spalling length and face advance rate, **c** relationship between rib spalling ratio and face advance rate

statistical analysis results of coal wall spalling at different face positions during the non-periodical ground pressure period. Based on the analysis and comparison, the spalling depth was 0.2 m at the upper part of the face, 0.32 m in the middle part of the face and 0.26 m at the lower part of the face, suggesting that the spalling depth was deepest in the middle part of the face, less deep at the lower part and least deep at the upper part.

Figure 29 shows the comparison of the spalling ratios at different face positions during the non-periodical ground pressure period. The spalling ratio showed a trendency of reduction with the increase of face advance speed during the non-periodical ground pressure period. As shown in Table 12, the coal wall spalling ratio was 22.56 % at the upper part of the face, 22.81 % in the middle part of the face, and 19.05 % at the lower part of the face, that indicated that the spalling ratio was largest in the middle of the face, less at the upper part of the face, and the least at the lower part of the face.

### *3.6.4 Analysis of coal wall spalling during the periodical ground pressure period*

(1) Coal wall spalling at the upper part of the face.

Observation results of coal wall spalling at the upper part of the face (during the periodical ground pressure period) are shown in Table 13 and Fig. 30.

During the period of ground pressure, the spalling

**Table 10** Characteristics of coal wall spalling at the lower part of the face (non-periodical ground pressure period)

| Face advance speed (m/d) | Average spalling depth (m) | Spalling length (m) | Spalling ratio (%) | Maximum spalling depth (m) |
|---|---|---|---|---|
| 2.05 | 0.30 | 26.25 | 46.88 | 0.40 |
| 2.25 | 0.25 | 24.50 | 43.75 | 0.30 |
| 2.40 | 0 | 0 | 0 | 0 |
| 3.00 | 0.45 | 8.75 | 15.63 | 0.70 |
| 3.05 | 0 | 0 | 0 | 0 |
| 3.10 | 0.20 | 15.75 | 12.50 | 0.30 |
| 3.15 | 0.45 | 21.00 | 20.34 | 0.70 |
| 3.40 | 0.35 | 8.75 | 15.63 | 0.50 |
| 3.60 | 0.40 | 14.00 | 25.00 | 0.50 |
| 3.85 | 0.30 | 7.00 | 12.50 | 0.30 |
| 3.90 | 0.35 | 8.75 | 15.63 | 0.50 |
| 4.00 | 0.30 | 12.25 | 21.88 | 0.30 |
| 4.50 | 0.30 | 21.00 | 37.50 | 0.40 |
| 4.60 | 0.25 | 10.50 | 18.75 | 0.30 |
| 4.75 | 0.30 | 3.50 | 6.25 | 0.40 |
| 5.00 | 0 | 0 | 0 | 0 |
| 5.40 | 0.30 | 19.25 | 34.00 | 0.40 |
| 5.50 | 0 | 0 | 0 | 0 |
| 5.65 | 0.40 | 8.75 | 15.63 | 0.50 |
| 5.75 | 0 | 0 | 0 | 0 |
| 6.00 | 0.50 | 14.00 | 25.00 | 0.70 |
| 6.15 | 0.30 | 17.50 | 31.25 | 0.40 |
| 6.25 | 0.25 | 15.75 | 28.13 | 0.40 |
| 6.50 | 0.30 | 14.00 | 25.00 | 0.30 |
| 7.00 | 0.30 | 15.75 | 28.13 | 0.40 |
| 8.50 | 0.30 | 8.75 | 16.00 | 0.40 |

depth, spalling length and spalling ratio at the upper part of the face had a similar variation trendency with the increase of face advance speed, i.e., increase early and decrease later. When the face advance speed reached 5.50 m/d, the spalling ratio was the largest at the upper part of the face at 63.33 %.

(2) Coal face spalling in the middle part of the face. Observation results of coal wall spalling at the middle part of the face (during the periodical ground pressure period) are shown in Table 14 and Fig. 31. During the period of periodical ground pressure, the spalling depth presented a trend of decrease early on, and increasing later with the increase of face advance speed. The spalling length and ratio presented a trend of gradual reduction with the face advance speed. In the middle part of the face, the spalling depth was 0.6 m, maximum spalling ratio was 49.15 % and maximum spalling length was 50.75 %.

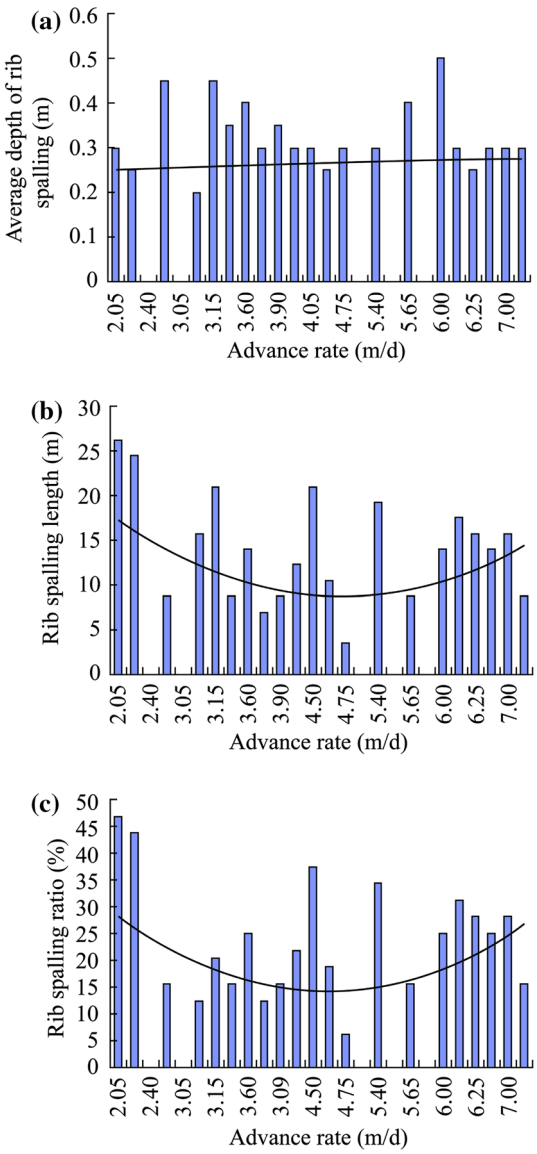


**Fig. 27** Relationship *curves* between coal wall spalling and face advance speed at the lower part of the face (non-periodical ground pressure). **a** Relationship between average rib spalling depth and face advance rate, **b** relationship between rib spalling length and face advance rate, **c** relationship between rib spalling ratio and face advance rate

(3) Coal wall spalling at the lower part of the face. Observation results of coal wall spalling at the lower part of the face (during the periodical ground pressure period) are shown in Table 15 and Fig. 32. During the period of periodical ground pressure, the average coal wall spalling depth at the lower part of the face decreased with the increase of the face advance speed. Before the face advance speed

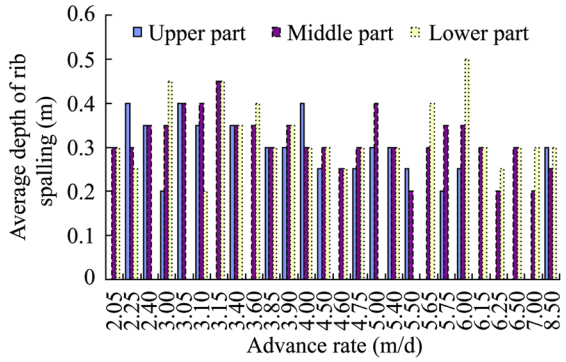


**Fig. 28** Comparison of average spalling depth at different face positions (non-periodical ground pressure period)

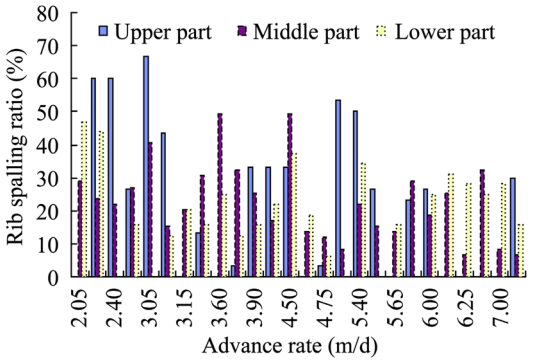


**Fig. 29** Comparison of average spalling ratio at different face positions (non-periodical ground pressure period)

**Table 11** Statistical analysis results of spalling depth at the upper, middle and lower parts of the face (non-periodical ground pressure period)

| Face advance speed (m/d) | Average spalling depth (upper) (m) | Average spalling depth (middle) (m) | Average spalling depth (lower) (m) | Average spalling depth (m) |
|---|---|---|---|---|
| 2.05 | 0 | 0.30 | 0.30 | 0.20 |
| 2.25 | 0.40 | 0.30 | 0.25 | 0.32 |
| 2.40 | 0.35 | 0.35 | 0 | 0.23 |
| 3.00 | 0.20 | 0.35 | 0.45 | 0.33 |
| 3.05 | 0.40 | 0.40 | 0 | 0.27 |
| 3.10 | 0.35 | 0.40 | 0.20 | 0.32 |
| 3.15 | 0 | 0.45 | 0.45 | 0.30 |
| 3.40 | 0.35 | 0.35 | 0.35 | 0.35 |
| 3.60 | 0 | 0.35 | 0.40 | 0.25 |
| 3.85 | 0.30 | 0.30 | 0.30 | 0.30 |
| 3.90 | 0.30 | 0.35 | 0.35 | 0.33 |
| 4.00 | 0.40 | 0.30 | 0.30 | 0.33 |
| 4.50 | 0.25 | 0.30 | 0.30 | 0.28 |
| 4.60 | 0 | 0.25 | 0.25 | 0.17 |
| 4.75 | 0.25 | 0.30 | 0.30 | 0.28 |
| 5.00 | 0.30 | 0.40 | 0 | 0.23 |
| 5.40 | 0.30 | 0.30 | 0.30 | 0.30 |
| 5.50 | 0.25 | 0.20 | 0 | 0.15 |
| 5.65 | 0 | 0.30 | 0.40 | 0.23 |
| 5.75 | 0.20 | 0.35 | 0 | 0.18 |
| 6.00 | 0.25 | 0.35 | 0.50 | 0.37 |
| 6.15 | 0 | 0.30 | 0.30 | 0.20 |
| 6.25 | 0 | 0.20 | 0.25 | 0.15 |
| 6.50 | 0 | 0.30 | 0.30 | 0.20 |
| 7.00 | 0 | 0.20 | 0.30 | 0.17 |
| 8.50 | 0.30 | 0.25 | 0.30 | 0.28 |
| Average | 0.20 | 0.32 | 0.26 | 0.26 |

reached 4.5 m/d, there was no distinct decrease of spalling depth, and the slope of the trend line was almost zero. When the face advance speed exceeded 4.5 m/d, there was a distinct decrease of spalling depth, thus the slope of the trend line increased.

As shown in Fig. 32b, c, during the periodical ground pressure period, the coal wall spalling ratio at the lower part of the face demonstrated a trend of increase early on, and decreasing later with the increase of face advance speed.

(4) Comparison of coal wall spalling at different face positions during the periodical ground pressure

As shown in Table 16, during the period of periodical ground pressure, the spalling depths at different face positions were almost identical, the average spalling depth was maintained at 0.29 m. The maximum spalling depth reached 0.7 m and the spalling depth exceeded 0.5 m, accounting for 30 %. During the period of periodical ground pressure, the spalling depth showed randomness, however, in general, presented a trend to decrease with the increase of face advance speed.

As shown in Table 17, during the occurrence of periodical ground pressure, the spalling ratio at the upper part of the face was the largest, reaching 38.67 %, less in the middle part at 28.81 %, and least at the lower part, 20.1 %. The average spalling ratio was 29.16 %.

### *3.6.5 Comparison of coal wall spalling at different ground pressure periods*

Figures 33 and 34 show spalling depth and spalling ratio at different ground pressure periods respectively (average 4.9 m/d).

As shown in Fig. 33, the average difference of spalling depth with periodical ground pressure was 0.05 m (under the same face advance speed, the difference of spalling depth with periodical ground pressure or without periodical ground pressure).

**Table 12** Statistical analysis results of spalling ratio at the upper, middle and lower parts of the face 8108 (non-periodical ground pressure period)

| Face advance speed (m/d) | Average spalling ratio (upper) (%) | Average spalling ratio (middle) (%) | Average spalling ratio (lower) (%) | Spalling ratio (%) |
|---|---|---|---|---|
| 2.05 | 0 | 28.81 | 46.88 | 27.05 |
| 2.25 | 60.00 | 23.73 | 43.75 | 38.89 |
| 2.40 | 60.00 | 22.03 | 0 | 26.21 |
| 3.00 | 26.67 | 27.12 | 15.63 | 24.52 |
| 3.05 | 66.67 | 40.68 | 0 | 37.20 |
| 3.10 | 43.33 | 15.25 | 12.50 | 26.21 |
| 3.15 | 0 | 20.34 | 20.34 | 20.29 |
| 3.40 | 13.33 | 30.51 | 15.63 | 22.83 |
| 3.60 | 0 | 49.15 | 25.00 | 31.28 |
| 3.85 | 3.33 | 32.20 | 12.50 | 20.29 |
| 3.90 | 33.33 | 25.42 | 15.63 | 25.36 |
| 4.00 | 33.33 | 16.95 | 21.88 | 22.83 |
| 4.50 | 33.33 | 49.15 | 37.50 | 43.12 |
| 4.60 | 0 | 13.56 | 18.75 | 11.84 |
| 4.75 | 3.33 | 11.86 | 6.25 | 8.45 |
| 5.00 | 53.33 | 8.47 | 0 | 17.75 |
| 5.40 | 50.00 | 22.00 | 34.00 | 32.97 |
| 5.50 | 26.67 | 15.25 | 0 | 14.37 |
| 5.65 | 0 | 13.56 | 15.63 | 10.99 |
| 5.75 | 23.33 | 28.81 | 0 | 20.29 |
| 6.00 | 26.67 | 18.64 | 25.00 | 22.83 |
| 6.15 | 0 | 25.42 | 31.25 | 21.14 |
| 6.25 | 0 | 6.78 | 28.13 | 10.99 |
| 6.50 | 0 | 32.20 | 25.00 | 22.83 |
| 7.00 | 0 | 8.47 | 28.13 | 11.84 |
| 8.50 | 30.00 | 7.00 | 16.00 | 15.22 |
| Average | 22.56 | 22.81 | 19.05 | 22.60 |

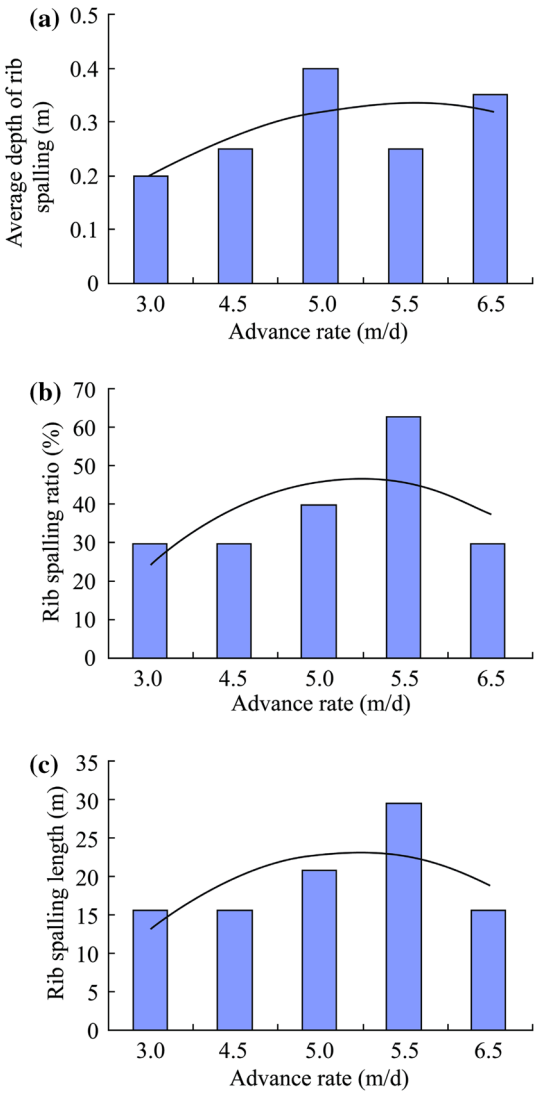


**Fig. 30** Relationship curves between coal wall spalling and face advance speed at the upper part of the face (periodical ground pressure period). **a** Relationship between average rib spalling depth and face advance rate, **b** relationship between rib spalling ratio and face advance rate, **c** relationship between rib spalling length and face advance rate

As shown in Fig. 34, the periodical ground pressure has limited influence upon the coal wall spalling ratio at the No. 8105 face. The difference of spalling ratio caused by the ground pressures was 4.64 % (at the same face advance speed, the difference between the spalling ratio during periodical ground pressure period and the spalling ratio during the non-periodical ground pressure period).

**Table 13** Characteristics of coal wall spalling at the upper part of No. 8105 face during periodical ground pressure period

| Face advance speed (m/d) | Average spalling depth (m) | Spalling length (m) | Spalling ratio (%) | Maximum spalling depth (m) |
|---|---|---|---|---|
| 3.00 | 0.20 | 15.75 | 30.00 | 0.30 |
| 4.50 | 0.25 | 15.75 | 30.00 | 0.50 |
| 5.00 | 0.40 | 21.00 | 40.00 | 0.50 |
| 5.50 | 0.25 | 29.75 | 63.33 | 0.30 |
| 6.50 | 0.35 | 15.75 | 30.00 | 0.50 |

**Table 14** Characteristics of coal wall spalling in the middle part of No. 8105 face during periodical ground pressure period

| Face advance speed (m/d) | Average spalling depth (m) | Spalling length (m) | Spalling ratio (%) | Maximum spalling depth (m) |
|---|---|---|---|---|
| 3.00 | 0.40 | 29.75 | 28.81 | 0.60 |
| 4.50 | 0.25 | 50.75 | 49.15 | 0.30 |
| 5.00 | 0.30 | 19.25 | 18.64 | 0.30 |
| 5.50 | 0.20 | 19.25 | 18.64 | 0.20 |
| 6.50 | 0.30 | 29.75 | 28.81 | 0.40 |

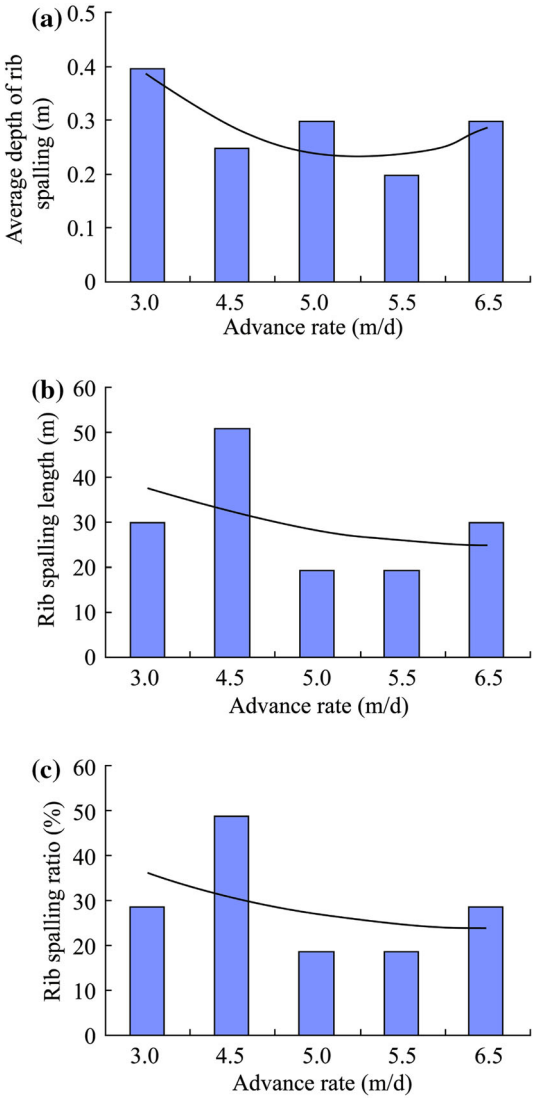


**Fig. 31** Relationship curves between coal wall spalling and face advance speed in the middle part of the face (periodical ground pressure period). **a** Relationship between average rib spalling depth and face advance rate, **b** relationship between rib spalling length and face advance rate, **c** relationship between rib spalling ratio and face advance rate

### *3.6.6 Conclusion of the observation on coal wall at No. 8105 LLTCC face*

(1) During the non-periodical ground pressure period, the relationship between the coal wall spalling ratio and face advance speed presented randomness. However, in general, the spalling ratio reduced with the increase of face advance speed. There were some differences in the spalling ratio at different face positions. The statistical analysis of the spalling ratio showed: the spalling ratio in the middle part of the face > the spalling ratio at the upper part of the face > the spalling ratio at the lower part of the face.

(2) During the periodical ground pressure period, the spalling depth and ratio showed a decreasing trend with the increase of the face advance speed. The spalling depth showed a difference at different face positions, i.e., upper part > middle part > lower part.

(3) During the period of periodical ground pressure occurrence, the spalling ratio showed a trend of increase early and decreased later on with the increase of the face advance speed. The spalling ratios at different face positions were different.

Through the comparison of coal wall spalling with the neighbouring No. 8104 face, it was found that: during the period of non-periodical ground pressure occurring, the average coal wall spalling ratio was 33.08 % and the spalling depth varied from 0.2 to 0.3 m at the No. 8104 face; the average spalling ratio was 22.06 % and the spalling depth varied from 0.18 to 0.25 m at the No. 8105 face. During the period of periodical ground pressure, the spalling ratio was 36.18 % at the No. 8104 face, and 29.16 % at the No. 8105 face. Based on the statistical analysis, the spalling depth and length were the largest in the middle parts of the No. 8104 and No. 8105 faces. In comparison with the No. 8104 face, the spalling ratio at the No. 8105 face was 33.4 % less than that at the No. 8104

**Table 15** Characteristics of coal wall spalling at the lower part of No. 8105 face during periodical ground pressure period

| Face advance speed (m/d) | Average spalling depth (m) | Spalling length (m) | Spalling ratio (%) | Maximum spalling depth (m) |
|---|---|---|---|---|
| 3.00 | 0.45 | 7.00 | 12.50 | 0.70 |
| 4.50 | 0.30 | 21.00 | 37.50 | 0.40 |
| 5.00 | 0.40 | 21.00 | 37.50 | 0.50 |
| 5.50 | 0.25 | 7.00 | 12.50 | 0.30 |
| 6.50 | 0 | 0 | 0 | 0 |

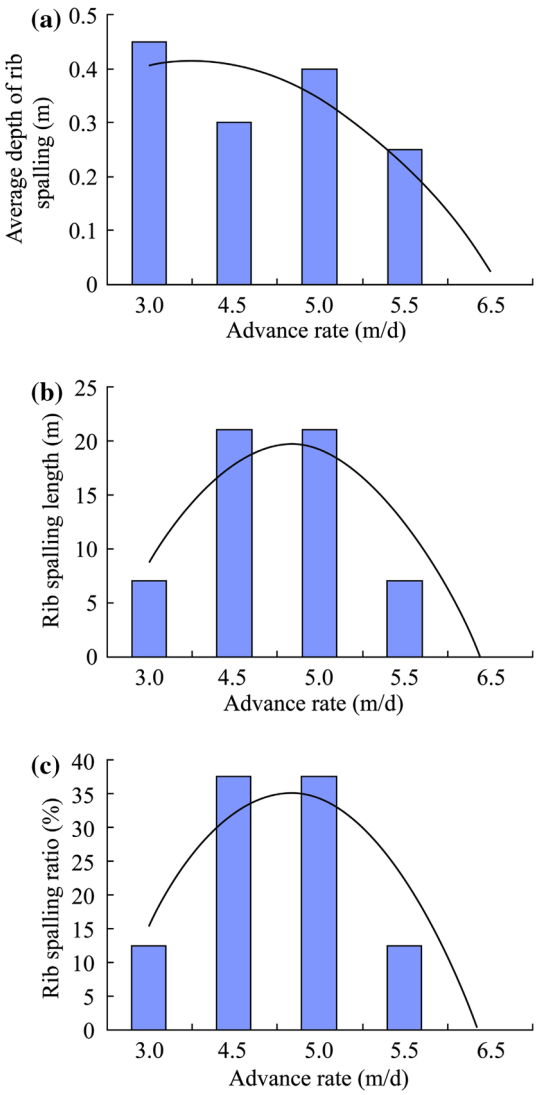


**Fig. 32** Relationship *curves* between coal wall spalling and face advance speed at the lower part of the face (periodical ground pressure period). **a** Relationship between average rib spalling depth and face advance rate, **b** relationship between rib spalling length and face advance rate, **c** relationship between rib spalling ratio and face advance rate

face, and the spalling depth was also 50 mm less than that at the No. 8104 face. Therefore, it can be concluded that the coal wall spalling was significantly reduced and the face achieved a fast advance speed due to the application of proposed comprehensive control technology at the No. 8105 face in Tashan coal mine in Datong, China, including controlling face advance speed, increasing support initial abutment force and increasing the wall protection capacity of support.

### 3.7 High efficient top-coal caving technology at a LLTCC operation

#### *3.7.1 Study on rational top-coal drawing interval*

It is important to select a rational top-coal drawing interval to improve coal recovery and reduce the percentage of gangue. If the drawing interval is too large, the top coals might be caved into the goaf, resulting in a coal loss. On the other hand, if the drawing interval is too small, the gangue might be mixed with coals and cave into the discharge window, which may not only affect the coal quality, but also be mistaken for top coal exhaustion and result in coal loss. The factors for determining the drawing interval consists of the thickness of the top coal, the discharge window length of support, the center height of the discharge window and the shearer's cutting depth. The principal for determining the drawing interval is to fracture and loosen the top coal in the range of the discharged coal, increase top coal recovery and reduce the percentage of gangue. In addition, the rational drawing interval should match the coal mining process and form an integer-times relationship with the shearer's cutting depth.

The drawing interval must be greater than the length of discharge window to avoid mixing the gangue with coal. The small drawing interval might result in the gangue in the goaf being mixed with caved top coals. The large drawing interval might result in top coal losses. A rational drawing interval will maintain the mixture of top coal with

**Table 16** Statistical analysis results of spalling depth at the upper, middle and lower parts of No. 8105 face (during periodical ground pressure period)

| Face advance speed (m/d) | Average spalling depth (upper) (m) | Average spalling depth (middle) (m) | Average spalling depth (lower) (m) | Average (m) |
|---|---|---|---|---|
| 3.00 | 0.20 | 0.40 | 0.45 | 0.35 |
| 4.50 | 0.25 | 0.25 | 0.30 | 0.27 |
| 5.00 | 0.40 | 0.30 | 0.40 | 0.37 |
| 5.50 | 0.25 | 0.20 | 0.25 | 0.23 |
| 6.50 | 0.35 | 0.30 | 0 | 0.22 |
| Average | 0.29 | 0.29 | 0.28 | 0.29 |

**Table 17** Statistical analysis results of spalling ratio at the upper, middle and lower parts of No. 8105 face (during periodical ground pressure period)

| Face advance speed (m/d) | Spalling ratio (upper) (%) | Spalling ratio (middle) (%) | Spalling ratio (lower) (%) | Average (%) |
|---|---|---|---|---|
| 3.00 | 30.00 | 28.81 | 12.50 | 23.77 |
| 4.50 | 30.00 | 49.15 | 37.50 | 38.88 |
| 5.00 | 40.00 | 18.64 | 37.50 | 32.05 |
| 5.50 | 63.33 | 18.64 | 12.50 | 31.49 |
| 6.50 | 30.00 | 28.81 | 0 | 19.60 |
| Average | 38.67 | 28.81 | 20.00 | 29.16 |

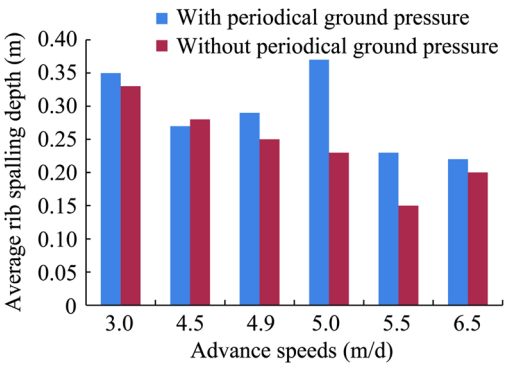


**Fig. 33** Comparison of average spalling depth at different ground pressure periods under different face advance speeds

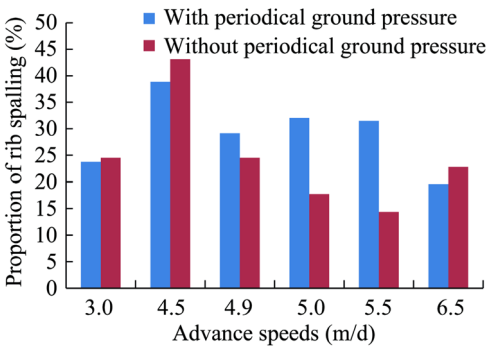


**Fig. 34** Comparison of spalling ratio at different ground pressure periods under different face advance speeds

gangue and top coal losses in allowable limits. In a LLTCC face, the space for top coal fracturing becomes larger due to the increase in mining height, therefore, the effects of ground pressure on top coal fracture become greater. With the effects of ground pressure, the top coal will be fractured and broken thoroughly. The top coal fragment becomes smaller and has a better flowability.

The drawing interval has a significant influence on the coal and gangue flow and thus is a key parameter for the LLTCC process. Figure 35 shows the coal and gangue flow at different drawing intervals. The boundary of coal and gangue before and after top coal discharge is regarded as the starting line for starting coal discharge and the finishing line for finishing coal discharge. In the experimental test, three drawing intervals were tested including one cutting and one coal caving, two cuttings and one coal caving, and three cuttings and one coal caving. In the process of support shift and coal caving, the boundary of coal and gangue was moved forward and maintained in the same shape. With the increase of the drawing interval, the distance between the starting line and the finishing line also increased.

As shown in Fig. 35, with the increase in the top coal drawing interval, there were some variations in the boundary shape of coal and gangue before and after top coal caving. In other words, the initial caving point of top coal shifted forward, the distance between start line and finish line of top coal caving increased with the drawing

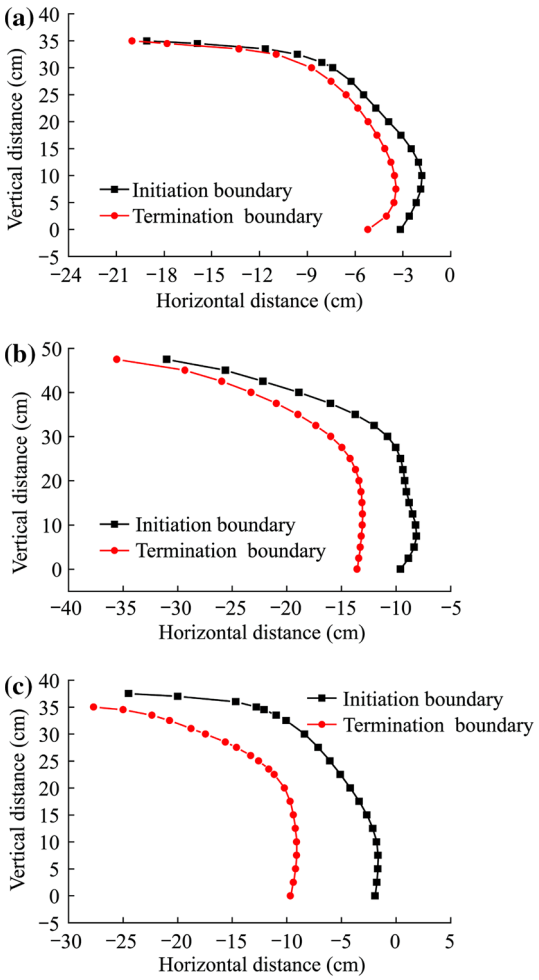


**Fig. 35** Boundaries between coal and gangue with different top coal drawing intervals. **a** One cutting and one drawing, **b** two cuttings and one drawing, **c** three cuttings and one drawing

interval. This indicated that the amount of coal discharged at each discharge circle increased with the increase of the drawing interval.

There were three kinds of coal and gangue mixtures near the discharge window of support after top coal caving using different drawing intervals:

(1) When the drawing interval is small, the gangue in the direction of the goaf reaches the discharge window earlier than the top coals do, and the discharged coals mix with gangue. Before coal discharge, the boundary between coal and gangue near the discharge window is beyond the lower boundary of the tail beam. Therefore, it results in the part of middle to top coals being unable to be discharged due to the enclosure of gangue and the tail beam. In this case, the gauge might enter the discharge window from the bottom of the window, and increase the percentage of gangue in the coals obtained.

(2) With a rational top-coal drawing interval, at initial coal discharge, the gangue in the goaf and top coal will reach the discharge window of the support at the same time. Before the coal discharge, the boundary between coal and gangue is behind the lower boundary of the tail beam, thus the horizontal movement of gangue in the goaf is small. In the process of top-coal caving and discharge, the coals can smoothly reach the discharge window. With the caving of the lower and middle part of the coals, the gangue above the coal seam caves as well, then there will be some mixture of coal and gangue during the discharge of the upper layer of top coal. The mixture gangue is mainly from the roof above the seam that enters the discharge window with the discharge of top coals.

(3) When the drawing interval is too large, at the beginning of coal discharge, top coals caved reach the discharge window earlier than gangue in the goaf. Before coal discharge, the boundary between coal and gangue is obviously behind the lower boundary of the tail beam, and the gangue in the goaf cannot reach the discharge window. With a LLTCC operation, the angle of the shield beam becomes larger, and the height of the discharge window becomes higher. During the process of coal discharge, the top coal above the discharge window can be discharged quickly and the gangue above the top coal also caves quickly. In this case, the coal and gangue in the goaf near the discharge window with natural angle of depose cannot flow toward the discharge window and be discharged, resulting in coal losses and low coal recovery.

Figure 36 shows the shape of residual top coals with different drawing intervals. As shown in the figures, the one cutting and one drawing method (drawing interval is 0.8 m) can lead to a high top coal recovery.

### *3.7.2 Study on rational coal discharge method*

Top coal discharge method involves the combination of sequence of coal discharge, the times of coal discharge at each discharge window and the quantity of coal discharge, as well as the number of discharge window opened in the same time along the face. The sequence of coal discharge can be categorized as sequential coal discharge and alternated coal discharge. The times of coal discharge at each discharge window can be categorized as single, double and multiple coal discharges. The number of coal discharge window opened in the same time can be categorized as

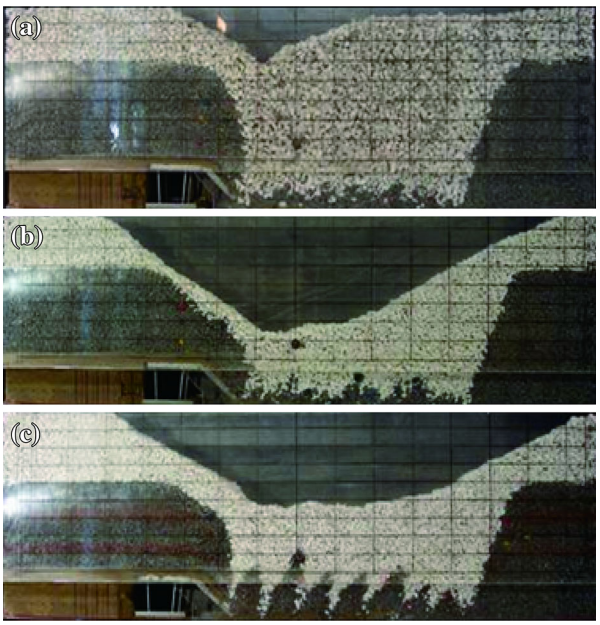


**Fig. 36** Shape of residual top coals with different drawing intervals. **a** One cutting and one drawing (drawing interval 0.8 m), **b** two cuttings and one drawing (drawing interval 1.6 m), **c** three cuttings and one drawing (drawing interval 2.4 m)

single window discharge and multiple window discharge. The number of simultaneously opened discharge window can be categorized as single coal discharge and multiple coal discharge. The quantity of coal discharge can be categorized as equal quantity and non-equal quantity. Because it is difficult to manage equal or non-equal quantity coal discharge in operation, and single or multiple coal discharge can be managed in labor planning, however the determination of the coal discharge method is mainly based on the sequence of coal discharge and the times of coal discharge at each discharge window. There are four main alternative methods including single sequential coal discharge, single alternated coal discharge, multi-round sequential coal discharge and multi-round alternated coal discharge. The geological conditions for different coal seams are different, and their capabilities are also different, thus, different coal discharge methods must be used, and the recovery of top coal is also varied.

A numerical analysis was conducted to simulate the top-coal caving and discharge by using the geological parameters of coal seams and the technical parameters of hydraulic supports at Tashan coal mine. In addition, the simulated loose thickness of the top coal was 10.50–11.17 m, and the simulated cutting heights were 4, 4.5 and 5 m. The top-coal caving and discharge operation was simulated including single sequential coal discharge, single alternated coal discharge and multiple alternated coal discharge method. The numerical results showed that the recovery of coal cutted and discharged was the lowest using single-time alternated multiple windows coal discharge, and highest using discharge in multi-round & multiple windows sequence alternately. In order to increase the recovery of top coal, the method of multiple-time alternated multiple window coal discharge was selected in the LLTCC operation at the No. 8105 face, Tashan coal mine in Datong, China.

## 4 Key equipment for the LLTCC coal mining operation

Key equipment for the LLTCC coal mining operation involves hydraulic support, shearer, front scraper conveyor, rear scraper conveyor, headgate belt conveyor and support hauler, etc. Prior to this project, there was no equipment for LLTCC coal mining operations in China or elsewhere in the world. Therefore, the various key equipment for LLTCC mining operation have been developed in this project.

### 4.1 Hydraulic support with large mining heights

Hydraulic support is one of key equipment for a LLTCC coal mining operation. The requirements for hydraulic support consist of rational structure, sufficient support resistance force, stable and shock resistance, sustainability of high efficient coal discharge and high coal recovery.

#### *4.1.1 Support and rock coupling 3D dynamic optimization design method*

In the design of hydraulic support, a support and rock coupling 3D dynamic optimization design method was used. The effects of surrounding rock on support structure, support intensity, and shift capability were fully considered. As the support and rock coupling based 3D dynamic parameter design commenced from roof movement, a simulation was conducted to simulate the transfer of fracture, subsidence, crash and the caving of roof into the pressure, torque, deformation and shift speed of the support. Using a series of conditions, support working resistance, support type and control parameters were dynamically determined to satisfy the requirements of roof movement and effective support on the roof. With the consideration of coal wall and floor characteristics, the forms and parameters of the auxiliary components for coal wall protection and bottom lift were determined. The advantages of the proposed method can be stated as: the dynamic characteristics of surrounding rock were fully considered through the dynamic interaction between

supports and surrounding rock, the variation of roof subsidence and fracture was transferred to the support in the forms of pressure, torque and constraints. Hydraulic support responded in terms of forms and characteristic parameters, and the response results fed back to rock in the forms of support resistance force and torque. Therefore, the roof caving and the distribution of stress and strain could be controlled.

In terms of the technique for the support design, a 3D parametric dynamic design method from top to bottom was used. In the design process, the requirements of support from surrounding rock were gradually satisfied. The flowchart of support design is shown in Fig. 37. The method proposed achieves seamless integration between the optimization of structural parameters and the 3D modelling. Furthermore, the method improves the design efficiency, provides an integrated platform for structure optimization and parametric design, and improves the applicability of support.

#### *4.1.2 Determination of support technical parameters*

Based on the geological conditions at the No. 8105 coalface in Tashan coalmine, the composition of support working resistances during their calculation was analyzed. Using the numerical modelling method, the numerical model was built based on the occurrence conditions of coal seams. Subsequently, the model was used to simulate the support intensity of 0, 0.5, 0.9, 1.2, 1.3, 1.4, 1.5, and 1.6 MPa, respectively. The analysis on the vertical stress at the coalface showed that the increase of support intensity could not change the distribution of abutment stress in the front of the coalface. The front peak abutment stress was approximately 10 m from the coal wall. With the increase of support intensity, the area of peak abutment stress in the front of the coal face decreased and became closer to the coal wall.

In order to obtain the relationship curve between support intensity and roof subsidence ($P$–$\triangle L$ curve) within the roof control range, the subsidence of the roof at a position 3 m

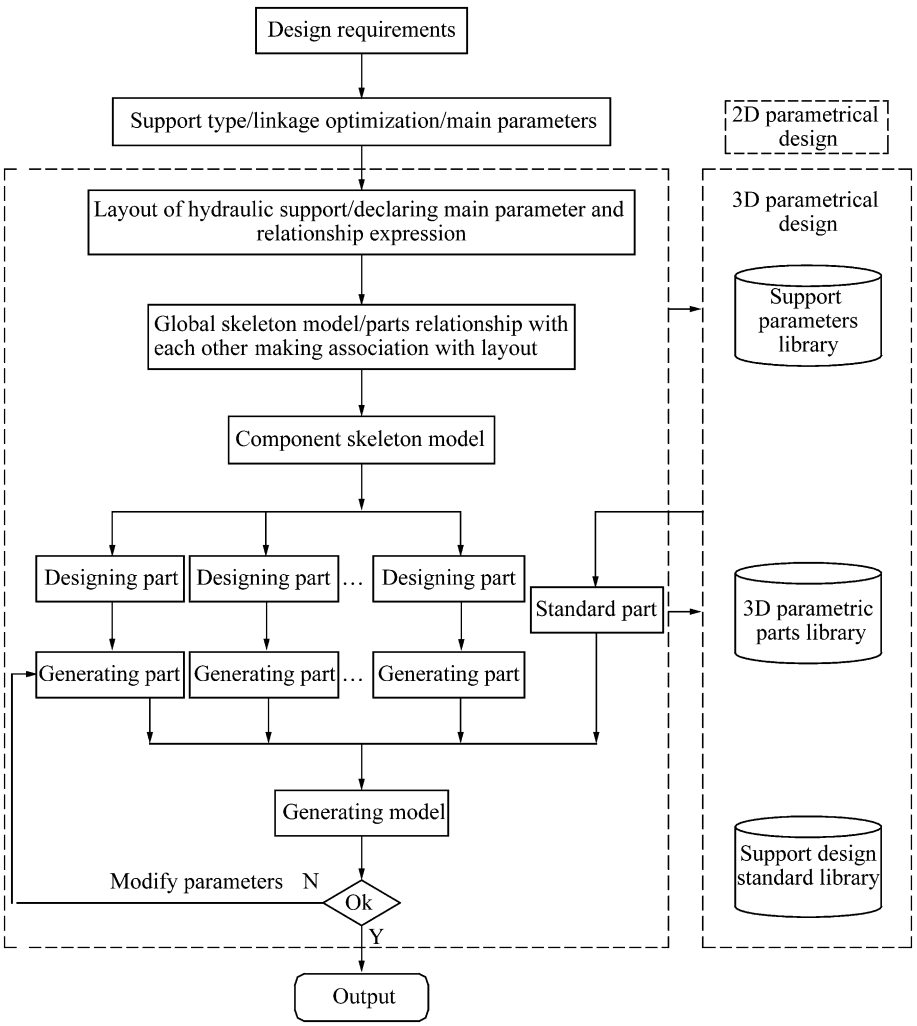


**Fig. 37** Flowchart of 3D parametric dynamic design of the hydraulic support from top to bottom

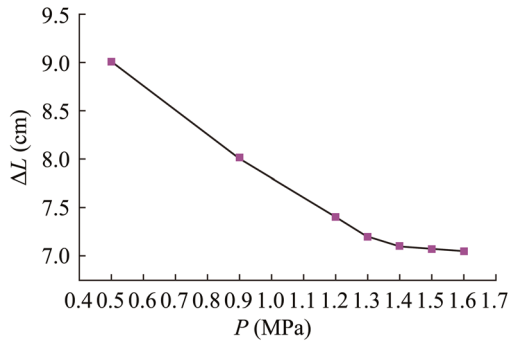


**Fig. 38** Relationship curve between support intensity and roof subsidence ($P$–$\triangle L$ curve)

away from the coal wall were measured, and simulated with the support intensity of 0.5, 0.9, 1.2, 1.3, 1.4, 1.5 and 1.6 MPa. The curve between support intensity and roof subsidence is shown in Fig. 38.

As shown in the relationship curve between support intensity $P$ and roof subsidence $\triangle L$, the subsidence of the roof gradually decreases with the increase of support intensity. When the increase of support intensity reaches a certain level, the increase of support intensity have little effect on the roof subsidence. Nevertheless, if the support intensity is below a given level, the reduction of support intensity will have substantial impact on roof subsidence. The given level of support intensity can be selected as rational support intensity. When the support intensity reaches 1.4–1.5 MPa, the decrease of roof subsidence will not obvious with the increase of support intensity. As a result, the rational support intensity is determined as 1.4–1.5 MPa. With comprehensive analysis on the mining and face conditions, the support intensity of the hydraulic support was determined as 1.4 MPa in Tashan coal mine.

Determination of support resistance.

Nominal working resistance $F$ can be calculated as Eq. (13):

$$F \geq \frac{PB_cL}{\eta} \tag{13}$$

where $P$ is the nominal support intensity at the LLTCC face, 1.4 MPa; $L$ is the center distance, 1.75 m; $B_c$ is the roof control distance, 5.5 m; $\eta$ is the support efficiency, 0.98.

Substitute the parameters above into Eq. (13), get:

$$F \geq \frac{1.4 \times 5.5 \times 1.75}{0.98} = 13750 \text{ kN}$$

Considering the safety coefficient, the nominal support resistance was determined as 15000 kN, which is consistent with the calculation result from the "cantilever beam-articulated beam" structural mechanical model.

The support and rock coupling mechanical model (Wang 2009) was used to analyses the main technical parameters of hydraulic support at Tashan coal mine. The support parameters were optimized based on the support and rock coupling mechanical model. The structural parameters, i.e. the beam length of the support, the center distance of the support, and maximum and minimum heights, were used as optimizing variables, and the surrounding distribution of roof stress and the floor pressure of the support front were used as the optimizing objective. The optimizing expression was:

Objective functions:

$$\begin{cases} \Delta p = \left| p - p_j \right| \leq \lambda (j = 1, 2, \ldots n) \\ \min \delta \end{cases} \tag{14}$$

where $p_j = f\,(l,h_{\max},h_{\min},a,b)$, $\delta = k\,(l,h_{\max},h_{\min},a,b)$; $\triangle p$ is the absolute difference between support intensity $p_j$ calculated iteratively based on support parameters and the result calculated based on surrounding rock parameters. When $\triangle p$ is less than or equal to a given condition of convergence $\lambda$, the support intensity is regarded as rational. The optimizing objective of floor pressure at the support front is to minimize the floor pressure. Function $f$ and $k$ are the mechanical status expression of the surrounding rock affected by support parameters obtained from the analysis of the interaction of support and surrounding rock, respectively. In the objective function, $l$ is the length of top beam, $h_{\max}$ and $h_{\min}$ are maximum support height and minimum support height; $a$ is the support center distance, being selected as 1.5, 1.75 and 2.05 m, $b$ is the horizontal distance between the center of the top beam prop cup and the center of the base prop foot.

Before optimization, the support type should be selected. The parameters of support are used as the variables of optimization function, after which the multiple-objective optimization function is established. After the calculation results converge to a group of stable values, the rational optimization results are obtained. In the Tashan coal mine, during the process of the LLTCC mining operation in 14–20 m thick coal seams, the thickness of the top coal is large and the caving space is also large, therefore, the movement of roof increases, and the range of resultant force point of interaction between support and roof becomes large (Yu et al. 2012). According to the observation results of ground pressure at the No. 8104 LLTCC face in Tashan coal mine, the resistance alternately increased at the rear prop or front prop during the roof periodical ground pressure period. As a consequence, the positive four-link bar type of support was selected to better suit the ground pressure.

The average seam thickness at the No. 8105 face in Tashan coal mine is approximately 20 m. Based on the requirement of not exceeding the cutting to caving ratio 1:3, the cutting height reached 5 m. Based on the requirements of cutting height and the parameter optimization of support-rock coupling, the main technical parameters of support were determined as follows: the maximum support height is 5200 mm, the minimum

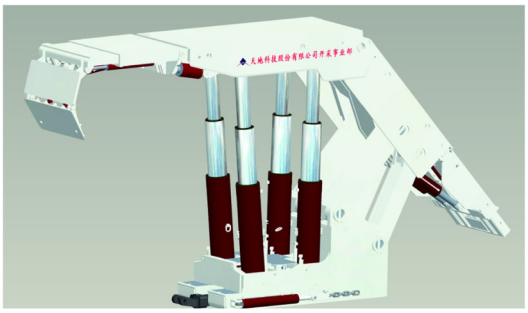

**Fig. 39** LLTCC hydraulic support with a height of 5.2 m

support height is 2800 mm, the top beam length is 5615 mm, the support center distance is 1750 mm, the horizontal distance between top beam prop cup center and support prop base center is 402 mm, and the support working resistance is 15,000 kN. Figure 39 shows the LLTCC hydraulic support as developed.

#### *4.1.3 Development of shock resistance components for LLTCC hydraulic support*

In comparison to the fully mechanized longwall mining method and the fully mechanized LTCC mining method, the LLTCC mining method requires a higher standard for the shock resistance of hydraulic support. Thus, a large diameter double telescopic shock resistance prop was developed. Its main parameters are as follows: outer cylinder: cylinder diameter $\phi$360 mm, cylinder outer diameter $\phi$418 mm; middle cylinder: cylinder diameter $\phi$ 260 mm, cylinder outer diameter $\phi$340 mm; small cylinder: cylinder diameter $\phi$235 mm, cylinder outer diameter $\phi$145 mm; working resistance ($P_1/P_2$ = 43.2/82.3 MPa): 4400 kN.

A 1000 $\text{min}^{-1}$ large flow rate safety valve fast release device was developed to meet the requirement of a safety valve with a flow rate of 620 $\text{min}^{-1}$ when prop was under shock force. With the development of key components above, the shock resistance capacity of the hydraulic support increased approximately 10 %.

#### *4.1.4 High efficient coal discharge device for a LLTCC hydraulic support*

At a LLTCC coal mining face in a coal seam with thickness greater than 10 m, the caving height is high after the top coals cave, and the size of coal block is relatively large. Therefore, the top coals might form an "arch" balance structure during top coal caving. To break the "arch" balance structure and enable the top coals to be easily discharged into the rear scraper conveyor is a key technology. Therefore, the technical issues discussed above must be solved for LLTCC hydraulic support, which provides the top coal control technology for a LLTCC hydraulic support.

As a result, the following method can be used for the LLTCC hydraulic support:

(1) The control of the size of the coal discharge window: The control of the discharge window is to control the coal discharge quantity at a single discharge window. Under the same flowability of caved top coals, the discharged quantity in a unit time is in proportion with the size of the discharge window. As a result, the centerline spacing of supports was modified from 1.5 m to 1.75 m to increase the size of discharge window along the inclined direction of the face (size in transverse direction). Simultaneously, the size of the discharge window in the longitudinal direction (along the strike direction of the face) was controlled.

The size of the coal discharge window is controlled by a coal discharge device (coal discharge sliding plate and tail beam). The size of the discharge window is the function of the extension length of the sliding plate and the swing angle of the tail beam. When the coal discharge window is completely opened, the maximum size of the discharge window in the longitudinal direction is equal to the coal-reception width of the rear scraper conveyor. In this case, the coal discharge rate of single support is determined by the chain speed of the rear scraper conveyor and the blockage coefficient of coal flow. The coal discharge rate of single support can be calculated using Eq. (15).

$$V_f = 60\,K_f F \gamma V_s \tag{15}$$

where $V_f$ is the coal discharge rate of single support, t/min; $K_f$ is the blockage coefficient of discharged coal flow, $K_f = 0.6$; $F$ is the carrying cross-section of the rear scraper conveyor, $m^2$; $\gamma$ is the loose coal density, $t/m^3$; $V_s$ is the chain speed of scraper conveyor, m/s.

(2) The time of multiple coal discharge and the control of coal discharge quantity: In respect of the LLTCC mining operation at Tashan coal mine, because the ply of the top coal is very thick and the top coal is very hard, after top coal caving, the upper top coals cannot fully break due to limited caving space. Some of top coals close to the roof cannot even cave. In this case, if the caved coals are discharged completely, there will be losses of large coal blocks and uncaved top coals. As a result, there should be multiple coal discharges, e.g., two or three times. The multiple coal discharges will provide time and

space for the fracturing and caving of top coals, and enable the boundary of caved top coals and immediate roof gangue to be evenly subsided.

The purpose of multiple coal discharges is to provide time and space for the top coals and the immediate roof to fracture and cave. Therefore, the delay time of the second coal discharge cannot be too short. Generally, the second coal discharge should be more than 10 m away from the first coal discharge. It should be adjusted according to the movement of top coals and the roof.

The discharged coal quantity in a round is determined by the awaited discharge of top coals. The awaited discharge quantity of top coals can be calculated theoretically, as shown in Eq. (16).

$$Q_{\mathrm{d}} = h_2 B S \gamma \eta_{\mathrm{d}} \tag{16}$$

where $Q_{\mathrm{d}}$ is the awaited discharged quantity of top coals in a support, t; $h_2$ is the thickness of top coals, m; $B$ is the width of support, m; $S$ is the discharge interval, m; $\eta_{\mathrm{d}}$ is the recovery of top coals, %.

Because the discharged coal quantity in a unit of time at a discharge window cannot be calculated, the control of discharged coal quantity each time at a support is to control the time. After the start of a LLTCC operation, the coal discharge time at a discharge window should be calculated through several rounds of coal discharge operation. The time from the start of discharge until the gangue occurring in the discharge flow is the time of coal discharge in a round. When using two rounds of coal discharge, the time spent on one round of coal discharge should be half of the total coal discharge time, and 1/3 of the total coal discharge time for three rounds of coal discharge.

(3) During the process of coal discharge, the size of caved coal is suitable at the initial stage and the discharged coal flow is smooth. With the discharge of top coals, the large-size coals increase and form a balanced arch above the discharge window to block the coal flow. In this case, the base of the balanced arch should be broken using a coal discharge device. In addition, the large coal blocks should be crushed to enable the continuity of coal discharge. Therefore, the tail beam should be continuously swung up and down during the process of coal discharge to disturb the awaited top coals. The upswing of the tail beam can crush large coal blocks and the down swing can loosen the coal flow.

Caving and discharging the top coals and increasing coal recovery is the major objective of the present project. Based on the studies on the caveability of top coals and the laws of top coal caving, the support structure and the method of top coal caving and discharge were optimized. A new highly efficient coal caving and discharge device was developed to increase top coal recovery. Figure 40 shows the design of the coal discharge device.

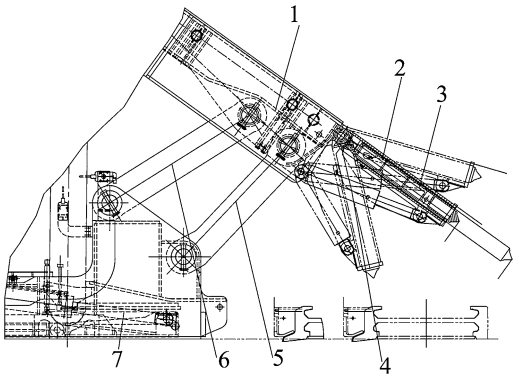


**Fig. 40** Coal discharge device. *1* shield beam, *2* tail beam-sliding plate, *3* pump of sliding plate, *4* pump of tail beam, *5* rear link bar, *6* front link bar, *7* base

Through the studies on previous coal discharge devices, the following problems were found:

(1) In previous type LTCC supports, the front link bar was the double link bar, and the rear link bar was the single link bar. The rear bar was fixed in the middle of the support base, which resulted in blocking the operator's sight and difficulty in observing the effects of top coal caving and discharge.

(2) There was no passage from the front to the rear of the support. Because the rear link bar was fixed in the middle of the support base, operators could not go through two supports from the front to the rear of the support. The only way was to go to the rear of the support via face ends, which resulted in difficulties in terms of safety and maintenance.

(3) The coal discharge device of the tail beam-sliding plate was easily jammed and hard to slide. Because the sliding plate was not slid back, the sliding plate occasionally cut the chain of the rear scraper conveyor when the tail beam swung.

In order to solve the above problems, a new type of coal discharge device was designed with a double rear link bar, middle passage and observation window for coal discharge through the optimization of support structure. In addition, the high efficient and high recovery coal discharge device had a strong disturbance capacity for releasing coals.

(1) A new type of coal discharge device with double front and rear link bars, middle passage and observation window.

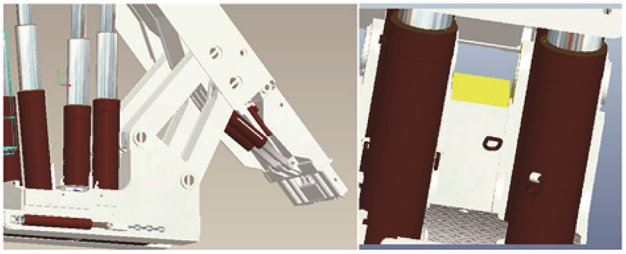

**Fig. 41** Middle passage in support

Through the optimization of the four-link bar on support, on the basis of meeting the requirements on support movement and limited positions, the internal components, i.e., shield beam and base, were re-designed. A new type of coal discharge device was developed with new double front and rear link bar, middle passage, and observation window, as shown in Fig. 41.

Under the ground pressure, the top coal is fractured and caved. The size of coal is different depending on the coal hardness. During the process of top coal discharge, the increase in large coals causes a balanced arch above the support discharge window and blocks the coal flow. In this case, the base of the balanced arch should be fractured using the coal discharge device. In addition, the large coal blocks should be crushed to enable the continuity of coal discharge. Therefore, a high efficient and high recovery coal discharge device was developed with a strong disturbance capacity. Two jacks with a cylinder diameter of $\phi$180 mm were installed on the tail beam for operation. The force of a single jack was 1000 kN ($P = 39$ MPa) and 2000 kN with both. In order to increase the disturbance to top coals, the upswing of the tail beam can reach 19.5° to crush top coals, and the down swing can reach 41° to loosen coal flow. During the process of top coal discharge, the tail beam was swung continuously to disturb the awaited top coals and to achieve a high efficient and high recovery coal discharge.

## 4.2 High efficiency and high reliability electrical haulage shearer

### *4.2.1 Assessment of the overall reliability of electrical haulage shearer*

The electrical haulage shearer is one of the key equipment in coal mining operations. High efficient continuous coal cutting is the shearer's main task, as the reliability and safety will affect coal production and operator safety. To meet the coal cutting requirements at the Tashan LLTCC coal mining operation, a new high efficiency, high reliability electrical haulage shearer had been developed. The shearer's specifications are as follows: cutting height 2.8–5.5 m, total installed power 1945 kW, coal cutting power 750 kW, maximum haulage speed 15–25 m/min, and maximum haulage power 2 × 570 kN, as shown in Fig. 42.

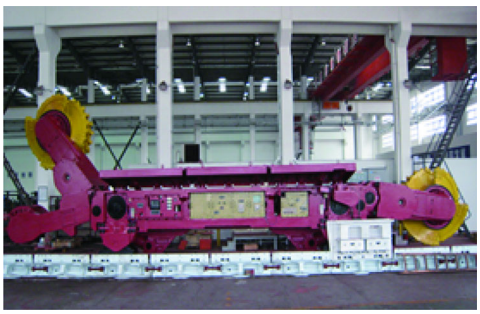

**Fig. 42** High efficiency and high reliability electrical haulage shearer

**Table 18** Common faults of electrical haulage shearer

| No. | Fault | No. | Fault |
|---|---|---|---|
| 1 | Not reach correct position | 20 | Structure crash |
| 2 | Broken | 21 | Jam |
| 3 | Loosen | 22 | False open |
| 4 | Fall off | 23 | False close |
| 5 | Bending | 24 | Unusual wear |
| 6 | Twisting | 25 | Oil leakage |
| 7 | No input | 26 | Inappropriate gap |
| 8 | No output | 27 | Puncture |
| 9 | Circuit open | 28 | Plastic deformation |
| 10 | Short circuit | 29 | Poor contact |
| 11 | Unable to switch | 30 | Blockage |
| 12 | Unable to start | 31 | Poor sealing |
| 13 | False action | 32 | Peel off |
| 14 | Flow blockage | 33 | Burn out |
| 15 | False indicator | 34 | Worn |
| 16 | Unexpected operation | 35 | False connection |
| 17 | External leakage | 36 | Burn down |
| 18 | Internal leakage | 37 | Fractured |
| 19 | False action | 38 | Rusty |

The reliability of the shearer is the key factor controlling normal mining operation. As a result, the assessment method for assessing shearer's reliability has been investigated. Table 18 lists 38 common faults of the electrical haulage shearer. A fault tree analysis method was used to analyses the reliability and design. Based on the theoretical analysis on component design, installation and the environment of usage, the main causes of component failure

were investigated to find the weakest link in reliability, and improve the reliability and utilization of the shearer.

The fault tree method for assessing the faults in electrical haulage shearer was divided into two stages:

(1) Establishment of fault tree for the electrical haulage shearer system.

① Collect and analyses the technical document of the electrical haulage shearer, including the drawings of the shearer, maintenance records, working environment and geological conditions, etc.
② Determine the contents and constraints of the electrical haulage shearer.
③ Determine top events based on the electrical haulage shearer system.
④ Analyze the causes and factors related with top events, the causes and factors related with each sub-system.
⑤ Map the fault tree of the electrical haulage shearer system. Deductively analyses from top events, search for causes level by level until reaching the basic event, map the fault tree according to the their logical relationship.

(2) Quantitative analysis of the electrical haulage shearer system.

① Simplify the fault tree, number the logical gates and basic events for further analysis.
② Calculate the failure rate of the basic event.
③ Calculate the occurrence rate of the top event.
④ Calculate the importance of parts of each basic event, including probability importance and criticality importance.
⑤ Establish the main control measures on key components individually according to the importance of each sub-system and elements.

#### *4.2.2 Shearer load database and faults database*

A remote data file submission scheme was developed to achieve a remote submission of shearer monitoring data by using the PHP language and B/S architecture. Through the automaton, the remote data was summarized and sent to database at headquarters to provide data for the simulation of shearer operation.

Using a new Browser/Server architecture, under Browser/Server three-layered architecture, the presentation, business logic and data service were divided into three individual units: presentation: Web browser; business logic: Web server with extension function of application program; data service: database server.

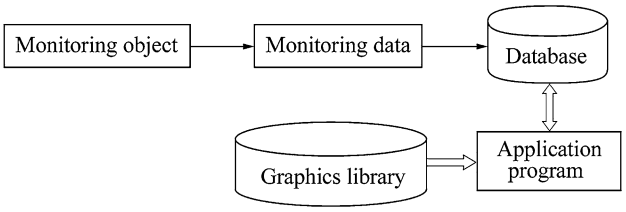


**Fig. 43** Relationship of monitoring objects, data and the graphic library

Monitoring objects are the monitored components in the shearer, which generate monitoring data. Monitoring data is the data converted from real-time signals generated by monitoring objects, which can be recognized by the computer. The graphic library in the monitoring system is composed of the instrument graphics of monitoring objects, which can be used by an application program. The relationship of three is shown in Fig. 43.

The parameters of the monitoring system of the electrical haulage shearer were mainly used to define the environmental parameters of system operations, including the parameters displayed at the client terminal and the parameters of network transmissions, and the geological parameters, mining parameters, gateroad parameters, the parameters of the scraper conveyor, the parameters of the hydraulic support, and the parameters of the shearer and its accessories.

Based on a whole configuration electric control system, the monitoring data of the shearer system is shown in Table 19.

Four current transformers were used in the shearer's electric control system to monitor the single-phase current of each cutting motor. In this case, the loading status of the motor can be known. The DC0-10 V voltage signal output from the current transformer is sent to PLC for comparison to obtain the signals of the underload or overload. Pt100 thermal resistances are installed inside the motor windings of four cutting motors on the left and right, haulage motors on the left and right. The thermal resistances are directly connected with the RTD module of PLC. The data collected are stored in CF cards as .csv files for subsequent data analysis. The visualization system of monitoring data connects the .csv files to the application programs through the ADO, OLE, and ODBC methods. The application programs input the data into corresponding database tables to display the data in a graphic format.

Based on the analysis on the requirement for the functions of monitoring the data visualization system, the

**Table 19** Data structure of the parameters of shearer operation condition

| Parameters | Variable type | Variable name | Note |
|---|---|---|---|
| Left cutting motor power | Float | LCMP | Left cutting motor power |
| Right cutting motor power | Float | RCMP | Right cutting motor power |
| Left haulage motor power | Float | LHMP | Left haulage motor power |
| Right haulage motor power | Float | RHMP | Right haulage motor power |
| Oil pump motor power | Float | OBMP | Oil pump motor power |
| Water pump motor power | Float | WBMP | Water pump motor power |
| Left cutting motor temperature | Float | LCMT | Left cutting motor temperature |
| Right cutting motor temperature | Float | RCMT | Right cutting motor temperature |
| Left haulage motor temperature | Float | LHMT | Left haulage motor temperature |
| Right haulage motor temperature | Float | RHMT | Right haulage motor temperature |
| Oil pump motor temperature | Float | OBMT | Oil pump motor temperature |
| Water pump motor temperature | Float | WBMT | Water pump motor temperature |
| Haulage direction | Bolean | HD | Haulage direction |
| Haulage speed | Float | HS | Haulage speed |
| Shearer position | Int | SP | Shearer position |

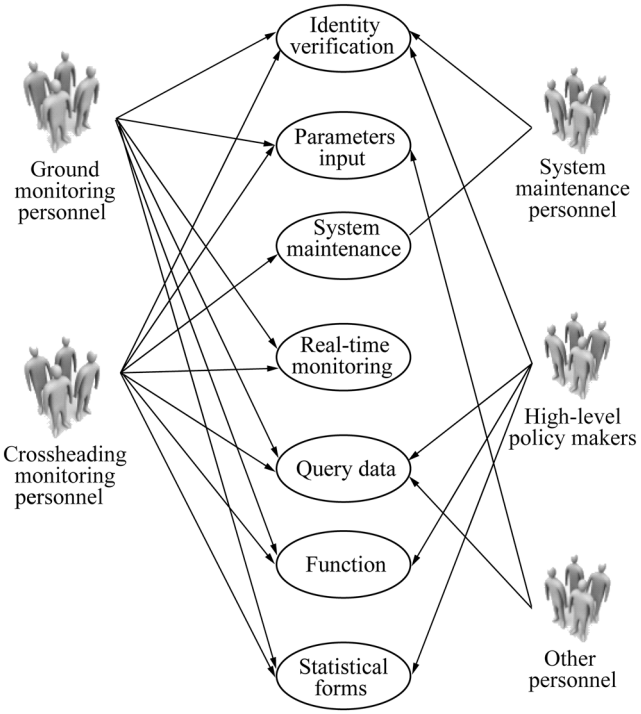


**Fig. 44** System case model for shearer monitoring data

system case model was established for the system, as shown in Fig. 44.

The large amount of monitoring data generated during the shearer operation were compiled and transferred into the database. After being processed in the database, the relevant data was extracted to link with the graphic library. The visualization of data was achieved. The large amount of historical data was analyzed and mined to form a decision support system.

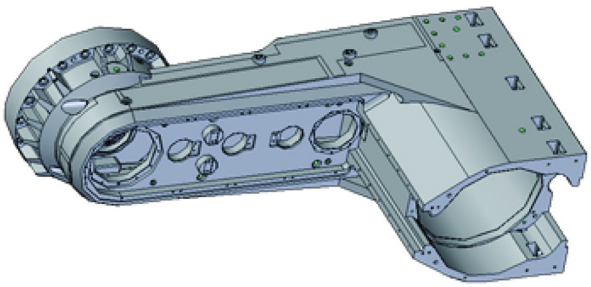

**Fig. 45** 3D model of shearer arm shell

### *4.2.3 Development of 750 kW high reliable shearer ranging arm*

Shearer's ranging arm shell (Fig. 45) is a power transmission part of drum rotary cutting and a supporting part of the curving movement of the drum. To enable the shearer's ranging arm maintaining its normal operation during the period of nominal coal cutting quantity (overhaul life maintenance), the arm shell should have excellent comprehensive mechanical properties, i.e., high tensile strength, high fatigue strength and hardness, and high impact toughness. As a result, a new material CrNiMo series of hardened and tempered steel was developed. The medium carbon CrNiMo series special cast steel material was selected because the alloy steel with Cr and Ni has a high strength, in addition to high plasticity and toughness. The addition of Mo can control the secondary temper brittleness, reduce overheating, increase temper stability and obtain high strength and toughness of steel after it is hardened and tempered. Because of the addition of Cr, Ni, Mo and other minor alloy elements in the alloy, the alloy

steel has a high hardenability. In addition, due to the solid solution strengthening of Ni and Mo elements, and the carbide precipitation strengthening of Cr and Mo elements, Mo and Cr elements hinder the growth of austenite grain, which will improve the strength, hardness and worn resistance of the alloy steel.

The large power ranging arm shell is made of large heterotypic cast steel, thus, it is in an irregular shape with large internal space and a complex structure. Furthermore, the shell's thicknesses vary significantly. Therefore, if the cooling rate after high temperature austenite is too fast, the shell might have cracks. At the same time, the alloy steel of the arm shell has a high hardenability, and has a high hardness under air quenching (air cooling, normalizing) with modest cooling rate. Therefore, during the process of air quenching and high temperature tempering, the rate and method of increasing temperature and the temperature of air quenching need to be appropriately controlled to meet the mechanical property requirements from the arm shell body, and prevent the occurrence of cracks.

The heat treatment of the shearer's ranging arm shell is high temperature tempering after air quenching (normalizing), which is completed before the machining of the shell. The process is: check before heat treatment—air quenching—intermediate check—tempering—final check. Figure 46 shows the normalized curve.

The shell cast outline of the split-type ranging arm is 2948 mm × 1434 mm × 961 mm, the minimum wall thickness is 45 mm, the maximum wall thickness is 119 mm, and the cast weight is 6380 kg. The position of water passage in the cast part needs to be tested in a hydrostatic test under eight standard atmospheric pressures, and the inner cavity is water leakage-proof. To make the castings with excellent mechanical properties, the density of the castings needs to be high and reaches GB 7233—87 II level in ultrasonic flaw detection. The geometry, allowance of machining, and dimensional deviation of the castings are consistent with the specifications of cast steel for engineering machinery JB/T 5939—1991. Therefore, based on ranging arm shell cast material composition based casting characteristics and structure, size, and casting weight level, the foundry program was determined, including the sand casting method and casting process (pouring position, parting surface, sand box structure and size). After the casting process was determined, the designs were conducted including the design of casting parameters, sand core design, gating system design, riser design, chill design, and vent design.

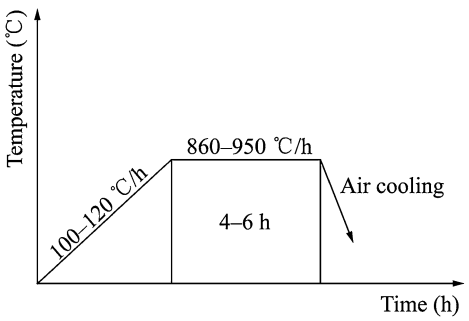


**Fig. 46** Normalizing curve

Ranging arm shell casting is a large heterotypic steel casting. A template sample manual molding was used. The molding sand is quartz sand with $SiO_2$ concentration greater than 96 %. The molding process used ester-hardened sodium silicate sand, core sand used 30–50 mesh of quartz sand, and binder used phenolic resin.

On the design of the outlet, sand core was used to make the exhaust channel, and the vent was reserved in sand mound. More vents were designed on the external mound upper box, in particular, on the sand mound upper box at the water jacket position of the ranging arm.

In terms of the design of feeding system, the gating and rising, and chill were appropriately laid out based on the modulus of each structural element by using the modulus method. The top insulation riser and side insulation riser were set up in the local area, and the external chill was placed. In addition, a riser subsidy was set up at necessary parts to feed castings.

With the computer numerical simulation of the process of shell mold filling and solidification, the casting process and parameters were optimized. Among them, the machining allowances were adjusted according to the JB/T5939—1991 the specifications of cast steel for construction machinery, and the shrinkage was set based on the inner cavity and external shape. In addition, using the lofting small casting test, the rationality and stability of the shell casting process was determined.

With the optimization of the casting process, the casting quality of the shell of the large power ranging arm was good in trial production. Through the process of heat treatment discussed above, the surface hardness test on the CrNiMo series casting steel of the ranging arm shell showed the hardness deviation in a reasonable arrange. The mechanical properties are as follows: Hardness HB200-240, tensile strength ≥700 MPa, yield strength ≥600 MPa, percentage elongation ≥18 %, area contraction ≥40 %, and impact toughness ≥70 J.

After using the technologies above, the performance of the shearer's ranging arm shells remained in good condition. The mechanical properties of the shell can meet the requirements of the high-power shearer.

In addition, the heat balance of the shearer ranging arm was investigated and a special forced lubrication and cooling device was developed. The heat of the shearer ranging arm comes mainly from the gears, bearings and stirring oil by gears. There are four main ways of heat

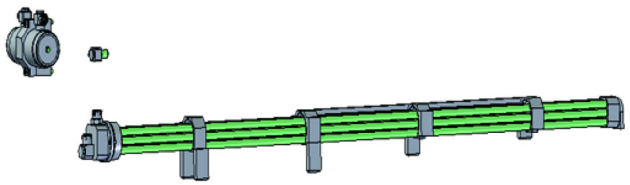

**Fig. 47** Built-in cooler

dissipation for the shearer ranging arm: convective heat transfer between the ranging arm shell and air flow; heat removal by the cooling water of the ranging arms; heat absorption by the lube oil of the ranging arm; radial heat transfer between ranging arm and its connection devices.

With the significant increase of ranging arm power, and the working requirements of equipment continuous transshipment by high production and high efficiency working face, it is difficult to solve the problem of heat caused by the loss of transmission efficiency through traditional methods. Thus, a dedicated heat balance system was set for the ranging arm. The design of the water jacket for the ranging arm shell was optimized. A cooling pipe was installed in the gear chamber. The built-in cooler is shown in Fig. 47. A hydraulic gear pump system was installed for forced lubrication and cooling. In addition, the temperature sensor was installed, when temperature exceeded the limit, the alarm was triggered. The design forms a unique, advanced and reliable ranging arm heat balance system.

In order to increase the service life of gears and bearings inside the ranging arm, and increase the reliability of the shearer, the hydraulic system of the gear pump was installed for forced lubrication and cooling. The ranging arm gearbox was used as an oil tank for the automatic lubrication device. At the other side of shearer ranging arm I, screw pump 1 was mounted. In the gear oil tank, N320 middle load gear oil was injected. The gear on axial group I drives the gears on the gear pump, and the lubricating oil in the pump, under the action of centrifugal force, was pumped out through the oil tube to filter, which filters out impurities in the oil. After the cooling, the oil was transported by pipeline to the axial group III, axial group IV, axial group V, axial group VI and axial group VII. Each axial group and gear had special holes drilled, and the lubricating oil lubricated the mating surfaces through the hole as the gear turned.

In order to clearly describe the effect of heat radiation on the shearer ranging arm temperature field after optimizing the cooler, the heat radiation without the cooler was theoretically and numerically analyzed when the ranging arm angle is 0° and ambient temperature is 0°. The temperature rise curve of the ranging arm (Fig. 48) and the color cloud of stead temperature field (Fig. 49) were obtained.

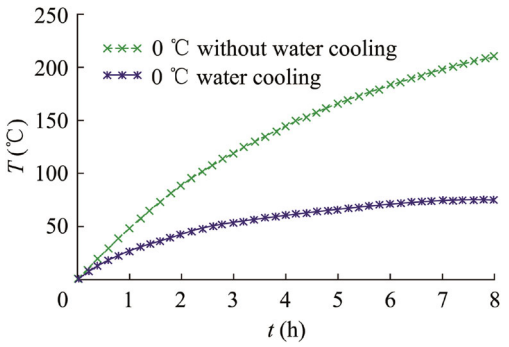


**Fig. 48** Temperature rise curve with the effect of water-cooling

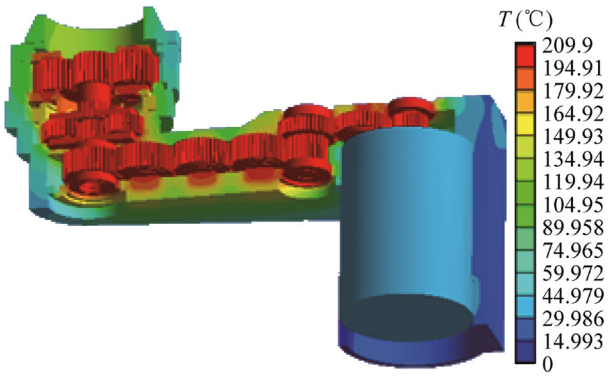


**Fig. 49** Temperature field of ranging arm without water-cooling at ambient temperature 0°

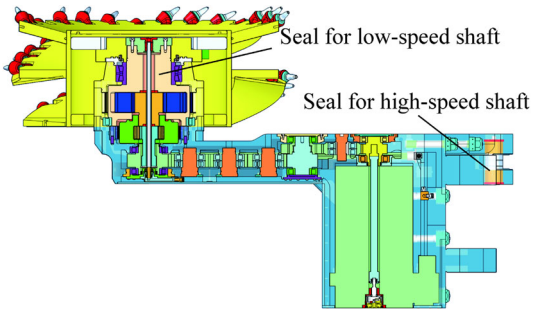


**Fig. 50** Locations of high speed and low speed seals on shearer ranging arm

As shown in Fig. 48, the effect of the water cooler after optimization on the temperature rise of the ranging arm is significant. Without the water cooler, the acceleration speed of temperature increase is very large. Figure 49 shows the distribution of the ranging arm temperature field without the water cooler under working conditions. Without the water cooler, the temperature gradient generated between transmission shaft and box is very large. It indicates that the water cooler of ranging arm design has solved the overheating problem with the 750 kW ranging arm. In addition, it provides a reference for the study on the heat

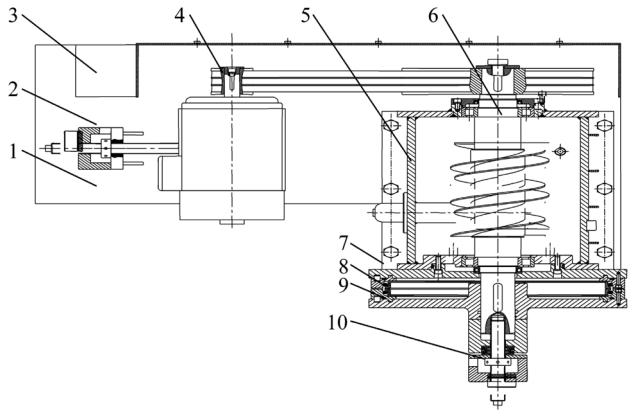


**Fig. 51** Major components of floating oil-seal test device. *1* Support, *2* 2 V belt tension device, *3* electric control console, *4* moter, *5* oil tank, *6* shaft, *7* static ring fixer, *8* float oil seal, *9* moving ring fixer, *10* axial loading device


**Fig. 52** Floating oil-seal test device. **a** Electric control console, **b** mechanical parts of test device

balance of large power ranging arms, and the optimization of cooler design.

In order to further improve the reliability of the shearer ranging arm, the seal performance of the shearer ranging arm was evaluated. In reality, the seal problems mainly appeared in moving seals. There are two moving seals in the ranging arm, one is the seal between drum connection sets and the gland at the output shaft of the ranging arm (low-speed shaft), the other is the seal between the ranging arm shaft I (high-speed shaft) and motor cavity body, as shown in Fig. 50.

Currently, a floating seal is used on the low-speed shaft seal of the ranging arm. The floating oil-seal is a sealing device combining dynamic and static sealing techniques. The floating oil-seal is composed of two identical metal rings (static floating seal ring and dynamic floating seal ring) and an "O" shape ring. In order to further understand the mechanism of the floating oil-sealing and optimize the assembly clearance, a test device of floating oil-seal was developed, as shown in Fig. 51. Figure 52 shows the photos of the test device.

The working principal of the floating oil-seal test device is as follows: a axial force is imposed on floating oil-seal through the axial loading device; the speed of floating oil-seal is adjusted through the electric control console, the oil temperature in floating oil-seal cavity and the test time of floating oil-seal are recorded; through the heater installed in the oil tank heat the oil in the tank, then the relationship between the axial force on floating oil-seal and assembly clearance can be measured; the floating oil-seal operation, and temperature increase and wear is monitored; and the oil leakage assembly clearance of floating oil-seal under static or dynamic status at a given temperature is detected. Main technical parameters of the test device are shown in Table 20.

Based on the main factors that affect the performance of the floating oil-seal, and the working principal of the test device, the routine test items and methods were determined as follows: hardness test on "O" type ring; test on the relationship between pressure and shift; static oil leakage test; test on the elastic resilience of the static "O" type ring; test on dynamic temperature rise; test on the operation of the floating oil-seal; test on dynamic oil leakage; test on the wearing condition of the floating oil-seal; test on service life; and the comparison of performance of floating oil-seals from different manufacturers.

The main problem for using the framework oil-seal of ranging arm's high-speed shaft is its premature failure, i.e., the failure before the service life of the framework oil-seal. The main causes of the premature failure for the framework oil-seal at the ranging arm shaft I are as follows: poor

**Table 20** Main technical parameters of test device of floating oil-seal

| Output (V) | Motor power (kW) | Variable frequency speed adjustment range (r/m) | Maximum output torque (N m) | Floating oil-seal size |
|---|---|---|---|---|
| 380 | 3 | 0–200 | 265 | $\phi$293–$\phi$560 |

**Table 21** Chemical composition of cladding materials (wt %)

| Sample | C | Si | Ti | V | Cr | Mn | Ni | Fe |
|---|---|---|---|---|---|---|---|---|
| A | 1.12–2–1.25 | – | 0.2 | – | 3.6 | 0.7 | – | Remains |
| B | 1.0–1.2 | 0.15 | – | 0.33 | 5.8 | 0.6 | – | Remains |
| C | 1.45–1.7 | 0.35 | 0.4 | – | 12.3 | 0.88 | 0.21 | Remains |
| D | 1.12–2–1.25 | – | 0.24 | 0.27 | 3.7 | 1.03 | 1.16 | Remains |

quality framework oil-seal, e.g., poor quality port, and defects; poor quality of self-tightening spring; the magnitude interference between port inner diameter and shaft I outer diameter is too small, which results in low radial pressure; and the material of framework oil-seal is not good, which results in wearing out at port. Design and machining: there are some misalignments at some positions, such as ranging arm, shaft I and bearing cup; there is a low degree of finish at shaft I that amounted with framework oil-seal; and inappropriate heat treatment, etc. Assembly: damage on the port of framework oil-seal, inclination of bearing cup, loose spring, different type of grease or different quantify of grease on oil-seal port and shaft surface. To overcome the problems associated with the framework oil-seal of ranging arm shaft I, and to increase the sealing reliability of high-speed shaft of ranging arm, the following measures were taken: select high quality framework oil-seals; maintain the machining precision of key components; checking and maintenance on oil leakage of the framework oil-seal.

#### *4.2.4 High speed ultra-powerful pin and rail haulage system*

Based on the previous system, a high speed ultra-powerful chainless haulage system was developed. It has a rated traction of 2 × 570 kN and a traction speed of up to 20 m/min.

The clearance matching of chainless haulage system with a pitch of 147 mm was studied. First of all, the variable range of meshing central distance of the shearer walk wheel and scraper conveyor pin rail was determined. Its determination principles are: under the correct meshing situation, the minimum meshing central distance can warrant the no interference and no gear jam between walk wheel and pin rail (two section pin row connection), and it is usually approximately 10 mm less than the pitch radius of the walk wheel; the maximum meshing central distance must satisfy the rational meshing, the simulation shows that the increase of the meshing central distance has little effect, based on analysis and experience, the value is taken as 15 mm larger than the corresponding pitch radius of the walk wheel; a further increase of meshing central distance would cause: imprecise rolling, impact on gears from every contact and alteration, the wear of wheel gear and rack gear, etc.

The wear resistance of components in the chainless haulage system of maximum traction force 2 × 570 kN was investigated. In the study, four types of cladding materials A, B, C and D were studied; the cladding of substrate steel can dramatically improve the surface hardness and abrasion resistance of the substrate. Based on the analysis, the C type is the hardest cladding layer among the four types of cladding material, up to HRC66.9, the A cladding layer is a less hard layer, the B cladding layer is the least hard layer, with its hardness reaching HRC51. The friction and wear test showed that the four types of cladding layers have the same wearing manner, e.g., abrasive and adhesive wears. Among the four types of cladding materials, the wear resistance of A is the best, followed by B, C and D that have the same wear resistance. Cladding material is Fe-based alloy powder; its chemical composition is shown in Table 21.

The modified substrate steel after the cladding of Fe–Cr-Mn–Ti Fe-based alloy powder has an A cladding layer and a high hardness, excellent anti-wear properties, and a substrate with very good toughness, and is superior to any other alloy steel wear-resistant material. This modified substrate steel can be used as the shearer's guide sliding shoe material to meet the performance requirements of the shearer guide sliding shoe under complicated mining conditions.

#### *4.2.5 Development of large-diameter, ultra-powerful and wear-resistance spiral drums with pick-shaped cutter and its components*

The shearer's pick holder and welding process were investigated. In earlier years, the pick holder of a small power shearer was cast with medium carbon steel. The common damage of pick holders were: weld cracking; overall cracking along pin hole due to high substrate hardness, poor plastic toughness; surface wear due mainly to poor surface organization, low hardness, poor wear resistance; inner hole wear due to poor surface organization, low hardness, and poor wear resistance. Comparison of different materials for the pick holders is shown in Table 22.

**Table 22** Comparison of material properties

| Property | ZG40Cr | 35CrMnSi | 15CrNi$_3$MoA |
|---|---|---|---|
| Material property | Not compact, many defects, low strength, low plasticity | High strength, good plasticity | High strength, excellent plasticity |
| Processing property | Poor hardnessability, high carbon-equivalent, poor welding property | Good hardnessability, high carbon-equivalent, poor welding property | Good hardnessability, low carbon-equivalent, good wielding property |
| Application property | Same surface hardness. In terms of the core, hardness is too high, poor plasticity, poor impact resistance; in terms of surface, hardness is too high, poor wear resistance | Same surface hardness. In terms of the core, hardness is too high, poor plasticity, poor impact resistance; in terms of surface, hardness is too high, poor wear resistance | After carburizing and quenching, the hardness at core is appropriate, good plasticity, high surface hardness, good wear resistance |

In order to better meet the working conditions of shearer's pick holders, a low carbon alloy steel 15CrNi3-MoA was used to make the pick holder which was subsequently treated by carburizing and quenching. Because the carbon content of the material is low, its carbon equivalent is also low and its welding property is good. The total alloy element content is low, therefore it is low cost, but its hardenability is high. After carburizing and quenching, the carburized layer is martensite plus carbide, its hardness exceeds 58 HRC, so the surface wear resistance is good, and substrate is a thin lath martensite. A material with a hardness of approximately 300 HB, a strong toughness, and strong impact resistance, would be a more appropriate for making pick holders.

The wear process of the shearer drum helical vane was studied. In poor production conditions, the tail end of the shearer drum helical vane was often worn out. After a comparative study of several methods, the chrome SA1750CR wear-resistant composite plate was selected. The plate is made as follows: using the heap welding method, a layer of high chrome and carbide material are surfaced on a low alloy steel plate, and form a heap welding layer with high wear property, while the back of the plate has high toughness property; the large difference in the properties of front and back side of the composite plate results in the large improvement in the properties of bending, welding and mechanical processing of composite plate and original low carbon alloy steel plate.

#### *4.2.6 Development of the prototype shearer and performance test*

Based on earlier studies in June 2009, the Shanghai Branch of Tiandi Science & Technology Co., Ltd commenced the manufacture of the prototype shearer and completed in February 2010. The key process of its main components is described as follows:

As the MG750/1915-GWD shearer developed is a heavy-duty large power shearer, large casting shells, such as ranging arms and traction gearbox, are heavy in weight, and the cavity structure is complex and the thickness is uneven. Through software simulation, the parameters of the riser, such as number, size and position, were rationally designed to effectively avoid the casting defects, e.g. cracks and loose. To overcome the problem of blowholes in casting, in terms of process, a vent was made on the core and on the sand box. In addition, a well-shaped exhaust duct was made on the sand box. Large particles of synthetic quartz sand were used as the back sand. In these ways, the casting blowhole was effectively eliminated. In addition, the measures of a one-box multi-core combined tool and a core with multiple positioning were applied to ensure dimensional accuracy. In the machining process, the benchmark superposition method was used to achieve location accuracy. Before semi-finishing machining, a baseline was mapped properly, and the base surface was machined properly. Based on the correct baseline, the surface of each hole was machined in semi-finishing or finishing. To meet the requirements of geometric tolerances of some holes, a one clamping multichannel processing method was used to ensure the requirements of finishing size. A "casting-air quenching and high temperature tempering-rough-finishing-stress removal tempering-finishing" processing route was used to ensure the strength and dimensional stability of the castings. With the development of materials and the processing method, on the basis of solderability, the hardness of ranging arm shell reaches 200–240 HB, and the tensile strength reaches $\sigma_b \geq 700$ MPa, which greatly enhances the mechanical properties.

Before forging the gear, the oxidized layer and surface defects were removed using a hand sand wheel to effectively avoid the cracking phenomenon of forging residue. In the forging process, the procedures must be strictly followed; the forging temperature must be strictly controlled with the temperature difference not exceeding 300 °C. After forging, the forging part must be normalized under more than 950 °C and tempered less than 600 °C to eliminate forging stress and improve cutting performance. After a rough-machining of the gear blank, each part

underwent an ultrasonic defect check. A grinding undercut large radius hob was used for gear grinding to increase gear root fillet, and improve the impact resistance and bearing capacity of gears. In the carburizing and quenching heat treatment process, the carbon potential concentrations were strictly controlled at 0.8 %–1.0 %. A "quenching + deep freezing + low temperature tempering" process was used to ensure that the gear surface hardness reached HRC58-62, surface carbide reached Grade 1–3, the depth of effective hardened layer reached 1.5–1.7 mm range (including grinding), core hardness reached HRC38 approximately, and retained austenite content was less than 9 %. All gears were ground in high precision grinding machine NILES, and some of the key components, such as planetary gear and sun gear, were under tip relief operation. At the same time, the accuracy of gear machining was one level higher than the specified level on the drawings to ensure a good meshing of the gears. The ground gears were treated by strengthened shot blast to eliminate the burns on the tooth surface and increase residual compressive stress, thereby enhancing the gear's contact fatigue strength and bending fatigue strength.

The working conditions of the shearer walk gear are harsh, thus the shearer walk gear is one of the weakest parts in the shearer. In order to improve its work life, the electro-slag remelted steel material 18Cr2Ni4WE was used to make the shearer walk gear. The electro-slag remelting greatly reduces the harmful content of non-metallic materials (these ingredients are the causes of quenching crack and fatigue crack), increases the purity of materials, and maximizes material performance. As the gear modulus was large and there was no standard hob, the gear tooth was machined twice, the first machining cut using NC wire cutting, leaving 2–3 mm allowance. The second machining was precisely machined to its place using a processing center. In particular, in the last processes, the amount of feed and cutting speed should be strictly controlled to avoid obvious cutting marks (machining marks are the stress concentration source of gear's tooth; currently fracturing of the shearer walk gear is often caused by these marks). To reduce the gear tooth's early failure due to stress concentration, it should be treated by shot-blast after heat treatment.

High quality medium carbon alloy steel was used to cast the shearer's guiding sliding shoe. At rough machining, the shoe was hardened and tempered to improve its substrate mechanical properties. The high quality wear-resistance material was selected to heap weld the guiding surface, then, the surface was machined using a special machine to reduce the surface roughness and friction force.

The trial production of other components also strictly followed the product standard and were checked to avoid installing non-confirming products in the prototype shearer, and can warrant the reliability of the shearer manufactured.

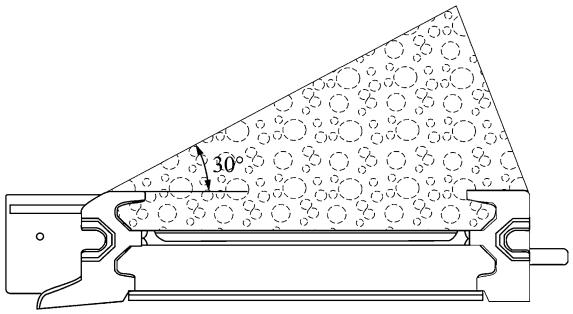


**Fig. 53** Cross-section of coal transportation at rear scraper conveyor

### 4.3 Rear scraper conveyor for LLTCC coal face

In order to meet the requirements of coal production of 1000 Mtpa at the No. 8105 face in Tashan coal mine, with the consideration of the effects of other uncertain factors, the calculation shows that the total transportation capacity of the front and rear scraper conveyors is 3500 t/h. Considering a cutting and caving ratio of 1:3, the individual transportation capacity of the front and rear scraper conveyors should be greater than 2625 t/h. Taking the uncertainty of caving quantity and some allowances in transportation capacity into consideration, the capacity of the rear scraper conveyor was determined as 3000 t/h.

Because of the specific environment in the underground mine and the matching characteristics of the scraper conveyor, shearer and hydraulic support, there are many constraints on many structural parameters of the scraper conveyor including the width of the pan and other important structural parameters. Balancing between economic and technical contexts, the pan width of the rear scraper conveyor was determined as 1200 mm. Its coal transport section is shown in Fig. 53.

Calculation of chain speed of scraper $V$:

$$V = n/2iZp/60\lambda \tag{17}$$

where $n$ is the motor speed, 149 $\text{min}^{-1}$; $i$ is the reduce deceleration ratio, 28.43; $Z$ is the tooth number of driving sprocket, 7; $P$ is the chain pitch of 48 × 154, 0.152 m; $\lambda$ is the slip ratio of coupler, 0.95. Substitute the parameters into Eq. (17), get:

$$V = 1491/28.43 \times 2 \times 7 \times 0.152/60 \times 0.95 \approx 1.77 \text{ m/s}$$

Calculate the hourly capacity of coal transportation $Q$:

$$Q = 3600\, VA\rho \tag{18}$$

where $V$ is 1.77 m/s; $A$ is the cross-section of loads as to rear conveyor, because the top of the cross-section is open,

based on the coals rest angle of 30°, the calculated coal transportation area $A = 0.63$ m$^2$; $\rho$ is the loose coal density, 0.85–1.0 t/m$^3$, select 0.9 t/m$^3$. Substitute the data into Eq. (18), get: $Q = 3600 \times 1.77 \times 0.63 \times 0.9 \approx 3613$ t/h $>$ 3000 t/h,meet the requirements.

Based on a conveying capacity of 3000 t/h and a chain speed of 1.77 m/s, and the installed power of 2000 kW, the theoretical power consumption utilization was analyzed under the conditions of face lengths of 300, 250 and 207 m respectively (the actual length at the No. 8105 face in Tashan coal mine). The calculation results showed that: when the face length is 300 m, and face dip is 0°, the power utilization reaches up to 94.3 %, power margin is small, which is only used in a flat or downhill face. When the face length is 250 m (or the actual face length at No. 8105 face is 207 m), and the face dip is 0°, the power utilization is 78.6 % and 65 %, respectively, showing a large margin. Therefore, a total power of 2 × 1000 kW can meet the requirement of transport capacity of 3000 t/h.

In order to warrant the non-fracture of the scraper chain, the safety coefficient of the chain was calculated. When the total power is 2000 kW, scraper chain speed is 1.77 m/s and the broken load of scraper chain is 3290 kN, the safety coefficient of scraper chain should reach 1.72 to satisfy the requirements of safe coal transportation.

Based on the analysis discussed, SGZ1200/2 × 1000 large load rear scraper conveyor was selected for the LLTCC face to extract the ultra-thick coal seam at Tashan coal mine. The installed power is 2 × 1000 kW, and transportation capacity exceeds 3000 t/h. The transportation distance meets the length requirement at the No. 8105 face.

In a LLTCC mining operation, the rear scraper conveyor should have reasonable technical parameters and structure; also, the key components should have high reliability. These key elements include a heavy-duty high-strength chain drive system, speed-adjustable soft start device, integrated monitoring transmission system of transmission device, heavy-loaded 1000 kW planetary retarder, high reliability long life high-strength coal transportation trough, high strength compact end discharge frame and automatic retractable tail with electro-hydraulic control, etc.

With the development of 48 × 152 compact high-strength round chain and link chain for the mine, as well as the high-strength forged scraper, the optimization of the meshing characteristics of the chain transmission system and the adaptability and chain tension, along with the development of along life 48 × 152 drive sprocket and component, a heavy-duty high-strength chain transmission system was successfully developed.

By studying the matching ability of controlled adjustable speed soft start device-valve-controlled hydraulic coupler and motor load characteristics, a rational coupler cavity has been designed and the fluid dynamics was optimized. In addition, an electro-hydraulic control technology for the coupler has been developed. A large power valve-controlled hydraulic coupler has been developed with intellectual property rights.

A comprehensive monitoring integrated transmission system has been developed. It consists of central monitoring equipment (upper equipment) and site monitoring equipment (lower equipment), which achieves a state monitoring and control on the transmission device of the rear scraper conveyor, and enhances the operation monitoring capacity of the large power rear scraper conveyor.

Through a combination method of theoretical analysis, three dimensional modelling, mechanical analysis and simulation, virtual prototyping, dynamic testing, bench testing, and industrial trial, a 1000 kW retarder for the mine has been developed.

Through the study on the bending angle design of the middle pan, and the connection method of U-shaped port of middle pan, in addition to the large amount of research and testing on the choice of materials, welding processes and equipment, and machining technology, a high-reliability, long-life coal pan has been developed.

Through the strength design on the end discharge head frame, the connection design of the head frame and joint parts, the connection design of the head frame and transition pan was improved. A high strength, compact end discharge head frame has been developed.

With the analysis on the operating conditions of the scraper conveyor chain, and the calculation on the adjustment required by conveyor tail and the calculation of traction force of the extension mechanism, an automatic retractable conveyor tail electro-hydraulic control system and retractable extension tail frame has been developed. Furthermore, an electro-hydraulic automatic control retractable conveyor tail has been developed.

Through the research and development of the key technologies and components above, the overall reliability of the rear scraper conveyor has been improved to warrant safe, efficient and stable operation.

### 4.4 Large-capacity and long distance gateroad belt conveyor

In order to achieve the transportation of both the coals extracted by the shearer and the coals extracted by top coal caving from the LLTCC operations, the technologies on a large-capacity long-distance gateroad belt conveyor has been investigated.

A CST soft drive system was used, in light loads or heave loads condition, the dynamic process of the loaded belt conveyor's soft start/soft stop can effectively be

controlled to achieve a balance of power among various drives.

Based on the variation of tensile force during the start, stop and operation of belt conveyor, a tension technology and equipment of high accuracy and large tensioning stroke has been developed. It can quickly respond and automatically adjust tension and tensioning stroke with the tension variation of the belt conveyor. During normal operations, the tensile force is 0.9–1.1 times of the rated tensile force, during start and stop, the tensile force is 1.3–1.4 times of the rated tensile force, and during the shift of conveyor tail, the equipment can quickly respond and guarantee non-skid. The working principle is: based on the conveyor's start-up and loading, with the feedback of tension sensor signal, the PLC controller and fuel tank can automatically adjust the output of tensile force to avoid slipping between belts and drive pulley, lower the safety factor selected for the belt, and ensure the normal operation of the belt conveyor. Installed with an automatic moved conveyor tail, the automatic tensioning can be achieved when the conveyor tail is automatically moved, thus to a certain extent, the downtime rate of the belt conveyor and the downtime rate of the three face machine can be reduced.

A new high-efficiency belt storage device was developed; the belt can be folded into six layers and stored with a length of 200 m. A belt storage system of multi-layer winding has been developed, which enables an automatic belt central alignment to overcome the deviation of conveyor belts in storage and the tensioning truck's off track.

A low speed large torque hydraulic motor and electro-hydraulic proportional control valves were used to develop a large-torque belt-speed controllable high efficiency hydraulic belt winding device, which significantly reduces the time on belt winding, is easy in operation, and reliable in working.

A high-speed low-friction larger-diameter roller was developed. Using labyrinth seals with special structure and oxidation resistance, water-resistance grease sealing method, the service life of the high-speed large-diameter roller is significantly increased.

**Fig. 54** The large-capacity, long-distance belt conveyor

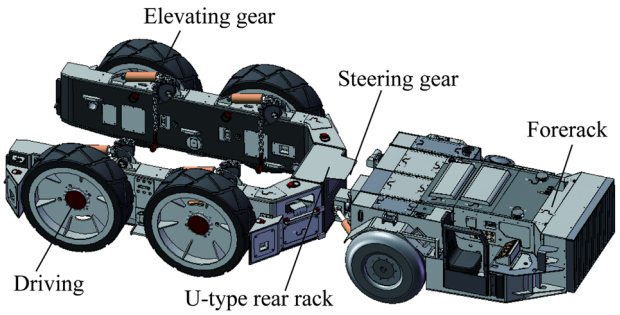


**Fig. 55** WC55Y shield hauler

Using dynamic analysis software, the system was analyzed to determine a reasonable starting and braking curve. An advanced PLC programmable controller was developed. In addition, an advanced program-controlled automatic monitoring system was developed, which can conduct the operations of data collection, processing, storage, transmission, fault detection, reach and feed, etc. It can meet the requirements of the conveyor's controllable soft start and braking, power balance, automatic tensioning and self-movement of conveyor tail, as well as various functions, such as protection, communication and signal contact. In addition, it can monitor the various protection and safety devices, conveyor belt tension, the temperature of the driving drum and roller bearing, the measurement of throughput, etc.

Through the studies presented, a large-capacity, long-distance belt conveyor has been developed, as shown in Fig. 54. Its main technical parameters are as follows: transportation distance: 2800 m; transportation capacity: 3500 t/h; lifting height: 35 m; belt width: 1400 mm; installed power: 1680 (3 × 500) kW; belt speed: ≥4.5 m/s; stored belt length: ≥120 m.

### 4.5 Large tonnage shield hauler

The tonnage of hydraulic support for the working face in thick and ultra-thick coal seam is very large. In order to improve the efficiency of coal mining, it requires a fast relocation of coal face equipment. Therefore, a heavy-duty frame shield hauler—WC55Y shield hauler was developed, as shown in Fig. 55. The vehicle is powered by diesel, the carrying capacity is 55 t, and is an efficient equipment for a quick relocation of coalface. If equipped with a hopper, it also can be used as a multifunctional underground transport vehicle.

A V-type six-cylinder diesel engine explosion-proof equipment was used in the WC55Y shield hauler. Based on the requirements of explosion-proofing, the explosion-proof device must be set up in engine intake and exhaust systems, which will increase the resistances of engine's

intake and exhaust, reducing engine efficiency, worsen the harmful emissions, and increase the pollution in underground. The difficulty in this project is how to optimize the inlet and outlet structures to minimize its effect on engine performance and reduce the emissions of harmful gases. In terms of the engine's explosion-proofing, the following four key technologies have been developed:

(1) In the explosion-proof diesel engine, exhaust turbocharged water–air cooling technology was used. Forced water circulation technology was used to solve the high temperature problem with the supercharger surface. Compared to natural air intake, the air intake increases 30 %, and lays a foundation for increasing efficiency and reducing emission.
(2) Using theoretical analysis and test methods, the fuel injection control was optimized. The oil injection method of low-speed in the early stages, high-speed in the middle stages and reduced speed in later stages was used to effectively control the emission of NO*x*, PT, etc.
(3) Intake resistance is an important factor affecting engine power. The intake spark arrestor is a key component of the air intake system in explosion-proofing the diesel engine, which directly affects engine performance. Through the experiment, after the installation of the air inlet device on the diesel engine, the losses of power and torque is up to 14 %. To improve the flow characteristics of the diesel engine intake, the original structure had been optimized. With a comparative analysis of eddy current resistance loss at inlet/outlet section in different intake spark arrestors, an inclined windward surface end grid plate was designed to substantially reduce inlet resistance.
(4) A constant pressure low resistance exhaust gas treatment device was designed. Using a water bath type cylindrical structure, the exhaust resistance was reduced by 5 %.

For the WC55Y shield hauler, a moving speed brake was developed, which integrates a planetary speed retarder and a large torque wetted multi-disc safe brake. Traditional brake concentrates on the high-speed end of wheel-side retarder, and is small in dimension. However, under a larger braking torque and repeated braking, the system generates large amount of heat and consistently fails. The working condition of the shield hauler is harsh. In the aspect of driveless axle hydraulic-driven design, there have been no successful braking studies anywhere in the world. Fully enclosed, high torque and large brake power, small in size, and high efficiency heat dissipation are the difficulties in the study. Meanwhile, the road underground is potholed, thus during the movement of heavy-loaded vehicles, the wheel-side retarder will withstand a greater shock load, and therefore must have enough strength. Otherwise, it will cause failures in the retarder's bearing, such as broken parts. In response to these technical bottlenecks, a "modular integrated technology" was used to design a new planetary gear of wetted multiple-disc brake. Also, an integrated motor-cartridge wheel drive and brake retarder was invented. It is a wheel-side planetary retarder, and integrates all brake functions. The brake was designed as a fully closed wetted-type multi-disc brake with spring braking and hydraulic release. Through the spline, friction tablets and steel tablets are coupled with fixed parts and turned parts respectively. Through the motor input, retarder part input torque, delivered via a two level planetary deceleration device, the torque will be transmitted to the wheels. The brake cavity and retarder cavity are completely insulated by a pair of high reliable floating seals to avoid the interference of two different functions. The braking torque of the integrated brake-retarder is greater than 60,000 N m, thermal equilibrium temperature is less than 90 C° under long term braking, and the average life of the friction disc is greater than 5000 h. Furthermore, it is safe, reliable, has good pollution resistance, and increases operational safety.

The main performance indicators of the WC55Y shield hauler developed are: rated load 55 t, minimum ground clearance 300 mm, full load speed 0–12 km/h and climbing ability 12°, engine rated power after explosion-proof 220 kW, turning radius 2800 mm (inside) and 7000 mm (outside). The WC55Y shield hauler was used in the relocation of the LLTCC coalface at 14–20 m thick ultra-thick coal seam in the Tashan coal mine to successfully solve the relocation problem of large-tonnage hydraulic support at a LLTCC coalface.

## 5 Bolt support technology of large cross-section roadway in ultra-thick coal seam

### 5.1 Deformation and failure characteristics of the surrounding rocks of coal roadway with a large cross-section in ultra-thick coal seam

The roadways for a LLTCC coalface include headgate, tailgate, top return airway and open-off cut. These roadways are responsible for equipment installation, transportation, ventilation, gas exhaust, personnel passage, etc. A safe, efficient coalface depends on roadway stability and smooth flow. Roadway support is a key to the LLTCC mining operation.

The roadway of a LLTCC coal face has following characteristics:

(1) The headgate, tailgate and open-off cut are developed along the coal seam. The roof is top coals with an average thickness of 12.9 m. Compared to rock, the coal seam is relatively soft, fractured, and thick. The top coal is easily subsided and even caved, which significantly increases the difficulty of roadway support.
(2) Because the power of mining equipment is large, and face production is high, a very large cross-section of the roadway is required. The tailgate and the headgate have a same cross-section with a width of 5.5 m wide, a height of 3.9 m and a size of 21.45 $m^2$. The open-off cut span is up to 10 m. The increase of roadway width can result in significant bending subsidence in the roof, and large height roadway can cause coal wall buckling and even spalling, which significantly affects the stability of the surrounding rock of the roadway, and brings great difficulties to roadway support.
(3) The tailgate suffers the side-abutment pressure caused by the previous longwal gob and the and the front abutment pressure caused by the current longwall panel. In addition, due to the distinct characteristics of ground pressure at a LLTCC coalface, the mining effect on the tailgate is very strong, resulting in serious damage of the surrounding rocks.

### 5.2 Bolt support mechanism of large cross-section coal roadway

Roadway support with bolt and cable has become one of the main methods at coal mines in China. In this project, bolts and cables were used to support the large cross-section coal roadway. However, the surrounding rock of the roadway in the coal seam is soft and fractured. Traditional bolt supporting failed to suppress the large deformation of the roadway due to the high mining-induced stresses. Bolt supporting mechanism for coal roadways should be investigated to provide a theoretical basis for support design.

Many studies have been conducted to investigate the support mechanism of bolt and cable support on coal roadways (Jia and Huang 2005; Zhang et al. 2006; Ma and Zhang 2008; Zhang and Yang 2010) in China. In recent years, it has been recognized that the prestress of rock bolts plays an important role in bolt support (Kang et al. 2007a, b, 2008; Wang et al. 2008; Zhang et al. 2010), such as the binding effect it plays on the layer separation, slippage, and join crack opening of the surrounding rock surface layer, and maintaining the integrity of the surrounding rock. The studies improve the bolting effect, in particular, providing an effective theoretical guidance for complicated roadway support.

Based on the deformation characteristics of large cross-section coal roadway in ultra-thick coal seam, a full coal roadway supporting mechanism is proposed.

(1) The deformation of surrounding rock in a full coal roadway consists of two parts: one is the dilatancy deformation including the separation of coal and rock, sliding, fissures opening, and new cracks at their structural plane; the second is the elastic deformation of surrounding rock and the plastic deformation before its peak strength, and a full deformation of anchorage zone. A reasonable full coal seam roadway support should greatly improve the stiffness and strength of supporting system at initial support, effectively controlling the dilatancy deformation of the surrounding rock, and maintaining the integrity of top coals. At the same time, the supporting system should have sufficient elongation and allow a second deformation to release high stress.
(2) The prestresses of bolts and anchors play a decisive role in roadway support. It is crucial for support design to determine reasonable prestresses according to coal roadway conditions, and enabling prestresses to effectively spread.
(3) The anchor cable in a full coal seam roadway plays its role in two main aspects: one is to connect the bearing structure formed by bolting in top coal with deep surrounding rock in order to improve the stability of load bearing structures; the other is that the large prestresses of anchor cables and the compressive zone of bolts form a skeleton mesh structure to actively support surrounding rock.
(4) In a full coal seam roadway, high prestress powerful bolt and anchor cables should be used to become the single necessary support during the service life of the roadway, avoiding second roadway support and roadway maintenance.

### 5.3 Material of high strength bolt and cable

The yield strength of a traditional thread steel bolt is 335–500 MPa, and the tensile strength is 470–650 MPa, which is applicable to the roadway with normal conditions. For a roadway under complex geological and geotechnical conditions, a higher strength and sufficient elongation steel should be used for bolts and anchor cables in order to achieve high prestress, high strength and high elongation.

In this project, with the cooperation of other steel mills, strong steel for bolts and cables has been developed. The key technology and difficulties in developing this type of

**Table 23** High strength bolt steel

| Strength level (MPa) | Yield (MPa) | Tensile strength (MPa) | Shock absorb energy (J) | Elongation (%) |
|---|---|---|---|---|
| 500 | 570 | 745 | 89.0 | 26.0 |
| 600 | 650 | 805 | 42.6 | 22.0 |

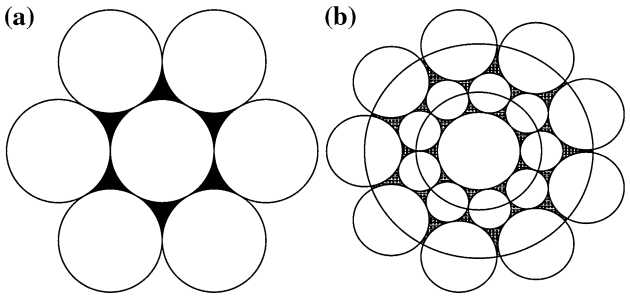


**Fig. 56** Anchor cable structure. **a** 1 × 7 structure, **b** 1 × 19 structure

steel is to greatly improve the bolt strength, and simultaneously, maintain sufficient elongation and impact toughness of the bolt to prevent bolt fracture and breaking under impact loads, bending and shear loads. Starting from steelmaking, a special bolt steel formula was formulated, e.g., adding elements of V, Nb and Ti in the steel to alter the mechanical properties of steel. In addition, an appropriate rolling process was used to manufacture the bolt in accordance with its technical specifications. Table 23 lists two kinds of anchor bolt steel developed with high strength, high elongation, and high impact toughness. The yield strength of the two types of boltreaches 570 and 650 MPa respectively, and the tensile strength reaches 745 MPa and 805 MPa respectively. The elongation is 26 % and 22 % respectively, and their shock absorbing energy is more than 40 J.

### 5.4 Cable material with large tonnage and high elongation

The anchor cable steel strand widely used in Chinese coal mines is composed of seven wires (Fig. 56a), with a diameter of 15.2 or 17.8 mm. Its application in underground coal mines showed the following disadvantages: the cable diameter is small and doesn't match borehole diameter, thus, significantly affects anchorage force, and is prone to the anchor end sliding. Due to its small breaking load, cable fractures often occur. Because of its low elongation, it cannot adapt to the large deformation of the surrounding rock. Due to its low prestress, it is poor in controlling the separation of rock layers.

To solve the problems discussed above, a large diameter, high tonnage strong anchor cable series was developed with a diameter of 18–22 mm, and a capacity of 400–550 kN. The technological approaches used are as follows: (1) changing cable body structure. Using new type of 19 wires (Fig. 56b) to replace the original seven wires, the cable body structure is more reasonable, and the anchor cable elongation has been significantly improved; (2) increasing the diameter of anchor cable body. The cable diameter was increased from 15.2 to 18, 20 and 22 mm to improve the cable body's broken force, and match the cable diameter and drilling diameter. The anchor cable with a diameter of 22 mm has a breaking load of greater than 600 kN, and an elongation of 7 %. The comparison of different mechanical properties of anchor cable steel strand wires are shown in Table 24.

### 5.5 Equipment for applying high prestress on bolt

As mentioned previously, the prestress of rock bolts is one of the key parameters for bolting, and plays a decisive role on the effect of anchor support. The previous studies show that the anchor prestress should reach a level of 30 %–50 % of anchor yield strength. According to the conversion relationship, the bolts' tightening torque should be 300–500 N m. To reach such a high prestress, the existing single bolting machines in China cannot meet such a requirement. It is necessary to develop a suitable bolt

**Table 24** Mechanical properties of different anchor cable strand wires

| Structure of steel strand wires | Diameter (mm) | Cross-section ($mm^2$) | Tensile strength (MPa) | Breaking load (kN) | Elongation (%) |
|---|---|---|---|---|---|
| 1 × 7 | 15.2 | 140 | 1860 | 260 | 3.5 |
| | 17.8 | 191 | 1860 | 355 | 4.0 |
| | 19.0 | 218 | 1860 | 406 | 4.5 |
| 1 × 19 | 18 | 215.5 | 1897 | 409 | 6.8 |
| | 20 | 262.4 | 1862 | 489 | – |
| | 22 | 321.6 | 1887 | 607 | 7.0 |

**Table 25** Physical and mechanical parameters of coal and rock seams in a numerical model

| Lithology | Density ($kg/m^3$) | Volume modulus (GPa) | Shear modulus (Pa) | Cohesion (MPa) | Friction angle (°) | Tensile strength (MPa) |
|---|---|---|---|---|---|---|
| Sandstone | 2650 | 25.3 | 18.2 | 22 | 44 | 1.6 |
| Coal | 1500 | 6.5 | 3.9 | 7.9 | 36 | 0.6 |
| Sandy mudstone | 2600 | 8.85 | 5.8 | 9.2 | 41 | 0.8 |

tightening tool to significantly increase the anchor cable's prestress.

In terms of the equipment for bolting, there are two main methods for increasing bolt's prestress (Kang and Wang 2007): one is to increase the bolt-nut tightening torque; the second is to use a bolt tensioning device, which is similar to imposing large prestresses on anchor bolts. The methods for improving bolt-nut tightening torque include: (1) high torque jumbolter. With a high torque jumbolter, it can not only increase the bolt tightening torque, but also achieve an integration of bolt installation to improve installation speed. For instance, the torque of the jumbolter used with continuous miner can reach more than 300 N m. The rated torque of a single jumbolter in China is not greater than 150 N m, and unable to meet the requirement of high tightening torque of the bolt. (2) Torque multiplier. In order to improve the installation torque of the jumbolter, a torque multiplier can be used on the jumbolter to multiply the nut tightening torque when installing bolt. (3) Torque wrench. Using a large torque preload wrench to tighten the bolts and nuts is an effective way to improve the prestress of anchor bolts.

Based on the jumbolter used in large cross-section coal roadway, and the operation conditions, torque multiplier was selected to improve the prestress of anchor bolts. The bolt torque multiplier developed has an input torque of 100–150 N m and an output torque of 500–600 N m. With a single jumbolter match, the maximum torque magnification is approximately six times, which meets the high prestressing requirement of the bolts.

## 5.6 Stress characteristics of the surrounding rock in a full seam roadway and numerical simulation of the combined support with bolt and cable

In order to better understand the distribution characteristics of variation of surrounding rock in a large cross-section full coal roadway, as well as the support mechanism and main effect factors of anchor bolts and cables, a numerical analysis using $FLAC^{3D}$ was performed based on the data from the No. 5105 return airway of the No. 8105 coalface at Tashan coal mine The stress characteristics of the surrounding rock in a large cross-section coal roadway with different top coal thicknesses, the influence of different roadway layout locations, different roadway width-height ratios, different ground stresses, and different pre-tight forces of anchor bolts and cables were evaluated.

### *5.6.1 Simulation approach*

The No. 5105 return air roadway was developed along the seam floor, its cross-section is in a rectangular shape with a width of 5.5 m, a height of 3.9 m. Ground stress data measured are shown in Table 2, vertical stress is 11.44 MPa, the maximum horizontal principal stress is 12.90 MPa, and the minimum horizontal principal stress is 7.24 MPa.

In the numerical simulation, the $FLAC^{3D}$ built-in cable structure element was used to simulate the rock bolts and cables. The bolts have anelastic modulus of 200 GPa, a yield strength of 600 MPa, a tensile strength of 800 MPa. The rock bolts are 2.4 m long and 22 mm in diameter. The cables have an elastic modulus of 195 GPa a length of 8.3 m, a diameter of mm, and a capacity of 600 kN. The Mohr–Coulomb constitutive model was used to describe the coal-rock body. Based on the results from the laboratory tests, the physical and mechanical parameters of coal and rock seams in the calculation are shown in Table 25.

Combining the geological conditions at the No. 5105 roadway in Tashan coal mine, based on the combined support of ancho bolts and anchor cables in coal roadway, multiple plans were compared in the simulations in this study:

(1) When the horizontal principal stress is 12.90 MPa, the vertical stress is 11.44 MPa, and the roadway was developed along the seam floor, the effect of different top-coal thicknesses on the stress distribution of the surrounding rock. Top-coal thicknesses were 0, 5, 10, 15, 20, and 25 m respectively.

(2) When the horizontal principal stress is 12.90 MPa, the vertical stress is 11.44 MPa, and the coal thickness is 15.72 m, the effect of different positions of the roadway layout on the stress distribution of

**Table 26** Different ground stress combinations in the numerical simulation

| Different ground stress combinations | Horizontal stress (MPa) | Vertical stress (MPa) | Lateral pressure coefficient |
|---|---|---|---|
| Combination 1 | 10 | 10 | 1 |
| Combination 2 | 20 | 10 | 2 |
| Combination 3 | 10 | 20 | 0.5 |

surrounding rock. In a vertical direction, the roadway was laid out along the roof and along the floor. When the coal-pillar widths in the horizontal direction were 10, 20, 30, and 40 m, the effect after the extraction of two adjacent coalfaces on the stress distribution of surrounding rock of roadway.

(3) When the horizontal principal stress is 12.90 MPa, and the vertical stress is 11.44 MPa, the effect of different width-height ratios on the stress distribution of the surrounding rock of the roadway. The height-width ratios in a full coal seam gateway are 1, 0.75 and 0.5.

(4) When the coal thickness is 16.8 m, the roadway was developed along the seam floor, the effect of different ground stresses on the stress distribution of the surrounding rock of the roadway. Different combinations of stress are shown in Table 26.

(5) The effect of different preloads of bolts and cables on the spread of stress in coal (regardless of in situ rock stress). Under the condition of the cable's prestress as 100, 150, and 200 kN, the bolt preloads are 60, 80 and 100 kN, respectively.

### 5.6.2 *Effect of top-coal thickness on the stress distribution of surrounding rock of full coal roadway*

In Fig. 57a, because the roadway's roof and floor are rock, and the two walls are coal, the stress concentration zones after roadway development are located at the four corners of the roadway in the roof and floor rock strata, the maximum compressed stress reaches 22 MPa. As the rock strengths of roof and floor are relative high, it enables pressure to be uniformly transferred to the coal wall bodies of the roadway to reduce the compressed stress in the coal bodies of the roadway's two sides, and reduce roadway deformation. As shown from Fig. 57b–f, with the increase of top coal thickness, the distribution zone of compressed stress in top-coal increases, and the stress in top-coal is less than that in the roadway floor. There is a distinct interface between top-coal and roof. Overall, during roadway excavation, when top-coal thickness is within 10 m, there is a strong correlation between the stress distribution of surrounding rock of roadway and the top-coal thickness. As the top-coal thickness increased, the stress concentration area in the top-coal expanded and the concentration coefficient reduced. With the continual increase of top-coal thickness, there is no appreciable variation in stress distribution of the surrounding rock.

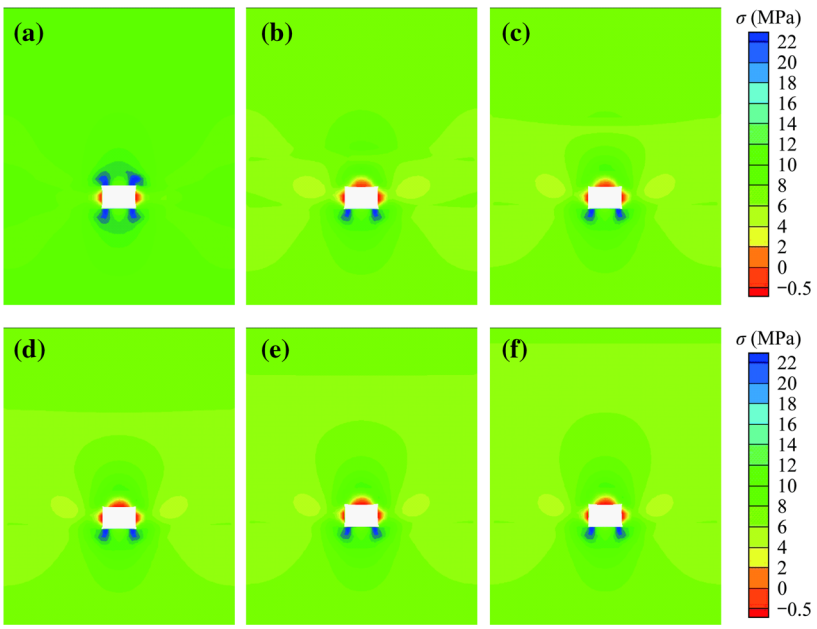


**Fig. 57** Stress distribution of roadway surrounding rock at different top-coal thicknesses. **a** Rock roof **b** top coal 5 m **c** top coal 10 m **d** top coal 15 m **e** top coal 20 m **f** top coal 25 m

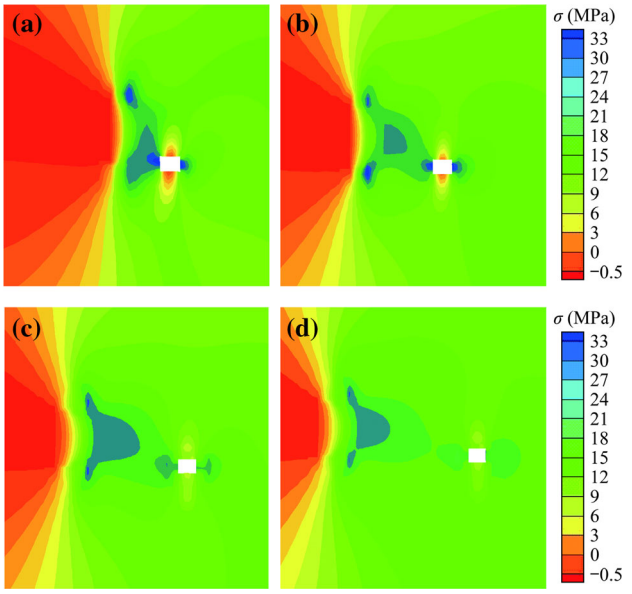


**Fig. 58** Stress distribution of roadway surrounding rock with different coal pillar widths. **a** Coal pillar width 10 m **b** coal pillar width 20 m **c** coal pillar width 30 m **d** coal pillar width 40 m

### 5.6.3 *Effect of roadway layout positions on the stress distribution of surrounding rock of full coal roadway*

The coalface with full coal roadways is usually a coalface with a large mining height. The increase of mining height will have a great impact on the stress distribution in the coal pillar, thus affecting the stress distribution of surrounding rock of the roadway. In Fig. 58a, b, the stress concentration zone generated at two side walls during roadway development overlapped with the stress concentration zone in coal pillar after coal extraction. The maximum stress in the coal pillar reaches 33 MPa. In Fig. 58c, the stress concentration zone in the surrounding rock of roadway during its development is isolated from the stress concentration zone in coal pillars caused by the extraction of two adjacent coalface. However, it still has some impact on the stress distribution of the surrounding rock of the roadway, the maximum compressive stress on the side coal pillar is approximately 30 MPa. In Fig. 58d, due to the further increase of coal pillar width, the effect of the stress of the adjacent mining face on roadway decreased significantly. The stress concentration zone formed in the surrounding rocks of the roadway during its development is basically separated with the stress concentration zone formed by coalface extraction. The maximum compressive stress of surrounding rocks of the roadway is 27 MPa. Overall, due to the large thickness of coal seams with the coal roadway, after roadway development and adjacent coalface extraction, the stress concentration zone formed in the coal pillar is different to that at thick or thin coal seams. The stress is no longer distributed as standard

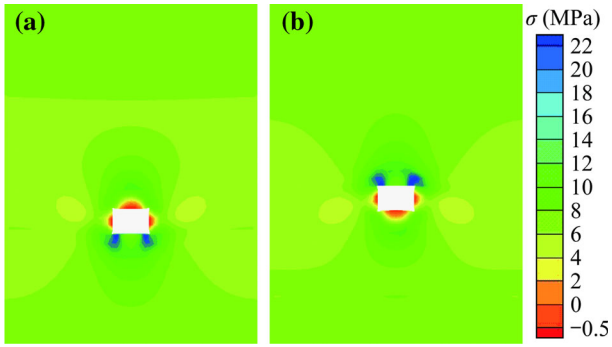


**Fig. 59** Stress distribution of surrounding rock with different roadway positions. **a** Along floor layout **b** along roof layout

"arch" or "hump" distribution, but renders approximately triangular distribution.

A full coal seam roadway has two kinds of vertical arrangements, one is arranged along the floor, the other is arranged along the roof, their stress distributions have a large difference (Fig. 59). When the roadway is arranged along the floor, the stress concentration area is mainly distributed in the two corners of the roadway floor, the maximum stress reaches 22 MPa, and the maximum stress in the top coal of roadway is about 18 MPa. When the roadway is arranged along the roof, the stress state of surrounding rock of the roadway is opposite to that of roadway arranged along the floor, the stress concentration area is mainly distributed on the two corners of the roof, maximum stress is 22 MPa, and the maximum stress of the coal body at the floor is about 18 MPa. Because the stress field distributions of two kinds of arrangements are different, different measures should be taken during the roadway support. When the roadway is arranged along the floor, in addition to the top-coal support, the side walls support should be enhanced or the anchor bolt should be installed at the floor corners to prevent the occurrence of floor heave. When roadway is arranged along the roof, the support on the two corners of the roof should be strengthened, and some measures should be taken to prevent or reduce the occurrence of floor heave.

### 5.6.4 *Effect of roadway height-width ratio on stress distribution of a full coal roadway*

The stress distributions of the surrounding rock of the roadway under different roadway height-width ratios are shown in Fig. 60. With the same roadway height, the wider the roadway tunnel is, the higher the level of stress concentration in the top-coal; the greater the stress concentration area in top-coal, the higher the stress concentration factor. When the roadway's height-width ratio is equal to one, the maximum compressive stress in top-coal is

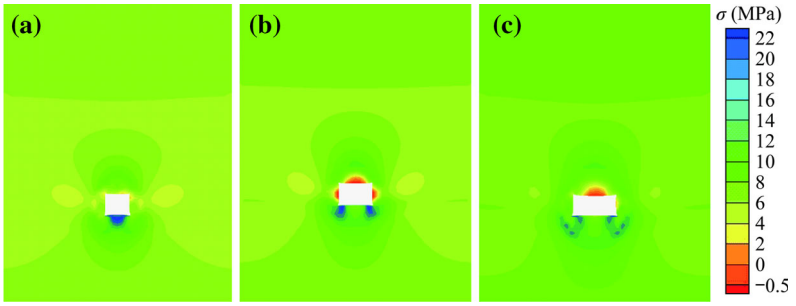


**Fig. 60** Stress distribution with different roadway's height-width ratios. **a** Height-width ratio 1 **b** height-width ratio 0.75 **c** height-width ratio 0.5

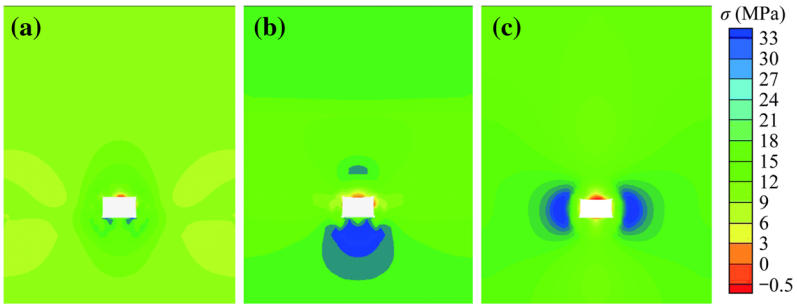


**Fig. 61** Stress distribution of surrounding rock with different ground stress. **a** Combination 1 **b** combination 2 **c** combination 3

12 MPa. When roadway's height-width ratio is 0.75, the maximum compressive stress in top-coal is 16 MPa. When roadway's height-width ratio is 0.75, the maximum compressive stress in top-coal is 16 MPa, but the compressive stress concentration area increases significantly. When the roadway's height-width ratios are different, the stress distributions formed in the floor during roadway development are significantly different. When the height-width ratio is equal to one, the stress concentration zone in the floor shows an "inverted arch" distribution. When the height-width ratio is 0.75, the stress distribution zone shows an "inverted hump" shape distribution. When the height-width ratio is 0.5, an irregular stress distribution in the floor occurs, but the range increases significantly. Based on the maximum stress values in the floor, with the increase in roadway's width, the maximum stress values follow a downward trend.

#### *5.6.5 Effect of ground stress on stress distribution of surrounding rock of a full coal roadway*

The stress field distributions of surrounding rock of a full coal roadway under different ground stress conditions are shown in Fig. 61. The stress distribution of the surrounding rock of the roadway after roadway development is correlated to rock strength. When the horizontal and vertical stresses are the same, the stresses in the top-coal and side coal walls are basically the same, their values are relatively low, about 15 MPa. High stress areas are mainly in the floor with high rock strength, the maximum stress is about 21 MPa. When the horizontal stress is twice of vertical stress, the stress concentration areas are mainly in the top coal and the floor rock. In particular, due to the high rock strength in the floor, its stress and stress concentration area are significantly larger than that in top coal, the maximum stress value is up to 33 MPa. When the vertical stress is twice of horizontal stress, the maximum compressive stress of surrounding rock of roadway is approximately 30 MPa, and the stress concentration area shows an arc-shaped symmetrical distribution at two side walls of the roadway.

#### *5.6.6 Effect of different bolt prestress on the stress distribution of surrounding rock of a full coal roadway*

The increase of compressive stress in the anchorage zone and the range extension of compressive stress are the keys to improving the supporting effect. As shown in Fig. 62a, in the anchor bolt and anchor cable joint support, when anchor bolt pre-tight torque is 200 N m, a prestress overlap zone can be formed in the anchor bolt anchorage zone, but cannot cover the area between roof and anchor bolt at two side coal walls. The maximum compressive stress near anchor bolt in the coal body is about for 0.55 MPa, the compressive stress between anchor bolts is approximately 0.25 MPa. When the anchor bolt's pre-tight torque is

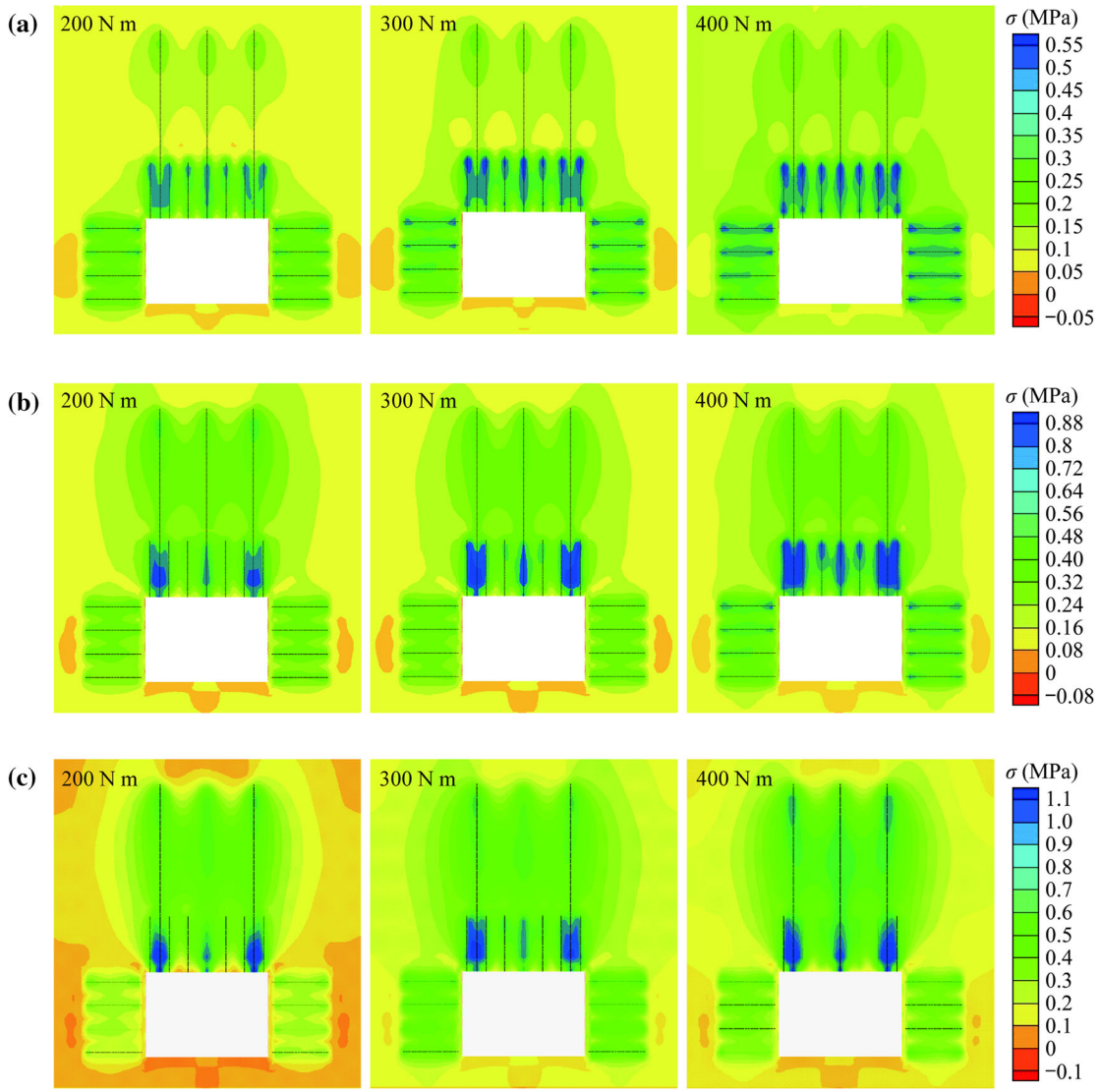


**Fig. 62** Stress distribution of surrounding rock with different combinations of bolt and cable. **a** Cable prestress 100 kN **b** cable prestress 150 kN **c** cable prestress 200 kN

300 N m, with the increase of anchor bolt's pre-tight force, the anchor bolt's prestress spread range increases at roadway roof and two side coal walls, and in roadway's top coal, the spread zones can basically join and form one large zone. However, the anchor bolt's prestress spread zone is still small, and cannot cover the whole coal wall. The compressive stress between top coal and the roadway walls anchor bolt increases to around 0.4 MPa. When bolt's tightening torque increases up to 400 N m, the effect of the bolt's prestress spread within bolting range between the roof and two walls of the roadway is good. It covers the entire range of anchor zone, and the compressive stress value between bolts in the coal increases to about 0.5 MPa. Because of the lower prestress of the anchorage cable, the cable's prestress cannot spread to its anchoring range, thus, the overlapping effect of the bolt's prestress and cable's prestress is not obvious.

Compared to Fig. 62a, b shows that with the increase of the cable's prestress, there is a significant increase of prestress spread in the area along the cable length in the roadway's top coal and perpendicular to the direction of cable length. Nevertheless, in terms of the compressive stress in coal body formed by the bolt and cable's prestress, under the impact of the increase of cable's prestress and the superposition effect of the bolt's prestress, the maximum compressive stress close to the cable in the coal body reaches 0.88 MPa. When the bolt's tightening torque is 200, and 300 N m, the distribution of compressive stress

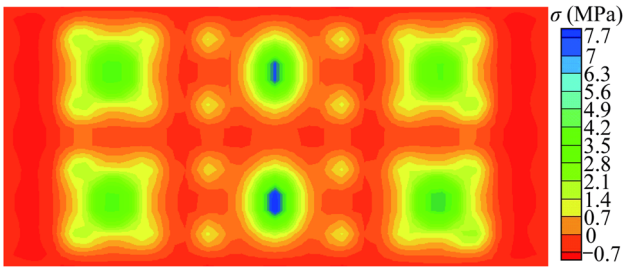


**Fig. 63** Stress distribution on the surface of top coal with the bolt and cable combined support

formed in the coal body by cables and bolts is not uniform, the compressible stress between two bolts farther away from cables is 0.48 MPa. When the bolt's tightening torque is 400 N m, the effect of prestress spread formed in top coal by cables and bolts is improved to some extent. The compressible stress between two bolts farther away from cables is approximately 0.64 MPa.

As shown in Fig. 62c, when the cable's pre-tight force increases to 200 kN, the cable plays a major role in prestress spread in the coal body, the range of prestress spread basically covers the entire cable anchoring zone, and the maximum compressive stress formed in coal body is 1.1 MPa. The bolt's pre-tight force mainly affects the compressive stress distribution in the coal body, as the increase of bolt tightening torque, there is a distinct increase of compressive stress spread formed in the coal body and the stress values.

Figure 63 shows the compressive stress distribution on the surface of the roadway under the support of the combination of rock bolts and cables with a pre-tightening force of 400 and 150 kN, respectively. The compressive stress zones on the roadway surface formed by bolts and cables' combined support are interconnected and superimposed. The compressive stress of top coal at the bolt tray reached 2.8 MPa, at cable tray reached 7.7 MPa, the bolt's prestress and cable's prestress basically spread to the entire surface of top coal to form an effective stress arch, and improve the stress state of the surrounding rock of the roadway.

### 5.7 Support design of a large cross-section full coal roadway

Based on the numerical simulation results and lessons learned, a high strength bolt and cable combined support system was determined for the No. 5105 roadway at the No. 8105 coalface in Tashan coal mine. A BHRB600 bolt was selected with a diameter of 22 mm and length of 2.4 m left-lateral no longitudinal reinforcement steel rebar, extended with resin, and the bolt's tightening torque is not less than 400 N m. A 4 mm thick W steel belt and

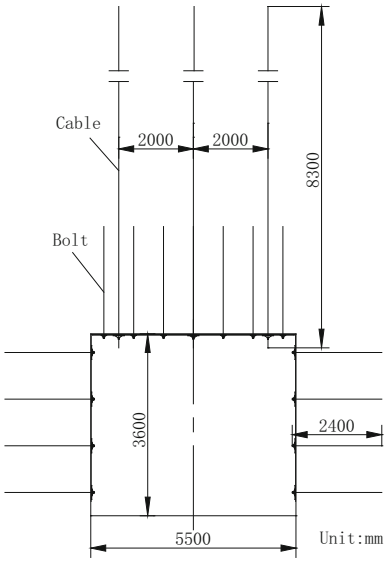


**Fig. 64** Layout of roadway support

diamond-shaped metal mesh were used to protect the roof and side walls of the roadway. The roof bolt spacing was 800 mm, and the row spacing was 800 mm. Roof cable's diameter was $\phi$22 mm with 1 × 19 strands high strength low relaxation prestressed steel wires, and its length is 8300 mm. Using one K2335 and two Z2360 low viscosity resin cartridge, the cable was anchored, the anchorage length is 1500 mm. With every two rows of bolts, three cable anchors were installed, the row spacing is 1600 mm, and cable spacing is 2000 mm, and all cables were vertically installed into the roof. The cable anchor's pre-tightening force was 100–150 kN. Figure 64 shows the layout of roadway support.

## 6 Safety technologies for the LLTCC coal mining operation

### 6.1 Gas control technologies for the LLTCC coalface

#### *6.1.1 Characteristics of gas distribution at the LLTCC coalface*

At the coal seam 3–5 in Tashan coal mine, the original gas pressure varies 0.14–0.17 MPa, the gas content in the coal seam varies 1.60–1.97 $m^3$/t and the average is 1.78 $m^3$/t. The coal seam permeability coefficient varies 171.71–428.80 $m^2$/(MPa$^2$ d), and the gas flow per hundred meters in the borehole varies 0.015–0.0212 ($m^3$/min hm); the gas discharge attenuation coefficient in the borehole varies between 0.602 and 0.7427 $d^{-1}$. The residual coal gas amount at the coal seam 3–5 is 1.17 $m^3$/t. The coal seams

are spontaneous combustion-prone coal seams, and the shortest period of the occurrence of spontaneous combustion is 60 days; the coal seams have a tendency for coal dust explosion hazards and the explosion index is 37 %.

With the analysis of field tests, the gas emission and distribution in a LLTCC coalface have four characteristics:

(1) Low gas storage, high gas emission. Under the influence of large thickness of coal seam and high mining intensity, the LLTCC mining operation in ultra-thick coal seam shows a "low gas storage, high absolute gas emission" feature. At the coal seam 3-5, the original gas pressure was only 0.14–0.17 MPa, gas content in the coal seam was 1.6–1.97 $m^3$/t, and an average was only 1.78 $m^3$/t, however, the absolute gas emissions in the working face exceeded 40 $m^3$/min, and the highest absolute gas emission was up to 65 $m^3$/min.

(2) Unbalanced gas emission. The gas emission sources at the LLTCC coalface in Tashan mine can be divided into three parts, one is the gas at the top position of the goaf including the gas in the upper adjacent layer; the second is the gas in the deep part of the goaf including the gas of the lower adjacent layer; the third is the gas from coal extraction and caving operation carried by the airflow leakage in the working face. The gas emission in the three sources discussed above will be affected by face pressure, upper roof caving and top coal caving, and present the characteristics of imbalance, and the uneven emission coefficient might reach 1.8.

(3) Large gas emission in goaf. Local gas emission in goaf showed that the gas emission often exceeded the gas limit at the zone between the 110th support and upper corner of the coalface; at the window of top coal caving and the gap between supports, the measured gas concentration reached 2 %–3 %, sometimes even higher. At U-type ventilation coalface, the gas concentration seriously exceeded the gas limit in the upper corner of the working face. Without taking any measures in the upper corner, the gas emission concentration often exceeded 5 %. In the 10 % tail region of the coalface, the gas emission accounted for 90 % of the gas emission.

(4) The gas concentration distribution in the coalface showed a nonlinear relationship with the distance from the monitoring station. Figure 65 shows the gas concentration distribution along the vertical direction and face advance direction at the LLTCC coalface. The gas concentration distribution on the vertical face in the goaf showed an increase trend from bottom to top, increasing 2.3 % every 5 m;

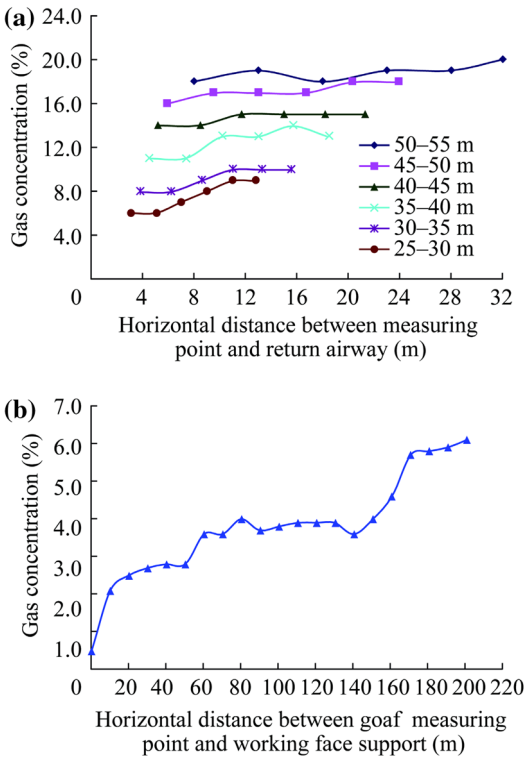


**Fig. 65** Gas concentration distribution along the directions of vertical height in the goaf and face advance. **a** Along the direction of roof height **b** along the direction of face advance

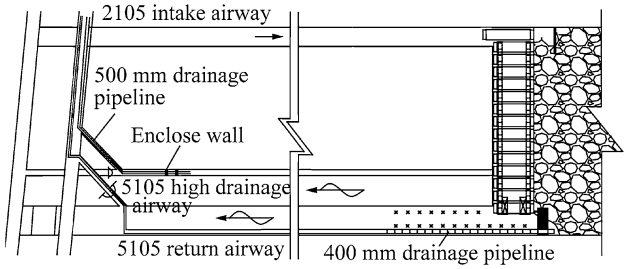


**Fig. 66** Gas drainage at the No. 8105 working face

From the tailgate to internal displacement 32 m, the gas distribution showed an increasing trendency within the same elevation. From the support at the working face to the deep goaf, and within a 200 m range, the gas concentration distribution showed a ladder-type distribution. Within a 0–60 m range from the support to the goaf, the gas concentration increased from 1.5 % to 2.8 %; within a 60–160 m range in the goaf, the gas concentration increased from 3.6 % to 4.6 %; within a 160–200 m range in the goaf, the gas concentration increased from 5.7 % to 6.1 %, and basically coincided with the spontaneous combustion "three-zone".

**Fig. 67** Nitrogen generator in making

**Fig. 68** Nitrogen generator in assembling

**Fig. 69** Nitrogen generator after assembly

**Fig. 70** Nitrogen generator at site test

#### *6.1.2 Gas control technologies at the LLTCC coalface*

Based on the characteristics of gas occurrence, a "mainly in strengthening gas drainage in goaf, complemented with the optimization of ventilation system in the working face" approach was used to develop a gas drainage roadway in roof-based comprehensive control technology for the LLTCC coalface. A three-step integrated program was developed: the first step was to use seals to block the gas at the upper and lower corners, and wind curtains to induce and dilute the gas for controlling the gas limit at the upper corner of the coalface at the early mining stage; the second step was to establish a large flow gas drainage system, including high-position pre-buried vertical tube, upper corner drainage tube and coalface ventilation system optimization; the third step was to developed a high drainage roadway in the roof, and use the closed roof high drainage roadway to drain the gas in the goaf. The gas drainage and mining at the No. 8105 coalface in Tashan coal mine is shown in Fig. 66.

### 6.2 Fire prevention technologies for LLTCC coalface

#### *6.2.1 Large flow mobile nitrogen generator mounted on rubber tire vehicle underground*

The nitrogen injection method was used to prevent fire at LLTCC coalface in ultra-thick coal seams. Therefore, a large flow mobile nitrogen generator mounted on rubber tire vehicle in the underground was developed. Figures 67, 68 and 69 show the units of large flow pressure swing adsorption nitrogen generator in the manufacturing process. Figure 70 shows the nitrogen plant in a field test.

The large flow mobile nitrogen generator mounted on rubber tire vehicle has following technical characteristics:

(1) Comparing and taking from the coarse and fine particle combined adsorption tower filling method in the US, the same method in Europe, the "blizzard" type adsorption tower absorption method, and the vibration desktop type filling method were used to develop a carbon molecular sieve filling method with the combination of vibration desktop type filling and coarse and fine grain filling, which greatly improved the service life of the molecular sieve;

(2) The recirculation calculation formula of minimum industrial pressure swing adsorption tower $\omega_2$ (minimum) $\approx 1.15\omega_0(t_a/t_p)(p_3/P_0)$ was used to replace the calculation formula of the minimum regeneration cleaning amount required by the continuous adsorption process $\omega_2$ (minimum) $\approx \omega_0(t_a/t_p)(p_{j0}/P_{j3})(-p_{j3} - P_{j3})/p_0$ ($\omega_2$ is the Minimum cleaning quality flow rate of regeneration, kg/s; $\omega_0$ is the initial gas mass flow rate, kg/s; $t_a$ is the limiting adsorption time, s; $t_p$ is the holding regeneration time, s; $p_3$ is the export airflow pressure, Pa; $p_0$ is the initial pressure entrance airflow, Pa), thus, the minimum amount of regeneration recirculation was determined. Combined with the control recirculation valve of the PLC controller, by reverse blowing

with the inlet direction, the fast and high efficient generation of nitrogen with the carbon molecular sieve device was achieved to increase the nitrogen amount generated by the nitrogen generator, as well as the nitrogen purity. In addition, it was possible to reduce the size of the nitrogen generator, and make the nitrogen generator more in line with the underground environment;

(3) The activated carbon filtering method was used with the combination of C, T and A three-stage fine filtrations. The activated carbon was used to remove large particles of water and oil in the compressed air, to prevent the absorption and break by the carbon molecular sieve. Using C, T, and A three-stage fine filtrations, the particles of water, oil and dust greater than 0.1 μm in compressed air will be removed to avoid large particle impurities not deposing to adsorption bed, reduce the adsorption bed resistance except maintaining the service life of the adsorbent. Furthermore, the nitrogen generator can work in a high nitrogen purity situation for a long time, ensuring that the molecular sieve service life can be extended and the efficiency of carbon molecular sieve can be improved;

(4) A dual PLC control automatic control system was developed. With the control of a dual control system, the unstable system problem caused by the interference of variable-pressure absorption in the same of twin towers was avoided during the operation of the four adsorption towers.

#### 6.2.2 *Study on the process and properties of large flow nitrogen generator*

With a full consideration of the speed effect of the pressure swing adsorption tower, the size effect of adsorption bed and the adsorption equilibrium of carbon molecular sieve, the pressure swing adsorption tower was designed and the tower was filled with the vibration bench filling method and the coarse–fine combination filling method. Selecting the suitable pressure swing adsorption process, through a control system, the pressure swing adsorption nitrogen-making process was controlled, to ensure the time of pressure swing adsorption, and the time of adsorbent regeneration. Using product gas reverse blowing regeneration technologies, the nitrogen generation capacity of pressure swing adsorption and nitrogen purity were improved, and the nitrogen purity reached the requirement of $\geq$98 %. With the methods of activated carbon filters, and C, T and A three-stage fine filtration, the particles of water, oil and dust greater than 0.1 μm in compressed air was removed to ensure the service life of the adsorbent while reducing the adsorption bed resistance, and maintain the generation of high purity nitrogen.

Based on research and the comparison on the method of other existing models of pressure swing absorption molecular sieve nitrogen generator, through a small scale laboratory test, a comparison on the different processes, different adsorption media was conducted to determine the best process. The process is as follows: air compression—air buffer (and preliminary water removal)—activated carbon filter (removal of most of the water, and oil in compressed air)—fine filter (removal of the particles of water, and oil and dust greater than 0.1 μm in compressed air in)—pressurized adsorption (nitrogen generation)—pressure release—even pressure regeneration (reverse blowing process)—product nitrogen. In the compressed air system, two 250 kW screw-type air compressors were used to compress air, and the two sets of PLC controllers were used to control the pressure swing adsorption process. They ensure the smooth completion of adsorption and desorption process of the pressure swing adsorption nitrogen generating apparatus. After a 24 h continuous operation test, with the condition of nitrogen purity was greater than 98 %, the nitrogen flow rate was greater than 2000 $m^3$/h.

#### 6.2.3 *Development of fast curing stackable sealing material*

The sealing on the upper corner of the coalface is an effective method for reducing the risk of spontaneous combustion in the goaf. However, in Tashan mine, the cross-section of intake and air return roadways are all up to 20 $m^2$. The use of traditional means, i.e. fly ash and yellow mud, would result in heavy workloads and high cost, which affects the normal transportation in the mine. Therefore, a fast curing stackable sealing material was developed.

Fast curing stackable sealing material is a polymer composite with multi-component, multi-usage, and solid gel combination, and is composed of a polymer compound, foaming agents, catalysts, flame retardants and other components. The feeding sequence for making the sealing material is: A material → B material → water-cement-sand mixture → curing agent. At the same time, the sealing material was quickly mixed to a uniform status, then pressurized and sprayed. The volume of the sealing material would instantly expand to (10–30) times of its original volume to achieve fast sealing. This material does not contain formaldehyde, is nontoxic, odorless, and non-corrosive. During the reaction expansion process, the sealing material can fill the space and cracks in coal and rock, and has a strong bonding property. It can bond coal (rock) body, concrete, and other materials to form one solid body. It has a certain level of pressure resistance and shear

**Table 27** Equipment for the coalface

| No. | Equipment name | Main parameters of equipment | Reference type |
|---|---|---|---|
| 1 | Hydraulic support | Height:2800–5200 mm; center distance: 1750 mm; support intensity: >1.35 MPa | ZF15000/28/52 |
| 2 | Shearer | Cutting power: 2 × 750 kW; cutting height: 2.7–5.0 m; cutting depth: 800 mm; AC electric traction; voltage: 3300 V | MG750/1915-GWD |
| 3 | Front scraper conveyor | Length: 220 m; power: 2 × 855 kW; voltage: 3300 V; transportation capacity: 2500 t/h | SGZ1000/2 × 855 |
| 4 | Rear scraper conveyor | Length:220 m; power:2 × 1000 kW; voltage: 3300 V; transportation capacity: 3000 t/h | SGZ1200/2 × 1000 |
| 4 | Stage loader | Transportation capacity: 3500 t/h; power: 450 kW; voltage: 3300 V | PF6/1542 |
| 5 | Crasher | Crashing capacity: 4250 t/h; power: 400 kW;voltage: 3300 V | SK1118 |
| 6 | Emulsion pump | Working pressure: 31.5 MPa, Rated flow rate: 400 L/min; motor power: 250 kW, voltage: 3300 V, fluid box: 2, volume: 2500 L | BRW400/31.5 |
| 7 | Spray pump | Working pressure: 12.5 MPa, Rated flow rate: 500 L/min,motor power: 132 kW, voltage: 3300 V, fluid box: 1,volume: 3000 L | BPW500/12.5 |

**Fig. 71** Combined trial operation on the surface of complete equipment for the working face

resistance strength. It has good flexibility, is shockproof and pressure resistant, has strong elastic resilience after compression, with no cracking after curing, and no shedding. It has insulation properties, including heat insulation and flame retardant properties, suitable for filling at different locations in an underground coal mine.

The response time of rapid curing stackable material is 5–60 s adjustable at (23 ± 2) °C. The foam index is 10–30 times adjustable. The flame retardant: oxygen index is not less than 32, vertical and horizontal combustion level is V0. The content of heavy metals (Pb) is less than 0.90 mg/kg (assessment value 90 mg/kg).

## 7 Test in underground coal mine and result analysis

### 7.1 Parameters of working face and equipment

At the No. 8105 LLTCC coalface in Tashan coal mine, the face length is 207 m, the maximum cutting height is 5.0 m, and the cutting depth is 0.8 m. The installed capacity for the working face is 10 Mtpa. Based on the technical parameters and performance of fully mechanized coal mining equipment in China, the main technical parameters of the fully mechanized coalface equipment are determined as shown in Table 27.

In April 2010, the combined trial operation on surface of the complete equipment developed was conducted at Tashan coalmine (Fig. 71). From October to December in the same year, an underground industrial trial was completed.

### 7.2 Operation of trial equipment and production

During the period of the industrial trial at the No. 8105 face from October to December 2010, the statistics of production downtime caused by major equipment accidents are shown in Table 28. From October to December 2010, the

**Table 28** Statistics of production downtime caused by major equipment failure during the industrial trial period from October to December 2010

| Time | Shearer | Hydraulic support | Scraper conveyor | Belt conveyor | Power supply system |
|---|---|---|---|---|---|
| October 2010 | 22 h 35 min | 0 | 0 | 8 h 30 min | 2 h 35 min |
| November 2010 | 4 h | 0 | 15 h 50 min | 5 h 10 min | 4 h |
| December 2010 | 4 h 30 min | 0 | 1 h 25 min | 15 min | 0 |
| Total | 31 h 5 min | 0 | 17 h 15 min | 13 h 55 min | 6 h 35 min |

**Table 29** Production statistics at No. 8105 coalface during the industrial test period from October to December 2010

| Time | Number of working days | Cutting height average/maximum (m) | Face advance (m) | Production (t) | Average/maximum monthly production (t) | Average daily production (t) | Average manpower efficiency (t/worker) | Coal recovery (%) | Equipment usage (%) |
|---|---|---|---|---|---|---|---|---|---|
| October 2010 | 30 | 4.5/5.0 | 147.75 | 901,732 | 907527/916785 | 30057.8 | 362.2 | 88.9 | 92.1 |
| November 2010 | 30 | | 152.25 | 904,065 | | 30135.5 | 363 | | |
| December 2010 | 30 | | 172.5 | 916,785 | | 30559.5 | 368.2 | | |
| Total | 90 | 4.5/5.0 | 472.5 | 2,722,582 | 907527/916785 | 30250.9 | 364.5 | 88.9 | 92.1 |

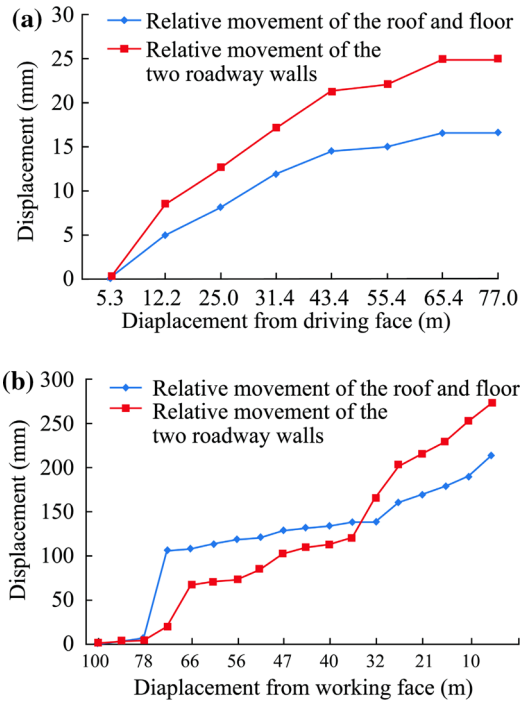


**Fig. 72** Displacement curve of the roadway surface. **a** During roadway development **b** during coalface operation

production downtime caused by shearer accidents was 31 h and 5 min, the shearer usage rate was 98.45 %, and its performance was stable. The production downtime caused by hydraulic support failure was zero, its working resistance varied within a 9000–13,000 kN range, and overall the support was in good condition. The production downtime caused by scraper conveyor failure was 17 h and 15 min with an usage rate of 98.95 %. The production downtime caused by belt conveyor accidents was 13 h and 55 min, with an usage rate of 99.15 %. The production downtime caused by power system accident was 6 h and 35 min, failure-free rate was 99.61 %.

In October 2010, the production downtime caused by cumulative electrical accidents during the production period was about 57 h and 40 min. Based on four shifts with six hours each shift in the working face, the usage rate was 89.3 %. In November 2010, the production downtime caused by cumulative electrical accidents during the production period was about 53 h and 50 min, the usage rate was 91.3 %. In December 2010, the production downtime caused by cumulative electrical accidents during the production period was about 7 h and 10 min, the usage rate was 95.7 %. In the industrial test period from October 2010 to December 2011, average usage rate of equipment in use was 92.1 %.

During the industrial test period from October to December 2010 at No. 8105 coalface, the cumulative face advance was 472.5 m, average daily advance was 5 m,

**Fig. 73** Roadway support at the No. 5105 roadway

maximum daily advance was 8 m; the cumulative coal production was 2.723 Mt, the average daily production was 30,300 t, maximum daily production was 38,000 t; average manpower efficiency was 364.5 t/worker. In three consecutive months during the industrial test, average monthly production reached more than 900,000 t, coal recovery rate at the working face reached 89.9 %. In 2011, the average monthly coal production was 904,000 t, the cumulative coal production for the year was 10.849 mt, achieving the goal of producing 10 Mtpa. The production statistics for the industrial test at the No. 8105 coalface from October to December 2010 is listed in Table 29.

### 7.3 Analysis of roadway support

During the excavation and support in the No. 5105 roadway, the deformation of the surrounding rock of the roadway was monitored, see Fig. 72a. The wall-to-wall convergence and the roof-to-floor convergence during the roadway excavation period was 25 mm and 16.6 mm, respectively. The support effect during the excavation period is shown in Fig. 73. In general, the deformation was small during roadway excavation period, and the effect of roadway support was good.

After the coal extraction at the No. 8105 coalface, under the influence of coal extraction, there were some variations in stress distribution of the surrounding rock in the roadway. The stress concentration occurred in coal and rock body in front of the coalface and in the surrounding rock of the roadway, resulting in the deformation of surrounding rocks in the roadway. The roadway surface displacement was monitored in the No. 5105 roadway within a 100 m range in front of the No. 8105 coalface, the monitoring results are shown in Fig. 72b. As can be seen from the figure, there was no change for the roadway surface displacement exceeding 78 m from the coalface, the roadway deformation affected by the coalface abutment pressure appeared from a location 78 m in front of the coalface. Within 78–66 m range in front of the coalface, large deformations occurred at the same time in the roof and two

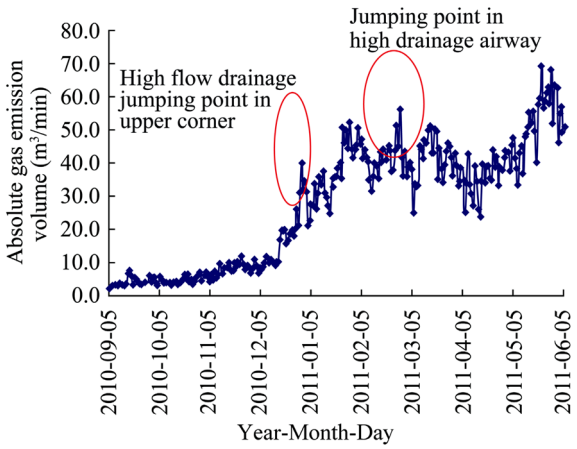


**Fig. 74** Monitoring curve of absolute gas emission volume

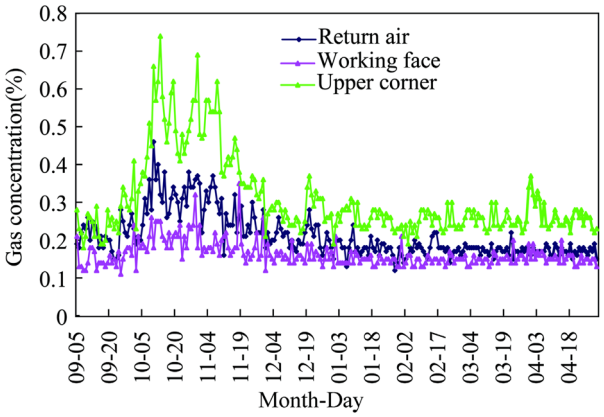


**Fig. 75** Variation curves of gas concentration at the upper corner of coalface, coalface and in return air after coal extraction

walls. Subsequently, the deformation increased as the coalface advanced slowly. Within 36 m range from coalface, with the advance of the coalface, the deformation began to dramatically increase. In the location of the monitoring station 5 m away from the coalface, the two side walls of the roadway moved closer by 280 mm, the roof and floor closer by 210 mm. However, in general there was no obvious damage to the surrounding rock of the roadway during the coal extraction period, the amount of deformation was small, and the transportation and ventilation requirements was fully able to be met.

### 7.4 Analysis on gas control

On the 9th of November 2010, the No. 8105 coalface and roof drainage roadway were connected. After the connection, a 2BEC80 gas drainage pump was used to drain the gas, the gas concentrations were maintained between 1.5 %

and 2.2 % in the high drainage roadway, between 0.2 % and 0.3 % at the upper corner of working face, between 0.2 % and 0.3 % at the tail of the rear scraper conveyor, and between 0.15 % and 0.25 % in the return air. Thus, the gas management at the coalface achieved very good results.

The gas emissions at the coalface were monitored before the coalface extraction, from coalface extraction to the initial caving of the upper roof, to first gas drainage at the upper corner of coalface, during the gas drainage at the upper corner of coalface, and from the gas drainage at the upper corner of the coalface to the gas drainage in return airway and high drainage roadway. The monitoring curve of absolute gas emission volumes are shown in Fig. 74.

Figure 75 shows the gas concentration variations at the upper corner of the coalface, the coalface and in the return air since the extraction of the No. 8105 coalface. As can be seen from the diagram, coalface gas emission rates gradually increased, the volume of gas drainage increased, while the gas concentration at the upper corner of the coalface, in the coalface and the return air gradually leveled off, and achieved a zero gas overlimit.

Site monitoring results showed that: the technology of roof high roadway drainage combined with other drainage can significantly reduce the gas concentration at the return air corner of the goaf, control the gas emission from the goaf to the coalface, play a role of "split-flow" of gas flow, and reduce the gas concentration in the goaf. The effect for preventing the gas accumulation at the upper corner of the coalface was significant. The drainage rate in the goaf reached 40 % of total gas emission in the goaf, achieving a zero overlimit, and ensuring a safe and smooth face advance. The gas control achieved a satisfactory result.

### 7.5 Analysis on fire prevention using nitrogen injection

Based on air quantity tests at different measuring points in the coalface, the amount of air leakage in the goaf was determined. With the installation of a bundle tube in the goaf and the connection of the bundle tube in the goaf with the main bundle tube monitoring system in the mine, the gas in the goaf was analyzed automatically. In addition, the airflow in the goaf was simulated in 3D to analyses the oxygen concentration in the goaf. Thus, a "three-zone" distribution was found in the goaf. Based on the finding, the nitrogen injection method and the amount of nitrogen injection were given at different face advance speeds.

Based on the actual mining conditions at the No. 8105 LLTCC coalface in Tashan mine, the nitrogen injection parameters were optimized, and the relevant nitrogen injection process and methods were developed. After calculation, an additional 3890 $m^3$/h nitrogen injection was required in addition to original 2500 $m^3$/h, to enable oxygen concentration at the spontaneous combustion zone to drop to an average of 7 %. Pipe nitrogen injection technology was used for fire prevention. The first nitrogen injection pipe along the goaf at the intake side of the coalface was buried. When the pipe was buried at a certain depth into the goaf, nitrogen injection commenced. Subsequently, a second nitrogen pipe was buried into the goaf (the shift interval of the nitrogen injection nozzle was 50 m). When the second nitrogen injection pipe was buried and started nitrogen injection into the spontaneous combustion zone in the goaf, the first pipeline of nitrogen injection stopped, and a new pipe was buried again for nitrogen injection. The process was repeated until the coalface extraction was completed.

The nitrogen injection method was determined based on fire prediction, in the case of nitrogen injection quantity of 2500 $m^3$/h, and coalface advance speed of 1.4 m/d, a continuous nitrogen injection method must be used. When the advance speed is less than 1.4 m/d or if the coalface has stopped, the amount of nitrogen injection must be increased. When the coalface has stopped working for more than 68 days, the nitrogen injection quantity should be not less than 6390 $m^3$/h; when the face advance speed is greater than 1.4 m/d, it would be appropriate to reduce the amount of nitrogen injection. Using the methods presented above, the occurrence of fire in LLTCC coalface can be prevented to achieve safe mining operation.

## 8 Application and benefits

The following problems are present in coal mining in China: one is that the capacity in maintaining safety in mining is relatively low; the second is that technology and equipment, technical management, and the technical innovation level are not at a high level; the third is that the waste of resources is relatively serious; the fourth is that the added-value and technological-content of products are relatively low; the fifth is that the centralization of business is relatively low.

The technologies and equipment for LLTCC coal mining operation in ultra-thick coal seam have achieved a safe and high efficiency extraction of the coal seam with a thickness of 14–20 m. The technologies and equipment developed have effectively increased the coalface production rate and top-coal recovery. The large mining height shock-resistance top-coal caving hydraulic support and the electrohydraulic control technology developed for top-coal caving greatly improved top-coal caving and discharge speed, reduced labor intensity, and increased coalface productivity. The anchor bolt support technology and material developed for the support of large cross-section

full coal roadway significantly improved the effects of roadway support, and ensured the roadway is stable and unblocked. The gas control and fire prevention technology and equipment ensured safe coal production.

After adopting the technology and equipment developed, the investment on equipment in Tashan mine was decreased. Compared to the No. 8104 coalface, the investment on equipment at the No. 8105 coalface saved about 100 million yuan.

With the geological and mining conditions at the No. 8105 coalface, compared to the sub-level caving method in ultra-thick coal seam, the technologies and equipment developed enabled coal production at the No. 8105 coalface in Tashan coal mine to be doubled; the economic benefit is significant.

In addition to the Tashan mine in Datong, currently the LLTCC technologies and equipment for ultra-thick coal seam have been used in 32 coal mines in China, including 13 mining areas such as Datong, Pingshuo, Shengdong, Xinjiang, covering 8 provinces or autonomous regions in China, such as Shanxi, Inner Mongolia, Xinjiang, Shaanxi, Shandong, Gansu, Anhui, Liaoning.

Currently, 14 large coal bases have been planned in China including Shendong, Northern Shaanxi, Huanglong, Northern Shanxi, Jinzhong, Jindong, Luxi, Lianghuai, Jinzhong, Henan, Yungui, Eastern Inner Mongolia (northeast), Ningdong, and Xinjiang, where thick and ultra-thick coal seams are predominantly mined. The main coal seams in the coal mines with 10 Mtpa capacities each currently under construction are mainly thick or ultra-thick coal seams. The coal mines built with a capacity of 10 Mtpa each mainly extract the coal seams with thickness of 6–20 m, the seams above 6 m account for 50 %, such as Halagou, Shigetai, Daliuta, Buliantai, Yujialiang, Shangwan in Shengdong coalfield, Yangchangwan in Ningdong coalfield, Huangling No. 2 mine in Huangling coalfield, Anjialing mine in Pingshuo coalfield, Dafosi mine in Binchang coalfield and Sihe coalmine in Jincheng coalfield. With the construction of large-scale coal production bases in China in the future, LLTCC coal mining technologies and equipment provide technological support for the safe, high efficiency and high recovery coal production in these mines. The technologies and equipment developed will drive the upgrading of existing mechanized caving technology and equipment. The research results will be widely used and the products will have great business potential.

At the same time, the development of technologies and equipment strongly promote the development of coal mining methods and related theories, and lead the progress of coal mining technologies. It enables the capability of manufacturing the complete set of the LLTCC coal mining equipment in China, driving the development of machine processing technology, electromechanical integration technology, and automation and information technology. It curbs the occurrence of roof, gas, and fire accidents, safeguard coal mine practitioners' personal safety, improves underground mine working environment, ensures coal mine safety, efficient, integrated production, improves the efficiency of coal mining and energy supply, and provides reliable energy security for China's sustained, healthy and stable economic development.

## 9 Conclusions

With the study and development of the LLTCC coal mining technologies and equipment for over 10 years, the following main conclusions are obtained:

(1) In terms of coal seams with a thickness of 14–20 m, the LLTCC coal mining method has been proposed, which increases the coal cut height to 5 m, coal caving height to 15 m, and the total mining height to 20 m. The effect of different coal caving intervals and top-coal caving patterns on top-coal recovery has been investigated, which concludes that the recovery rate can be improved in long wall caving by applying the caving patterns of one-cut-one-caving and discharge in multi-round and multiple windows sequence alternately.

(2) A "cantilever beam-articulated beam" model has been established for the overlying strata at the LLTCC coal mining face. Based on the model, the working resistance of the LLTCC hydraulic support has been determined. Furthermore, the law of top coal and roof movement at the LLTCC coalface has been obtained. In front of face coal wall, the main characteristics of top coal and roof movement are mainly horizontal compressive deformation under abutment pressure; in the rear of the face coal wall, the characteristics of roof movement are mainly fractures and subsidence, the characteristics of top coal movement are mainly vertical caving movements caused by roof fractures and subsidence. The speed of horizontal deformation of the top coal and roof in front of the face coal wall under abutment pressure is much smaller than that of the vertical subsidence of the top coal and roof after fracture at the rear of the face coal wall.

(3) Comprehensive spalling prevention and control technologies have been proposed, including controlling the coalface advance speed, increasing the initial support force, and improving the ability of wall protection. These technologies reduce coal wall spalling and maintain the normal advance of the coalface.

(4) A large-diameter double telescopic shock-resistance prop and a 1000 $min^{-1}$ large flow safety valve quick unloading device have been developed, which improve the shock-resistance of hydraulic support; an articulated front beam and high reliable telescopic beam with a secondary wall protection structure have been developed, which overcomes the wall spalling problem at LLTCC coalfaces; and a strong disturbance-type top coal discharge device with high efficiency and high top coal recovery has been developed, which improves coal recovery. On the basis of the developments presented above, a 5.2 m cutting height LLTCC hydraulic support has been developed.

(5) A high efficiency and high reliability electric traction shearer has been developed, its specifications are: coal cutting height 2.8–5.5 m, total installed power 1945 kW, coal cutting power 750 kW, maximum haulage speed 15–25 m/min, and maximum traction force 2 × 570 kN. An analysis method of the shearer reliability has been established. Furthermore, a new control system and walking system for the shearer has been developed, and the new material of ranging arm shell body and the performance of drum tooth have been optimized to improve the reliability of the shearer.

(6) A large-capacity SGZ1200/2 × 1000 rear scraper conveyor has been developed with installed power of 2 × 1000 kW, and transportation capacity of more than 3000 t/h. The transportation distance meets the requirements of the No. 8105 coalface in Tashan mine. In addition, some key accessories, including the heavy-load and high-strength chain transmission system of the scraper conveyor, controllable speed-adjustable soft start device, the integrated monitoring transmission system of transmission device, heavy-load 1000 kW planetary retarder, high-reliability and long-life coal pan, high strength and compact type end unloading headframe, and electrohydraulic control automatic telescopic conveyor tail, have been investigated to improve the performance of the LLTCC rear scraper conveyor.

(7) Various devices have been invented in the project, including a height adjustable ring chain lifting device, a new high efficient air inlet flame arrester and exhaust processing box, and an integrated motor plug type wheel side drive and brake retarder. A WC55Y support hauler with a load of 55 tons has been developed, achieving a safe, high efficiency, non-demolition, "point-to-point" transportation of the LLTCC hydraulic support, and improves the efficiency of LLTCC coalface relocation.

(8) The stress distribution of surrounding rock of large cross-section coal roadway is significantly influenced by the in situ stress and the rock strength. Under the same stress conditions, the higher coal and rock mass strength, the higher the stress magnitude of surrounding rock after the roadway excavation. The support effect of rock bolts on the roadway is mainly to generate compressive stress zones through the prestress force of bolts, and form a prestress loading structure with cables and other supporting structures, thus to strengthen the surrounding rock of the roadway, and constrain the separation, sliding, and opening of fracture in the surrounding rock, and subsequently maintain the integrity and stability of the roadway surrounding rock.

(9) A special bolt steel formula has been developed, which changes the steel mechanical properties. With suitable rolling method, a high strength (500–600 MPa), high elongation bolt material has been developed. Using new 19 structure wires instead of 7 structure wires, a large elongation, powerful cable bolt has been developed. Also, a bolt torque multiplier has been developed, which enables the output torque of bolt driller to be amplified 6 times, and solves the problems of rock bolt prestressing.

(10) In terms of the characteristics of "low gas reserve, high gas emission" in the LLTCC coalface, comprehensive gas control technology, using mainly the roof high drainage roadway, has been developed. The gas drainage amount from the goaf accounts for 40 % of the total gas emission in the goaf, achieving gas zero overlimit; a large flow underground mobile nitrogen generator has been developed to solve the fire prevention problems at the 10 Mtpa LLTCC coalface and guarantees safe coal mining.

(11) The key technologies and equipment for LLTCC coal mining operation has been successfully evaluated at the No. 8105 coalface of the Tashan coal mine. The underground test demonstrated that the match of "shield, shearer and scraper conveyor" is rational, average usage of face equipment reaches 92.1 %, face coal recovery reaches 88.9 %, the cumulative coal production was 10.849 Mtpa in 2011, achieving the target of 10 Mtpa for a LLTCC coalface in China, and safe and high efficiency coal mining in an ultra-thick coal seam.

## References

Alehossein H, Poulsen BA (2010) Stress analysis of long wall top coal caving. Intern J Rock Mech Min Sci 47(1):30–41

Altounyan P, Taljaard D (2001) Developments in controlling the roof in South African coal mines—a smarter approach. International conference on coal research. South African Institute of Mining and Metallurgy, pp 33–40

Buddery PS, Oldroyd DC (1992) Development of a roof and floor classification applicable to collieries. Proceedings of the Eurock '92 conference. Thomas Telford, London, pp 197–202

Cao SG, Liu CY (1997) Study on the stiffness of the immediate roof of longwall face. Ground Press Strata Control 4:16–19

Cao SG, Qian MG, Liu CY, Miao XX (1998) New research about support and surrounding rock relationship in working face. J China Coal Soc 23(6):575–579

Cao SG, Qian MG, Liu CY (1999) Mechanical characteristics of the immediate roof in working face and working resistance of supports. Mining Science and Technology'99. vol 8, pp 309–312

Chen Y, Yu L, Lan TW (2010) Numerical simulation research on surrounding rock activities in shallow coal seam face. 2010 International symposium on safety science and technology. Science Press USA Inc, pp 1618–1622

Cheng SP (2008) Research on surface movement rules off full-mechanized caving mining with large mining height in mountain area. Coal Min Technol 13(4):37–39

Deng GZ (1994) Characteristics of movement and rupture of the roofs during longwall top coal caving process. Ground Press Strata Control 2:23–26

Duan WS, Gao XC, Dou J (2008) Law of movement and fracture of overlying strata of fully-mechanized top-coal caving face in the hard and thick coal seam. J Xi'an Univ Sci Technol 28(2):211–214

Fan YC, Kang LJ, Kang YH (2003) Fully mechanized long-wall top coal caving mining technology. China Coal Industry Publishing House, Beijing

Fang XQ (2002) Study on stability of support-surrounding rocks and it's control in fully-mechanized top-coal caving face. Doctor's Thesis: China University of Mining and Technology

Fu YG (2008) Study about mining height fully-mechanized coal winning caving face gas governing technology. Coal 17(12):9–12

Hou W, Jiang FX, Wang CW, Feng ZQ, Wang DZ (2009) Pressure control in sub-level long face surrounded by three sides minedAreas of C-shaped stratas patial structure. J China Coal Soc 34(3):310–314

Hu W (1995) Roof control and selection of drawing roof-coal stope. J Xiangtan Mine Inst 10(4):7–13

Huang K (2002) Mechanical system of chock-roof and stability of soft coal longwall face during top caving process. Doctor's Thesis: China University of Mining & Technology (Beijing)

Jia AL, Huang X (2005) Research on bolt support system for full seam gateway in high stressed thick seam. Coal Sci Technol 33(7):45–48

Jia XR, Zhai YD, Yang SS (1998) Structure of roof rocks in sub-level caving face and calculation of roof weighting. J China Coal Soc 23(4):366–370

Jiang FX (1995) Structure patterns and roof-chock relationship in longwall top coal caving. Coal Mine Mod 1:33–35

Jiang FX (2006) View point of spatial structures of overlying strataand its application in coal mine. J Min Saf Eng 23(1):30–33

Jin ZM, Wei JP, Song XM, Xue Y, Niu Y (2002) Test Study on The top cracking process of large coal sample. Proceedings of the '99 international symposium on mining science and technology, Beijing, pp 405–408

Kang LJ (1990) Rupture characteristics and the interaction between roof and chocks in gently-inclined thick coal seams using longwall top caving methods. Master's Thesis: China Coal Research Institute

Kang LJ (1995) Study on top coal stress in caving mining. Proceeding of the international mining Tech'95 symposium. Beijing, pp 18–25

Kang LJ (1996) Ground pressure characteristics in longwall top coal caving work face for gently-inclined seam coal seams. Coal Sci Technol 24(11):39–42

Kang LJ (1998) Limiting effect of strain-softening character of the top coal on loads exerted on the powered supports in a fully mechanized sub-level caving face. J China of Coal Soc 23(2):140–143

Kang LJ (1999) Mechanical coupling relationship between roof and chock in longwall top coal caving method.Coal. Min Technol 4(12):69–71

Kang LJ, Qi QX (1998) Discrete element modelling of longwall top coving process. Coal Min Technol 3(2):3–6

Kang HP, Wang JH (2007) Rock bolting theory and complete technology for coal roadways. China Coal Industry Publishing House, Beijing, pp 83–86

Kang LJ, Shi YW, Yao JG (1991) Interaction between chock and roof in longwall top coal caving for gently-inclined coal seam. Ground Press Strata Control 1:19–24

Kang LJ, Wu G, Zhang YJ (1997) Top coal movement characteristics during longwall top caving process in the Yanquansikuang coal mine. Coal Sci Technol 25(9):13–16

Kang LJ, Zheng XZ, Feng ZC (1998) Investigation on the ground pressure characteristics of the tailgate driven alongside the #10 longwall gob in the Nantun coal mine. Coal Sci Technol 26(7):41–45

Kang LJ, Liu JH, Ceng HF, Wang LX (1999) Study on the behavior and controlling method for hard roof strata of seam No. 4 in Wang ping Colliery. Coal. Min Technol 1:69–71

Kang TH, Chai ZY, Li YB, Ge YY, Zhang HB, Liu RR (2007a) Study on physical simulation of full-seam mining for a 20 m very thick and medium hard seam by sub-level caving mining with high bottom cutting Height. Chin J Rock Mech Eng 26(5):1065–1072

Kang HP, Wang JH, Lin J (2007b) High pre-tensioned stress and intensive bolting system and its application in deep roadways. J China Coal Soc 32(12):1233–1238

Kang HP, Jiang TM, Gao FQ (2008) Design for pre-tensioned rock bolting parameters. J China Coal Soc 33(7):721–726

Kong LH, Jiang FX, Liu J, Yie GX, Wang CW, Song GD (2009) High-precision microseismic monitoring system to reasonable width of segment coal pillar in extra-thick coal seam fully mechanized top-coal caving mining. J China Coal Soc 34(7):871–874

Kong LH, Jiang FX, Yang SH, Song JW, Wang CW (2010a) Movement of roof strata in extra-thick coal seams in top-coal caving mining based on a high precision micro-seismic monitoring system. J Univ Sci Technol Beijing 32(5):552–558

Kong LH, Jiang FX, Liu J, Wang CW (2010b) Relationship between support and strata in extra-thick coal seam fully-mechanized sublevel caving mining based on high precision microseismic monitoring technology. Chin J Geotech Eng 32(3):401–406

Kong LH, Jiang FX, Wang CW (2010c) Study of reasonable working resistance of support in fully-mechanized sublevel caving face in extra-thick coal seam. Chin J Rock Mech Eng 29(11):2312–2318
Li MZ, Liu KM, Zeng MS (2006) Full seam cutting and caving mining technology in and its development prospect. Coal Mining Technology 11(5):28–29, 43
Li L, Xu G (2009) Researchon supporting density of powered support for full-mechanized caving ming in Shuiliandong colliery. Coal Min Technol 14(5):86–88
Liu CY (1996) Mechanical characteristics of immediate roof and chock-roof relationship in longall mining face. Doctor's Thesis, China University of Mining & Thechnology
Liu J (2008a) Microseismic monitoring in longwall top coal caving for an extra-thick coal seam. Min Saf Environ Prot 35(1):44–46
Liu KG (2008b) Studying about mining hight fully-mechanized coal winning caving the roof activity. Coal 17(6):9–11
Liu QM (2010) Research on space effect of face length of fulimechanized caving mining with large mining height. Coal Min Technol 15(3):27–29
Liu CY, Huang BX (2009) Technical parameters of drawing and coal-gangue field movements of a fully mechanized large mining height top coal caving working face. Min Sci Technol 19(5):549–555
Liu CY, Qian MG, Cao SG, Miao XX (1997) Influencing mechanism of immediate roof on the relation between supports in the workings and surrounding rocks. J China Coal Soc 22(5):471–476
Liu CY, Wan ZJ, Cao SG (2002) The deformation destroying interaction regulation of immediate roof and top-coal in long wall sublevel caving face. Proceedings in mining science and safety technology. Science Press, Beijing, pp 105–109
Liu YD, Zhang DS, Wang HS (2006) Simulation analysis of coal mining with top-coal caving under hard-and-thick strata. J China Univ Min Technol 16(2):110–114
Lu XS, Zhao XL (2006) XU XD, Xue SJ. Kit technique research about fully-mechanized coal winning equipment. Coal 15(6):6–7
Ma QH (2005) Study of the overlying strata "O" letter type spatial structures of long wall and correlate rock pressure. Doctor's Thesis: Shandong University of Science and Technology
Ma JY, Zhang ZQ (2008) Research on coal roadway supported by bolting with mesh. J Taiyuan Univ Technol 39(5):233–235
Mao DB, Yao JG (2010) Adaptability of long wall top coal caving with high cutting height. J China Coal Soc 35(11):1837–1841
Meng QK (2007) Fully mechanized high cutting height and caving mining technology and hydraulic powered support selection in Wobei mine. Coal Sci Technol 35(8):53–54
Meng D, Shen J, Zhao Y (2010) Determination of the hydraulic supporting resistance based on a simplified structural system. Metal Mine 10:24–28
Miao SJ, Lai XP (2011) Top coal flows in an excavation disturbed zone of high section top coal caving of an extremely steep and thick seam. Min Sci Technol (China) 21(1):99–105
Nan H, Xu T, Wei ZD (2008) Application of RFPA 2D in sublevel caving mining extra-thick coal seams. Materials Sci Forum 575:1246–1251
Qian MG, Shi PW (2003) Coal mine pressure and roof control. China Coal Industry Publishing House, Beijing
Qian MG, He FL, Miao XX (1966) The system of strata control around long wall face in China. Mining Science & Technology, pp 15–18
Qian MG, Miao XX, He FL, Liu CY (1996) Coupling mechanics of chock and roof in longwall mining face. J China Coal Soc 21(1):40–44
Ren RH (2005) Surface movement regularity of super-wide mining face with top-coal caving. J China Univ Min Technol 15(1):68–71
Shi H (2005) Study and applications ability of hard and massive overlying stratain fully mechanized sub level caving face. Doctor's Thesis: Shandong University of Science and Technology
Shi YW, Chen SJ (1993) Ground control of floor in retreating mining face. China Coal Industry Industry Publishing House, Beijing
Shi H, Jiang FX (2004) Mechanical analysis of rupture regularity of hand and massive overlying strata of longwall face. Chin J Rock Mech Eng 23(18):3066–3069
Shi H, Jiang FX (2005) Study on relationship between roof stability and recovery ratio of top coal at first weight period in fully-mechanized sublevel caving face. Chin J Geotech Eng 27(4):414–417
Shi YW, Ning Y, Qi QX (1993) Ground control and optimum parameters in longwall top coal caving technologies. China University of Mining & Technology Press, Xuzhou
Shi H, Jiang FX, Wang HJ (2005) Study on relationship between roof stability and top coal's recovery ratio burning cyclic weighting in fully-mechanized sublevel caving face. Chin J Rock Mech Eng 24(23):4233–4238
Shi HM, Du JW, Li ZQ (2009) Mining height long caving mining stope pressure control technology. Coal 18(11):14–16
Song JW, Gao RP, Wang AW (2010) Science and Technology of West China 20(9):6–10
Su H (2008) Stability analysis and ground control of coal measures during longwall top coal caving process China. Coal 34(2):35–36
Wang JC (2005) Fully mechanized longwall top coal caving technology in China and discussion on issues of further development. Coal Sci Technol 33(1):14–17
Wang JH (2006a) Present status and development tendency of fully mechanized coal mining technology and equipment with high cutting height in China. Coal Sci Technol 34(1):4–7
Wang HJ (2006b) Resarch on the movement and control of "O"letter type overlying milti-strata spatull structures of face surrounded by mined areas. Doctor's Thesis: Shandong University of Science and Technology
Wang JC (2009) Theories and technologies for mining thick coal seams. Metallurgical Industry Press, Beijing
Wang GF (2010a) Top-caving powered support and fully-mechanized caving technology. China Coal Industry Publishing House, Beijing
Wang M (2010b) Study on the laws of strata behavior in the top-coal caving of fully mechanized mining. Master's Thesis: Taiyuan University of Technology
Wang JH (2011) Present status and prospects of modernized mining technology and equipment in China coal mine. Coal Sci Technol 39(1):1–5
Wang JH (2013a) Key technology of complete equipment for fully-mechanized top coal caving face with large mining height in extra-thick seam. Coal Sci Technol 41(9):1–5
Wang JH (2013b) Key technology for fully-mechanized top coal caving with large mining height in extra-thick coal seam. J China Coal Soc 38(12):2089–2098
Wang ZF, Li QS, Yang LP, Liu J (2001) Research to ensure the height of displacement caving zone in overlying strata at Xiashijie coal mine combined working face. Coal 16(1):1–3
Wang JS, Chai ZY, Kang TH, Li YB (2007) Numerical simulation of full seam mining for a 20 m very thick and medium hard seam by fully mechanized sublevel caving. J Taiyuan Univ Technol 38(2):175–178
Wang JH, Kang HP, Gao FQ (2008) Numerical simulation on load-transfer mechanisms and stress distribution characteristics of cable bolts. J China Coal Soc 33(1):1–6
Wang GF, Pang YH, Liu JF (2012) Determination and influence of cutting height of coal by top coal caving method with great

mining height in extra thick coal seam. J China Coal Soc 37(11):1777–1782
Wu J (1998) Reviews on the longwall top coal caving technologies in the past 15 years. Proceedings of the 3rd Longwall Top Coal Caving Theory and Application Conference
Wu YP (2008) Research on full mechanized caving mining technology in extremely thick and complicated coal seam. Coal Min Technol 13(1):18–20
Wu J, Fu Q (1998) Current situation and prospect of top coal caving technology in China. J China Univ Min Technol 8(2):108–112
Wu J, Yan SH (1995) Basic concepts of determining resistance of face support with fully mechanized mining and top coal caving. Mine pressure and roof management 3(4):69–71
Wu J, Zhang Y (2001) The new concept of relationship between support and surrounding-rock in longwall top-coal caving faces. J China Coal Soc 26(4):350–356
Xie GX (2005) Mechanical characteristics of fully mechanized top-coal caving face and surrounding rock stress shell. J China Soc 30(3):303–313
Xie GX (2006) Influence of mining thickness on mechanical characteristics of working face and surrounding rock stress shell. J China Coal Soc 31(1):6–10
Xie GX, Luo Y (2005) Study on the Countermeasures against methane outburst of mining multiple upper protective layers in coal seams C luster. J Coal Sci Eng 11(1):31–35
Xie YS, Zhao YS (2009a) Numerical simulation of the top coal caving process using the discrete element method. Intern J Rock Mech Min Sci 46(6):983–991
Xie YS, Zhao YS (2009b) Technique of top coal caving with vibration. Procedia Earth Planet Sci 1(1):219–226
Xie GX, Chang JC, Yang K (2006a) Investigation on the stress field characteristic of top coal at FMTC faces under the influence of caving thickness. J Coal Sci Eng 13(2):123–125
Xie GX, Yang K, Liu QM (2006b) Study on distribution laws of stress in inclined coal pillar for fully-mechanized top-coal caving face. Chin J Rock Mech Eng 25(3):545–549
Xie GX, Yang K, Chang JC (2007a) Study on distribution characterics of 3D stress and thickness effects of coal-seam in unsymmetrical disposal and fully-mechanized top-coal caving. Chin J Rock Mech Eng 26(4):775–779
Xie GX, Yang K, Hua XZ (2007b) Influence of mining velocity on mechanical characteristics of surrounding rock in fully mechanized top-coal caving face. Chin J Geotech Eng 29(7):963–967
Xie GX, Chang JC, Yang K (2009) Investigations into stress shell characteristics of surrounding rock in fully mechanized top-coal caving face. Intern J Rock Mech Min Sci 46(1):172–181
Xing SJ, Wang JZ, Zhao YB (2009) Development and application of top coal caving hydraulic supports with large mining height. China Coal 35(4):81–83
Yan SH (2008) Research on side and roof falling mechanism and control approaches in caving mining with large mining height. Coal Min Technol 13(4):5–8
Yan SH (2009) Theory study on the load on support of long wall with top coal caving with great mining height in extra thick coal seam. J China Coal Soc 34(5):590–593
Yan SH, Fu Q (2003) Movement characteristics of the strata above the coal seam under longwall top coal caving. China Coal Industry Publishing House, Beijing
Yan SH, Yin XW (2008) Discussing about the main theoretical problems of long wall with top coal caving. J China Coal Soc 33(5):481–484
Yan SH, Jia GS, Liu XL (1996) Analysis of mechanism of overlying strata structure transmitting toward upper position in top coal caving. Mine Press Roof Manag 3:3–5
Yan SH, Yin XW, Xu HJ, Xu G, Liu QM, Yu L (2011) Roof structure of short cantilever-articulated rock beam and calculation of support resistance in full-mechanized face with large mining height. J China Coal Soc 36(11):1816–1820
Yang JL (2007) Stability and ground control of coal measures during longwall top coal caving process.China. Coal 33(11):37–39
Yang PJ (2009) Research on the relationship between two-leg sublevel caving shield support and surrounding rocks and adaptability. Doctor's Thesis: China University of Mining and Technology
Yasitli NE, Unver B (2005) 3D numerical modeling of long wall mining with top-coal caving. Intern J Rock Mech Min Sci 42(2):219–235
Yin XW, Yan SH, An Y (2008) Characters of the rib spalling in fully mechanized caving face with great mining height. J Min Saf Eng 25(2):222–225
Yu L, Fan ZZ, Xu G (2011) Study on the structure characteristics and ground pressure behavior of overlying strata with shallow buried coal seam. Adv Mater Res 255–260:3780–3785
Yu L, Yan SH, Liu QM (2012) Determination of support working resistance of top coal caving in extra thick coal seam. J China Coal Soc 37(5):737–742
Zhang DL (1995) Stability and ground control of coal measures in longwall top coal caving. Doctor's thesis: China University of Mining & Technology
Zhang DL (1999) Ground control in longwall top coal caving. China Coal Industry Publishing House, Beijing
Zhang HJ, Liu QM (2008) Research on the fuzzy clustering of comprehensive support working resistance. China Min Mag 17(10):93–98
Zhang CW, Yang WB (2010) Technology of supporting deep full-seam coal roadway with high stress. Coal Min Technol 15(4):63–64
Zhang BS, Kang LX, Yang SS (2006) Numerical simulation on roof separation and deformation of full seam roadway with stratified roof and large section. J Min Saf Eng 23(3):264–267
Zhang Z, Kang HP, Wang JH (2010) Pre-tensioned stress coordination function analysis of bolt-cable anchor support in coal roadway. J China Coal Soc 35(6):881–886
Zhang JG, Zhao ZQ, Gao Y (2011) Research on top coal caving technique in steep and extra-thick coal seam. Procedia Earth Planet Sci 2:145–149
Zhou ZL, Su H (2008) Support technologies for longwall top coal caving face ends. Coal 17(6):18–20
Zhu LF, Yan SH (2011) Numerical simulation of top-coal movement rule in fully-mechanized caving mining with large mining height. Coal Min Technol 16(1):11–13